THE UNIVERSITY *of* EDINBURGH

Simple Molecular Systems at Extreme Conditions

Robin Turnbull

A thesis submitted in fulfilment of the requirements
for the degree of Doctor of Philosophy
to the
University of Edinburgh

May 29, 2018

Supervisor: Prof. E. Gregoryanz

Examiners: Prof. M. I. McMahon and Prof. C. Pickard

Abstract

This thesis project has focussed on the experimental study of simple molecular systems at extreme conditions. High-pressure and high-temperature techniques have been used in combination with Raman spectroscopy and X-ray diffraction diagnostics to characterise three simple molecular systems which are unified by the inclusion of nitrogen as a constituent element.

The N_2 molecule contains the only triple-bond amongst the elemental diatomics and is considered a model system for exploring the changes in structure and bonding induced by tuning pressure and temperature conditions. As such the nitrogen phase-diagram is a focus-point in current extreme conditions research and nitrogen has been found to exhibit a high-degree of polymorphism not observed in other simple molecular systems such as hydrogen or oxygen. Understanding molecular mixtures of nitrogen with other simple molecules at extreme conditions is significant to many scientific fields varying from chemistry to astronomy.

The first system presented is the binary mixture of nitrogen and xenon which was studied as a function of pressure. The study constitutes the first comprehensive study of the xenon-nitrogen system at high-pressures. A new van der Waals compound was observed which underwent a phase transition at 14 GPa and was stable up to at least 180 GPa and 3000 K, conditions where pure nitrogen becomes amorphous. Optical measurements suggested possible metallization of the new compound around 120 GPa.

The second system presented is the binary mixture of nitrogen and hydrogen which was studied both as a function of pressure and composition. Two known nitrogen-hydrogen structures were confirmed and a pressure-temperature path-dependent formation of hydrazine or ammonia was discovered. Additionally, one mixture was compressed to 242 GPa, the highest pressure investigated in the nitrogen-hydrogen system.

The third system presented is the elemental nitrogen phase known as ι-nitrogen, an elusive high-temperature polymorph which has hitherto eluded structure determination and proved challenging to access. ι-nitrogen was successfully characterised as having an extraordinarily large unit cell containing 48 N_2 molecules, making it the most complex molecular nitrogen structure to be determined unambiguously.

Lay Summary

Extreme conditions are very common in the universe, from the cold vacuum of deep space to the elevated temperatures and pressures within stars. It is important to study matter at these conditions if we are to understand the world around us. Many interesting phenomena occur when materials are subjected to extreme conditions, one of the most intriguing of which is phase transitions. The freezing/melting and boiling/condensing of water are common examples of phase transitions which we observe in our daily lives. At extreme conditions phase transitions can be observed in common materials which might not be traditionally expected, for example, the oxygen gas which we all breathe at ambient conditions becomes a solid metal at very low temperatures and high pressures. More subtle phase transitions are also observed at extreme conditions. For example, diamond and graphite are both solid phases of carbon, but they have very different properties and it is possible produce diamond from graphite by subjecting it to elevated temperatures and pressures. The work of this thesis particularly relates to solid phases at extreme conditions and aims to characterise novel nitrogen-containing materials which have not previously been observed at ambient conditions.

Declaration

Except where otherwise stated, the research undertaken in this thesis was the unaided work of the author. Where the work was done in collaboration with others, a significant contribution was made by the author.

Parts of Chapter 5 have been published in Sci. Rep. 6, 34896 (2016).

Signed: .....

R. Turnbull

May 29, 2018

Acknowledgments

I would like to record my thanks to all those who have helped me in the course of this work. In particular, the following:

My supervisor Prof E. Gregoryanz for providing me with the opportunity to undertake the Ph.D., the freedom to follow my research interests, and the wisdom to do so fruitfully.

Dr R. Howie for his many patient teachings without which I would not have been able to conduct the experiments of this thesis.

Dr J. Binns for regaling me with tales of X-ray crystallography. His discussions over the course of the Ph.D. have been invaluable.

Dr M. Frost for showing me the meaning of haste, and Dr P. Dalladay-Simpson for showing me the meaning of deliberation.

Dr M. Peña-Alvarez for her unwavering good-spirits and assistance which were much appreciated in the many late nights working in the lab, and A. Coleman, V. Afonina and E. Pace for being great office mates.

Dr M. Hanfland, without whom Chapter 5 may not be so complete, and the technical staff in the Physics Workshop without whom many of the experiments would not have been possible.

The EPSRC for financial support.

Finally, those who are not last in my thoughts, my family and María, for their unfailing love, encouragement and guidance.

This thesis is dedicated to the memory of my grandfather William.

Contents

List of Figures

List of Tables

Chapter 1

Introduction

This introduction section attempts to set in context the contributing work of this thesis and to indicate what is peculiarly interesting about the extreme conditions area of condensed matter physics, specifically regarding simple molecular systems.

Condensed matter physicists seek to understand the physical properties of systems in which there is a large number of interacting particles. In practice this often means asking about the behaviours of macroscopic thermodynamic observables as an external control parameter is varied. These behaviours are mapped out by drawing phase-diagrams, which show the state of the system for a given choice of the external control parameters. The properties of a system when it is in a particular phase are determined by its structure, and structural changes may be induced by tuning the external control variables of pressure and temperature, as probed in the contributing work.

Phase transitions are a particularly interesting phenomenon in extreme-conditions research, and they emerge as a result of inter-particle interactions. A system of neutral atoms interacting via the famous Lennard-Jones potential already exhibits phase-transitions, and when simple molecules are considered phase-diagrams can become drastically more complicated. The compression of molecular systems to megabar pressures (100s of gigapascals) is becoming routinely achievable with

modern diamond-anvil cells and the free-energy change associated with such compression is comparable to the energy of intramolecular bonds (10s of eVs) leading to phenomena such as the pressure-induced evolution of bonding.

Phase transitions and modified bonding are some of the phenomena associated with molecular systems at extreme conditions which have implications spanning the chemical and physical sciences. Molecular nitrogen is frequently used in both theoretical and experimental investigations as a prototype simple molecule as it contains the strongest (and only) triple-bond amongst the homonuclear diatomics. Nitrogen features as a constituent element in each of the three experimental systems studied in this thesis: ι-nitrogen, nitrogen–xenon and nitrogen–hydrogen.

1.1 Thesis Outline

There are eight chapters in this thesis including this introduction chapter. Chapters 2 and 3 introduce the reader to the conceptual and experimental background relevant to the contributing work. Chapter 4 presents the reader with a review of nitrogen at extreme conditions. Chapters 5, 6 and 7 detail the contributing work into three independent high-pressure systems which are unified by the inclusion of nitrogen as a constituent element. Chapter 8 presents a summary of the main conclusions of the contributing work and discusses possible future studies.

Chapter 2: Spectroscopy and Diffraction

This chapter introduces the reader to the theory behind the two main diagnostics used in this thesis: Raman spectroscopy and X-ray diffraction. An overview of Raman spectroscopy is followed by a short section on the interpretation of experimental Raman spectra. A brief discussion of the theory behind X-ray diffraction relevant to the contributing work is introduced.

Chapter 3: Experimental Techniques

This chapter describes the experimental techniques used in this thesis. The first half of the chapter covers the high-pressure and high-temperature techniques used to achieve extreme conditions. The second half of the chapter gives an experimental overview of the Raman and X-ray diffraction diagnostics introduced in Chapter 2.

Chapter 4: Review of Nitrogen at Extreme Conditions

Nitrogen is central to each of the three following experimental chapters of this thesis. This chapter presents the reader with a review of nitrogen at extreme conditions with a discussion centred around the experimental nitrogen phase-diagram.

Chapter 5: Nitrogen–Xenon

This chapter constitutes the first comprehensive experimental study of the xenon–nitrogen system at high-pressures. A new solid $Xe(N_2)_2$ van der Waals compound was observed which undergoes a phase transition at 14 GPa. The molecular nitrogen in the $Xe(N_2)_2$ compound was observed up to the maximum pressure studied of 180 GPa, surpassing the non-molecular limit in pure nitrogen.

Chapter 6: Nitrogen–Hydrogen

This chapter details exploratory work into the behaviour of nitrogen-hydrogen mixtures as a function of both composition and pressure. Powder XRD experiments revealed mixed phases of known nitrogen-hydrogen solids. Room and high-temperature Raman experiments demonstrated a P-T path-dependent synthesis of hydrazine or ammonia. The first megabar study of the nitrogen-hydrogen system is also presented in which the two species were not mutually soluble.

Chapter 7: ι-Nitrogen

This chapter constitutes the first study of ι-nitrogen to determine its crystal structure. ι-nitrogen is an elusive high-temperature phase which has remained

relatively unexplored since its discovery. The single-crystal diffraction data were acquired at a sample pressure of 56 GPa. Previously, the highest pressure at which a nitrogen structure had been determined was 14.5 GPa. The discrepancies in the literature regarding the P-T synthesis conditions of ι-nitrogen are discussed based on observations made in this work. The chapter concludes with a discussion of ι-nitrogen and possible related phases.

Chapter 8: Conclusions

This final chapter summaries of the main conclusions and underlines some of the questions raised throughout the project in the context of future investigations.

Chapter 2

Spectroscopy and Diffraction

Raman spectroscopy and X-ray diffraction are the two main diagnostics used in this thesis. Section 2.1 opens with a brief introduction to general spectroscopy followed by an overview of Raman spectroscopy and how it is used to probe molecular structures. Section 2.2 introduces the reader to X-ray diffraction (XRD) from solids and how it is used to probe crystal structures.

2.1 Spectroscopy

Spectroscopy is the study of matter through its interactions with electromagnetic radiation. There are many different mechanisms of light-matter interaction, including: emission, absorption, elastic scattering and inelastic scattering. In spectroscopy, electromagnetic radiation of a known energy (or spectrum of energies) is incident on a scattering medium. The scattered radiation is detected and generally the electromagnetic intensity is plotted as a function of wavelength. The spectra contain quantitative and qualitative information about the scattering medium which may be extracted. The information which is encoded into spectra is generally found within three spectral characteristics, each of which will later be discussed in terms of Raman spectra, these are:

1. The spectral line **positions**, which are determined by the allowed energy levels in the scattering molecules.

2. The spectral line **intensities**, which are determined by:

   — *population of states* – how many molecules can undergo transition.

   — *transition probability* – how likely the transition is to occur.

   — *optical path-length* – how much sample is being probed.

3. The spectral line **widths**, which may be determined by various broadening mechanisms, such as:

   — *Doppler broadening* – distribution of molecular velocities.

   — *lifetime broadening* – uncertainty in energy of excited states.

   — *collision broadening* – energy levels perturbed by collisions.

   — *systematic broadening* – due to experimental set-up.

Whilst not all of these factors will be discussed this summary aims to illustrate the wealth of information which may be determined from spectroscopy experiments. Depending on the type of radiation used it is possible to probe different excitations, including: nuclear spin, electron spin, molecular rotation, molecular vibration, valence-electron excitation and core-electron excitation. The excitations of interest in this thesis are specifically vibrational and rotational excitations, which lie in the infra-red region of the electromagnetic spectrum.

In classical infra-red spectroscopy a sample is illuminated with a broad spectrum of infra-red radiation and the observed absorption bands in the transmission spectrum are characteristic of certain molecular vibrations. Symmetrical molecules, such as the homonuclear diatomics investigated in this thesis (N_2 and H_2), are inactive in infra-red spectroscopy because their dipole moment (which is zero) does not change during vibration.

Raman spectroscopy is a complimentary technique which allows vibrations in symmetric molecules to be probed because the gross selection rule is a *polarisability* which changes with molecular vibration. Raman spectroscopy uses a single incident frequency (usually in the visible region) which allows investigation of a very wide range of excitations spanning both rotational and vibrational modes.

2.1.1 Raman Spectroscopy

The Raman effect was discovered experimentally in 1928 by two independent groups: Raman and Krishnan [Raman 28b, Raman 28a]; and, Landsberg and Mandelstam [Landsberg 28]. It was first predicted in 1923 by Smekal [Smekal 23] who suggested that a system with quantised energy levels would scatter incident light with both shifted and unshifted frequencies. The inelastic scattering of photons by excited molecules is known as the *Raman effect*. The Raman effect is a statistically weak effect because the majority of photons scatter elastically, while roughly only one in every million scatters inelastically. The invention of the laser in 1960, and the development of high resolution digital spectrometers, have allowed Raman spectroscopy to become a mainstream diagnostic for substance analysis. Raman spectroscopy can be conducted on very complex biological molecules, providing fingerprint spectra which can be used to quickly identify materials.

In the following sections the phenomenon of Raman scattering is initially explained using a semi-classical model of a homonuclear diatomic molecule, which describes the experimental observation of frequency-shifted spectral lines. The semi-classical description is followed by a brief quantum mechanical description which explain some of the spectral details which are not recovered by the semi-classical description, such as the spectral line intensities.

2.1.2 Semi-classical Description of Raman Scattering

Homonuclear diatomic molecules do not poses a permanent electric dipole moment, $\boldsymbol{\mu}$, and are thus inactive in infra-red absorption spectroscopy. Induced dipole moments, $\boldsymbol{\mu}_{ind}$, are created in Raman spectroscopy by exposing molecules to an electric field of strength, $\mathbf{E}$. The induced dipole moment is proportional to the field strength:

$$\boldsymbol{\mu}_{ind} = \alpha \mathbf{E}, \tag{2.1}$$

where the proportionality constant, α, is the *polarisability* coefficient which describes the extent to which the electron cloud in the molecules is redistributed. The polarisiability is characteristic of the molecules in the scattering medium. Strictly the polarisiability is actually described by a tensor because polarisability in real molecules depends on the coordinates of the atoms. In free atoms, such as noble gases, the polarizability tensor is isotropic in all directions, but in linear molecules the polarizability tensor is anisotropic ($\alpha_{\parallel} \neq \alpha_{\perp}$).

If the electric field which is inducing the dipole moment, $\boldsymbol{\mu}_{ind}$, has time-dependent oscillation, as it would in electromagnetic radiation from a laser, then the field strength, $\mathbf{E}$, can be described by:

$$\mathbf{E} = \mathbf{E}_0 \cos(2\pi\nu_0 t). \tag{2.2}$$

where ν_0 is the the frequency of the laser light. We can see by substituting (2.2) into (2.1) that the induced dipole moment, $\boldsymbol{\mu}_{ind}$, will also therefore have a time-dependence:

$$\boldsymbol{\mu}_{ind}(t) = \alpha(t)\mathbf{E}_0 \cos(2\pi\nu_0 t), \tag{2.3}$$

and in fact will oscillate at the same frequency, ν_0, as the incident radiation. The polarisability has also necessarily picked up a time-dependence, $\alpha(t)$, because it depends on the atomic coordinates which change as the diatomic molecule vibrates. The time-dependence of the polarisability can be expressed as a constant plus a time-dependent term:

$$\alpha(t) = \alpha_0 + \alpha_1 \cdot \cos(2\pi\nu_R t), \tag{2.4}$$

where ν_R is some natural frequency of a molecular vibration.

Substituting the time-dependent polarisability, $\alpha(t)$, given by (2.4), into the expression for the induced dipole moment, $\boldsymbol{\mu}_{ind}(t)$, given by (2.3), the expression now has two terms:

$$\boldsymbol{\mu}_{ind}(t) = \alpha_0 \mathbf{E}_0 \cos(2\pi\nu_0 t) + \alpha_1 \mathbf{E}_0 \cos(2\pi\nu_0 t)\cos(2\pi\nu_R t). \tag{2.5}$$

where the second term contains a multiplication of similar cosines, containing ν_0 and ν_R, which can be expanded using using the trigonometric identity:

$$\cos(A)\cos(B) = \frac{1}{2}[\cos(A+B) + \cos(A-B)], \tag{2.6}$$

giving us our final expression for the time-dependent induced-dipole:

$$\begin{aligned} \boldsymbol{\mu}_{ind}(t) = \alpha_0 \mathbf{E}_0 \cos(2\pi\{\nu_0\}t) \\ + \alpha_1 \mathbf{E}_0 \cos(2\pi\{\nu_0 + \nu_R\}t) \\ + \alpha_1 \mathbf{E}_0 \cos(2\pi\{\nu_0 - \nu_R\}t). \end{aligned} \tag{2.7}$$

The induced dipole-moment therefore oscillates in a superposition of three oscillation modes, corresponding to each of the terms in (2.7). The first term is a function of ν_0 and therefore describes elastic scattering in which the dipole oscillates at the same frequency as the incident radiation. The second and third terms of (2.7) demonstrate that the induced-dipole additionally oscillates at frequencies which are shifted from the incident radiation, ν_0, by $\pm\nu_R$. An oscillating dipole emits electromagnetic radiation and it is these shifted frequencies which are detected in Raman spectroscopy.

This semi-classical description successfully recovers the observation of Raman scattering into frequency-shifted spectral lines and it provides the gross vibrational selection rule that $\alpha_1 \neq 0$, which states that the polarisability of the diatomic molecule must change with the vibration. The semi-classical description does not however explain the observed intensities of the spectral lines, nor does it meaningfully explain what the energy shift, $\pm\nu_R$, corresponds to. In order to explain these factors it is necessary to give a quantum-mechanical description of Raman scattering in which the molecular vibrational and rotational energies take discrete values.

2.1.3 Quantum-mechanical Description of Raman Scattering

The three scattering terms of equation (2.7) are illustrated in Figure 2.1. In each of the three cases an incident photon of frequency, ν_0, pushes the molecule into a virtual excited state. As the molecule relaxes a second photon is emitted which has either lost or gained an energy characteristic of the difference between the quantised vibrational or rotational energy levels of the molecule. (In the case of Rayleigh scattering the scattered photon has the same energy as the incident photon.) In Figure 2.1 the vibrational states $v = 0$ and $v = 1$ are used for the sake of illustration, however Raman scattering can be used to measure differences

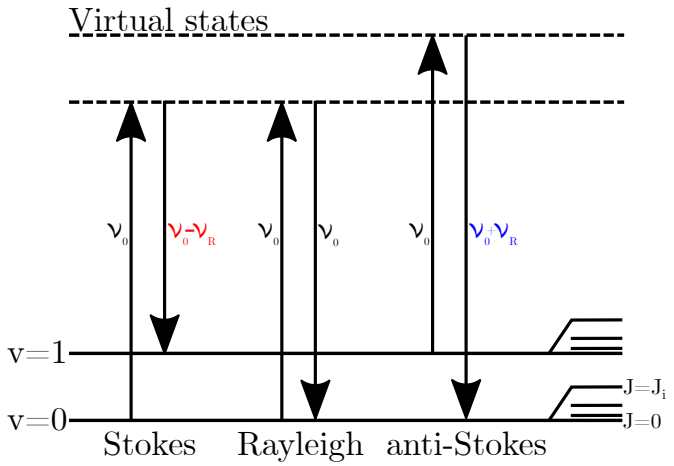

Figure 2.1: An illustration of the three types of scattering processes observed in Raman spectroscopy described by equation (2.7)

between rotational modes (shown on the right hand side of Figure 2.1) or even between excited electronic states in the case of resonance Raman scattering. It is important to note that the energy of the levels themselves is not observable, only the difference between them.

Figure 2.1 is also useful for illustrating the mechanism behind the different observed intensities of the Stokes and anti-Stokes lines. Clearly their relative intensities will depend on the occupation of the initial state, either $v = 0$ or $v = 1$ in the illustrated example. The state occupancy is given by the Boltzmann distribution, and at room-temperature the thermal energy available to the system puts the majority of molecules will be in the ground-state, $v = 0$. Consequently the Stokes line is by far more intense at room-temperature and only in high-temperature experiments reaching close to 1000 K do the anti-Stokes bands appear. The theoretical relative intensities can be given by the ratio of Boltzmann distributions given in equation (2.8) [Long 77]:

$$\frac{\mathrm{I}_{anti-Stokes}}{\mathrm{I}_{Stokes}} = \left[\frac{\nu_0 + \nu_R}{\nu_0 - \nu_R}\right]^4 \exp\left(-\frac{hc\nu_R}{k_B T}\right), \tag{2.8}$$

2.1.4 Experimental Raman Spectra

The purpose of this section is to illustrate some of the important considerations and phenomena associated with interpreting observed Raman spectra.

In the above discussion only a single isolated molecule was considered. In a real system of molecules the intermolecular interactions can be sufficient to shift or even split Raman bands. For example, molecules occupy distinct sites in crystalline solids and as such experience locally anisotropic crystal fields which affects their polarisability. The different potentials experienced by identical molecules sitting on distinct sites in real crystals means that many different Raman bands may be observable for the same transition in different molecules.

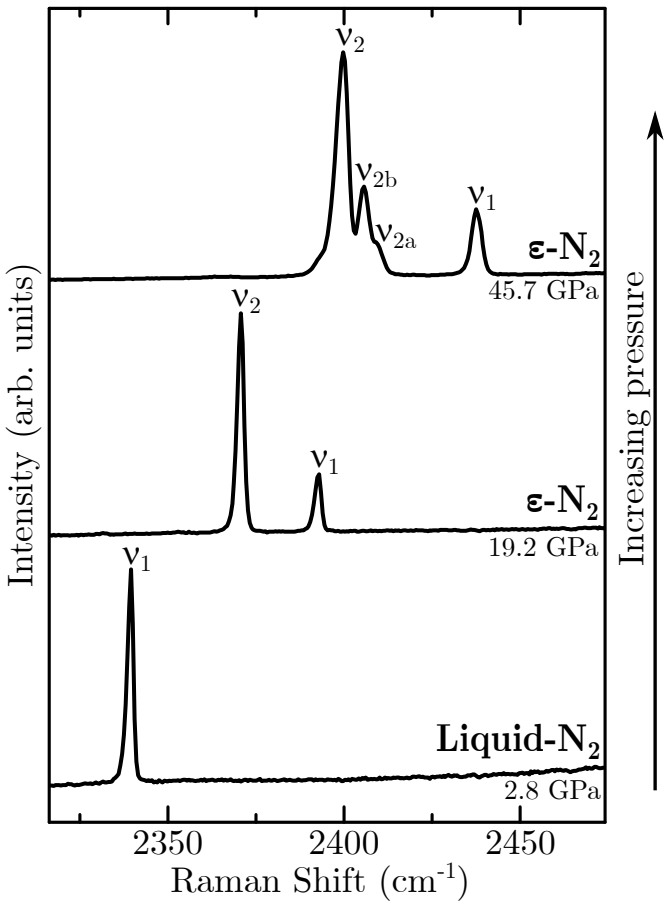

Figure 2.2: The evolution of Raman spectra acquired from a system of N_2 molecules (vibrational region only) with increasing pressure. The lower spectrum is from liquid-N_2 at 2.8 GPa. The middle and upper spectra are from the ϵ-N_2 solid at 19.2 and 45.7 GPa respectively.

The shifting and splitting of Raman modes is illustrated in Figure 2.2[†] using Raman spectra from a sample of N_2 molecules. The lower spectrum, acquired from liquid N_2, exhibits a single Raman vibrational mode, labelled ν_1. In the liquid state the N_2 molecules experience the same time-averaged environment and hence only a single vibrational mode is observed.

In the middle spectrum of Figure 2.2 the nitrogen system has been frozen into the solid ϵ-phase by isothermal compression at room-temperature. The crystallisation into ϵ-N_2 has lifted the site degeneracy, and a second vibrational mode is observed, ν_2, even though both systems are comprised solely of N_2 molecules which, if isolated, would have identical vibrational eigen-energies. The different relative intensities of ν_1 and ν_2 can be attributed to the different number of molecules occupying the distinct sites. It is important to note here that the ϵ-N_2 spectra shown in Figure 2.2 were acquired from a polycrystalline sample (discussed in section 2.2.3) and as such the observed Raman intensities were not affected by the orientation of the sample. Because Raman scattering depends on the polarisability, which is anisotropic in N_2 molecules, the relative peak intensity would in principle have a dependence on the orientation of the sample in the experiments if it consisted of single crystal.

Looking again at Figure 2.2 and comparing the liquid-N_2 spectrum with the lower ϵ-N_2 spectrum, another interesting observation is that the ν_1 band shifted to higher energies when pressure was increased. (The ν_1 label is correct because the peak can be tracked via incremental pressure increases.) The observation of increasing Raman shift is common in high-pressure Raman experiments and can be explained by the work being done on the sample increasing the energy-level spacing. A molecule confined to a localised region of space, such as in the ϵ-N_2 crystal, can be described to a first approximation as a quantum harmonic oscillator. As the strength of the quantum harmonic oscillator potential well is increased (i.e. the pressure in increased) the spacing between adjacent the eigen-

[†]N.B. The units used for Raman spectra are reciprocal centimetres, cm^{-1}, which have an implied factor of hc and therefore represent an energy.

energies increases. The peaks in Raman spectra show precisely the differences between those energy levels.

The top two spectra in Figure 2.2 are from ϵ-nitrogen at different pressures, yet their Raman spectra appear quite different. ϵ-nitrogen is characterised by a rhombohedral unit cell as determined via X-ray diffraction experiments (discussed in the next section) at these pressures. The splitting of ν_2 into additional peaks ν_{2a} and ν_{2b} can be attributed to the molecules on the sites corresponding to ν_2 picking up an orientational preference as pressure is increased, again lifting the site degeneracy [Olijnyk 99]. This is an important observation because depending on the definition of 'phase' it may not be possible to identify phase-transitions using Raman spectroscopy alone. Very often in high-pressure physics it is necessary to use X-ray diffraction as a diagnostic complimentary to Raman spectroscopy, or indeed vice versa.

2.2 X-Ray Diffraction

The technique of X-ray diffraction is used to determine the structure of crystalline solids. It was developed 1912 by two groups: Max von Laue[†], Walter Friedrich[‡] and Paul Knipping[§] who performed the first X-ray diffraction experiments on copper sulfate pentahydrate - a triclinic crystal; and the father and son team of W. H. Bragg and W. L. Bragg who provided the first successful interpretation of the diffraction patterns. The two groups respectively won the Nobel Prize in Physics in 1912 and 1914 for their work in developing the technique.

The theory of X-ray diffraction (XRD) relevant to the work of this thesis is introduced in this Section, with a particular emphasis on the central concept of the *structure factor*, leading into a discussion of *systematic absences* and how they can be used to identify crystal symmetries. The bulk of the discussion pertains

[†]Max von Laue was a student of Plank.
[‡]Walter Friedrich worked with Sommerfeld.
[§]Paul Knipping was a student of Röntgen – who discovered X-rays in 1895.

to diffraction from single crystals, however diffraction experiments can also be performed on polycrystalline samples as reviewed at the end of the chapter.

Before beginning the discussion with the structure factor it is useful to mention that diffraction patterns are generated by the interference of X-rays scattered from an ordered array of atoms, the periodicity of which is on the order of the wavelength of the X-ray. The genius of the Braggs was to imagine that diffraction patterns are generated by reflections of X-rays from *planes* of atoms in crystals. Crystals in diffraction experiments can therefore be thought of as three-dimensional diffraction gratings which have a periodic scattering density determined by the crystal structure. The periodic scattering density in a real crystal is related to its diffraction pattern in reciprocal space by a Fourier transformation from the real-space basis to the reciprocal-space basis.

2.2.1 Structure Factor

The Bravais lattice, $L(\mathbf{r})$, of a real crystal can be described by a three-dimensional Dirac comb which is constructed by placing delta functions at the points $\mathbf{R}$ in space where $\mathbf{R} = u\mathbf{a} + v\mathbf{b} + w\mathbf{c}$. Because an ideal crystal extends infinitely in all directions the lattice is summed over all space:

$$L(\mathbf{r}) = \sum_{u,v,w=-\infty}^{+\infty} \delta^3(\mathbf{r} - \mathbf{R}) \tag{2.9}$$

Upon each of the Bravais lattice points sits the basis, which contains N atoms placed at the fractional coordinates $\mathbf{r}_j = x_j\mathbf{a} + y_j\mathbf{b} + z_j\mathbf{c}$. Each of the atoms in the basis has an individual scattering density, $\rho_j(\mathbf{r}_j)$, which depends on its atomic number. The scattering density of the basis, $\rho_{bas}(\mathbf{r})$, is given by the sum of each of the atomic scattering densities contained within it:

$$\rho_{bas}(\mathbf{r}) = \sum_{j=1}^{N} \rho_j(\mathbf{r} - \mathbf{r}_j) \tag{2.10}$$

The scattering density of the crystal, $\rho_{cr}(\mathbf{r})$, is given by the convolution of the scattering density of the basis (2.10) with the Bravais lattice (2.9):

$$\text{crystal} = \text{basis} * \text{lattice} \tag{2.11}$$

$$\rho_{cr}(\mathbf{r}) = \rho_{bas}(\mathbf{r}) * L(\mathbf{r}) \tag{2.12}$$

According to the convolution theorem the Fourier transform of a convolution is described by the product of Fourier transforms:

$$\mathcal{F}\{\rho_{cr}(\mathbf{r})\} = \mathcal{F}\{\rho_{bas}(\mathbf{r})\} \cdot \mathcal{F}\{L(\mathbf{r})\} \tag{2.13}$$

which is useful when dealing with periodic functions. Starting with the right-hand term in the product, the Fourier transform of the real-space Bravais lattice describes a distribution of delta functions in reciprocal space:

$$\mathcal{F}\{L(\mathbf{r})\} = \sum_{h,k,l=-\infty}^{+\infty} \delta^3(\mathbf{k} - \mathbf{G}) \tag{2.14}$$

where the delta functions now sit on the reciprocal-space lattice points $\mathbf{G} = h\mathbf{a}^* + k\mathbf{b}^* + l\mathbf{c}^*$. The Fourier transform of the scattering density of the basis is a central concept in X-ray diffraction known as the *structure factor* and it is denoted, $\mathbf{F}(\mathbf{k})$:

$$\mathcal{F}\{\rho_{bas}(\mathbf{r})\} = \mathcal{F}\Big\{\sum_{j=1}^{N}\rho_j(\mathbf{r}-\mathbf{r}_j)\Big\} \tag{2.15}$$

$$= \int_{bas}\sum_{j=1}^{N}\rho_j(\mathbf{r}-\mathbf{r}_j)e^{i\mathbf{k}\cdot\mathbf{r}_j}d\mathbf{r} \tag{2.16}$$

$$\mathbf{F}(\mathbf{k}) = \sum_{j=1}^{N} f_j e^{i\mathbf{k}\cdot\mathbf{r}_j} \tag{2.17}$$

where f_j is the known as the atomic form factor which is related to the individual atomic scattering densities, $\rho_j(\mathbf{r}_j)$. The full expression for the structure factor of the crystal therefore is the product of (2.14) and (2.17):

$$\mathcal{F}\{\rho_{cr}(\mathbf{r})\} = \mathbf{F}_{cr}(\mathbf{k}) = \sum_{j=1}^{N} f_j e^{i\mathbf{k}\cdot\mathbf{r}_j}\cdot\sum_{h,k,l=-\infty}^{+\infty}\delta^3(\mathbf{k}-\mathbf{G}) \tag{2.18}$$

which, because of the delta function on the right-hand-side, means that the structure factor can only be non-zero when $\mathbf{k} = \mathbf{G}$. In other words this means that diffraction spots can only be observed at the reciprocal lattice points $\mathbf{G} = h\mathbf{a}^* + k\mathbf{b}^* + l\mathbf{c}^*$, allowing us to simplify (2.18) to:

$$\mathbf{F}(h,k,l) = \sum_{j=1}^{N} f_j e^{i\mathbf{G}\cdot\mathbf{r}_j} \tag{2.19}$$

$$\mathbf{F}(h,k,l) = \sum_{j=1}^{N} f_j \exp(2\pi i[hx_j + ky_j + lz_j]). \tag{2.20}$$

The importance of this result is that for each reciprocal lattice point there is a unique structure factor. The intensity of the observed reflections in diffraction patterns, $I(h,k,l)$, is the experimental observable which gives us access to the reciprocal lattice because it is proportional the square of the structure factor:

$$I(h,k,l) \propto |\mathbf{F}(h,k,l)|^2 \tag{2.21}$$

where the square of the magnitude is taken because the structure factor can take complex values. The observed intensities can therefore be used to construct an initial attempt at the scattering density in the basis through an inverse Fourier transformation. The structure factor cannot be directly reconstructed by measuring the reflection intensities because the imaginary part is not observable. The initial attempt is therefore refined by a least squares refinement of the structural parameters by comparison of calculated and observed structure factors generated by repeated cycles of Fourier transformation. For this reason progress in crystallography was for a long time tied to progress in developing fast-Fourier transform algorithms.

2.2.2 Systematic Absences

The structure factor given by (2.20) can be equal to zero for some specific sets of (h,k,l)s, in which case the scattering intensity cannot be directly observed. This is known as a *systematic absence*. Systematic absences are useful for determining the crystal symmetry because certain absences are caused by specific symmetry elements of the crystal structure. The rules relating systematic absences and their corresponding symmetry elements will not be discussed in detail here but a numerical example is given which relates directly to the $P2_1/c$ crystal structure determined in Chapter 7 of this thesis.

The two atoms in Figure 2.3 are related by a 2_1 screw-axis along the c-axis direction, which describes a mapping of atom 1 onto atom 2 by a rotation around the c-axis by 180° followed by a translation parallel to the rotation axis of $\frac{c}{2}$. Atom 1 sits at position (x,y,z) and atom 2 sits at position $(-x,-y,z+\frac{1}{2})$. Assuming that both atoms are the same species then we can set the form factor equal to one. If we consider a basis consisting of these two atoms then the structure factor

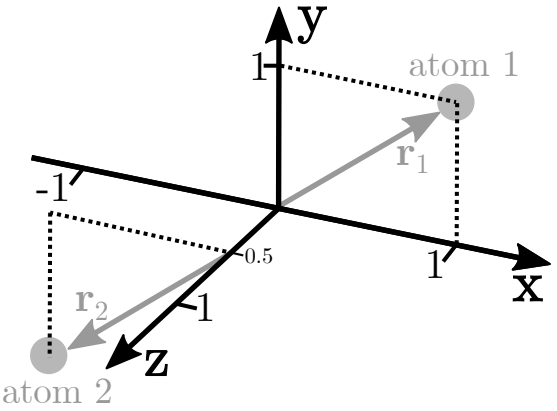

Figure 2.3: An illustration of a 2_1 screw-axis along the c-axis direction where atom 1 is mapped onto atom 2.

can be written in full by substituting in the atomic positions:

$$|\mathbf{F}(h,k,l)| = \sum_{j=1}^{N} \exp(2\pi i[hx_j + ky_j + lz_j]) \tag{2.22}$$

$$= e^{2\pi i(hx+ky+lz)} + e^{2\pi i(-hx-ky+lz+\frac{l}{2})} \tag{2.23}$$

$$= e^{2\pi i(hx+ky+lz)} + e^{-2\pi i(hx+ky-lz-\frac{l}{2})} \tag{2.24}$$

$$= e^{2\pi i(hx+ky)}e^{2\pi i(lz)} + e^{-2\pi i(hx+ky)}e^{2\pi i(lz)}e^{2\pi i(\frac{l}{2})} \tag{2.25}$$

$$= e^{2\pi i(lz)}[e^{2\pi i(hx+ky)} + e^{-2\pi i(hx+ky)}e^{\pi il}] \tag{2.26}$$

Then, for the set of reflections $(00l)$:

$$|\mathbf{F}(0,0,l)| = e^{2\pi i(lz)}[e^{2\pi i(0x+0y)} + e^{-2\pi i(0x+0y)}e^{\pi il}] \tag{2.27}$$

$$= e^{2\pi i(lz)}[e^{0} + e^{0}e^{\pi il}] \tag{2.28}$$

$$= e^{2\pi i(lz)}[1 + e^{\pi il}] \tag{2.29}$$

Equation (2.29) shows that the reflection from all $(00l)$ planes will vanish when the term in the square brackets is equal to zero, i.e. when $e^{\pi il} = -1$. Using

the trigonometric identity,

$$e^{\pi i l} = \cos(\pi l) + i \sin(\pi l) \tag{2.30}$$

$$= -1 + 0 \qquad \text{for all odd values of } l \tag{2.31}$$

we can see that the structure factor $|\mathbf{F}(0,0,l)|$ vanishes for all odd values of l. Thus a screw axis parallel to the c-axis will affect the $(0,0,l)$ reflections, and in fact all set of planes $(0,0,l)$ with $l =$ odd will have zero scattering intensity in this 2_1 screw-axis example.

To give a brief conceptual description of the same example we can consider Figure 2.4 in which the 2_1 screw-axis operation has been repeated a number of times to build up a periodic pattern of atoms. Clearly a suitable basis to describe the pattern contains two atoms, one with a negative x-coordinate and one with positive x-coordinate. However, if *only the z-coordinate* of the atoms is considered then the size of the repeating unit cell is halved in real-space along the c-direction, which therefore doubles size of the reciprocal unit cell along the c*-direction, thus recovering the systematic absence of *every other* $(0,0,l)$ reflection.

This is a specific example of the more general observation that the choice of unit cell determines the observed systematic absences. In practice, the choice of unit cell is determined by the observed symmetry of the reciprocal lattice, plus other considerations such as choosing the highest symmetry. The choice of unit cell has no effect on the observed diffraction pattern, yet a number of unit cells may be chosen to describe the same crystal structure. The reflections in the diffraction pattern occur at the reciprocal lattice points of the *primitive* reciprocal lattice, which defines the primitive reciprocal cell. If a unit cell in real-space is chosen which is twice the size of the primitive unit cell, then the corresponding reciprocal unit cell is described by a reciprocal lattice containing twice as many

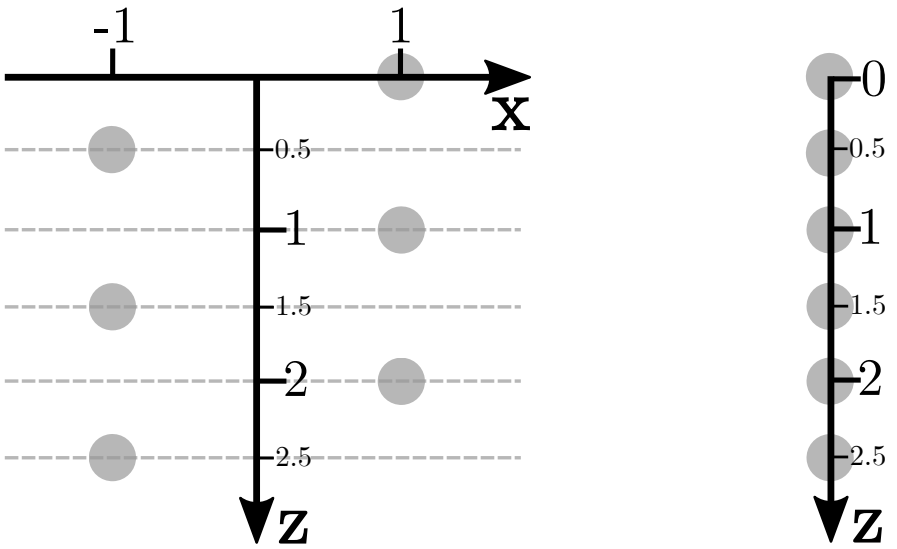

Figure 2.4: Left: the 2_1 screw-axis operation has been repeated to build up a periodic pattern of atoms. **Right:** The same periodic pattern when considering only the z-coordinate.

lattice points as the *primitive* reciprocal lattice. The crystal structure and diffraction pattern remain unchanged by this choice, and the additional lattice points resulting from the choice of a non-primitive unit cell correspond to reflections with zero intensity, i.e. systematic absences.

2.2.3 Polycrystalline XRD

As mentioned in the introduction to this section XRD can also be performed on polycrystalline samples. Polycrystalline (or 'powder') samples ideally contain many thousands of crystallites oriented essentially randomly. The reflections corresponding to each set of planes (h, k, l) in a powder sample are projected along a cone for the same scattering angle of 2θ about the incident beam, resulting in a diffraction pattern of concentric rings rather than spots. An example diffraction pattern is given in Figure 2.5 in which both polycrystalline rings and single-crystal spots are visible.

Polycrystalline diffraction data are useful in the determination of the unit cell dimensions given the crystal system and the Miller indices (h, k, l) of the

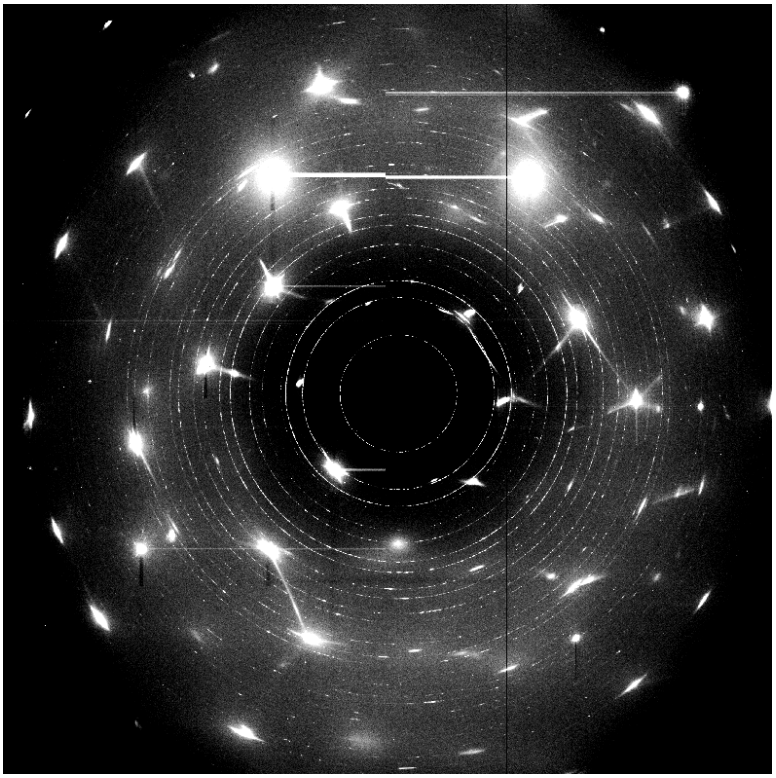

Figure 2.5: An example diffraction-pattern from the contributing work. The pattern contains both powder diffraction rings (from $Xe(N_2)_2$ – see Chapter 5) and single-crystal diffraction spots (from xenon).

reflection. The inter-planar spacing, d_{hkl}, may be calculated for each observed reflection because it is related to the scattering angle by the Bragg condition:

$$2d_{hkl}\sin(\theta) = n\lambda, \tag{2.32}$$

and it is related to the unit cell dimensions as a function of the Miller indices. For example, in an orthorhombic crystal system, where $a \neq b \neq c$ and $\alpha = \beta = \gamma = 90°$ the relation is given by:

$$\frac{1}{d_{hkl}^2} = \frac{h^2}{a^2} + \frac{k^2}{b^2} + \frac{l^2}{c^2}. \tag{2.33}$$

Determining the unit cell dimensions is often the first step in determining a real crystal structure from XRD data. Single-crystal diffraction data are gen-

erally more beneficial than polycrystalline diffraction data because the unique reflections enable the determination of the atomic positions within the unit cell. The disadvantage with polycrystalline data is the overlap of peak positions once the data are reduced into 2D. Because information is lost it may not be possible to observe systematic absences, which means that the space group cannot be determined and therefore neither can the atomic positions. The peak intensities also carry information about the atomic species in the crystal which may not be reliably determined from polycrystalline data, again due to overlap.

The overlap problem is exacerbated at pressure due to broadening of the reflections at higher pressures due to the onset of non-hydrostaticity in the sample. Under non-hydrostatic conditions the stress in the sample is greatest along the axis of compression, which means that different randomly oriented crystallites experience the maximal stress along different crystallographic directions, thus exhibiting a distribution of inter-planar spacings, d_{hkl}, for the same sets of planes, which is observed as a broadening of the diffraction rings. Single-crystal reflections also broaden with increasing pressure but because they are distributed in 3D space the overlap is less detrimental. The advantage of single-crystal diffraction data over polycrystalline diffraction data is illustrated in Figure 2.6. As the full width at half maximum (FWHM) of the reflections is increased in Figure 2.6, not only do the individual reflections become indistinguishable but the intensities of those reflections are also obscured.

The experimental methods associated with acquiring and handling XRD data, including producing intensity *vs.* 2θ plots as shown in Figure 2.6, are detailed in experimental section 3.5 in the next Chapter.

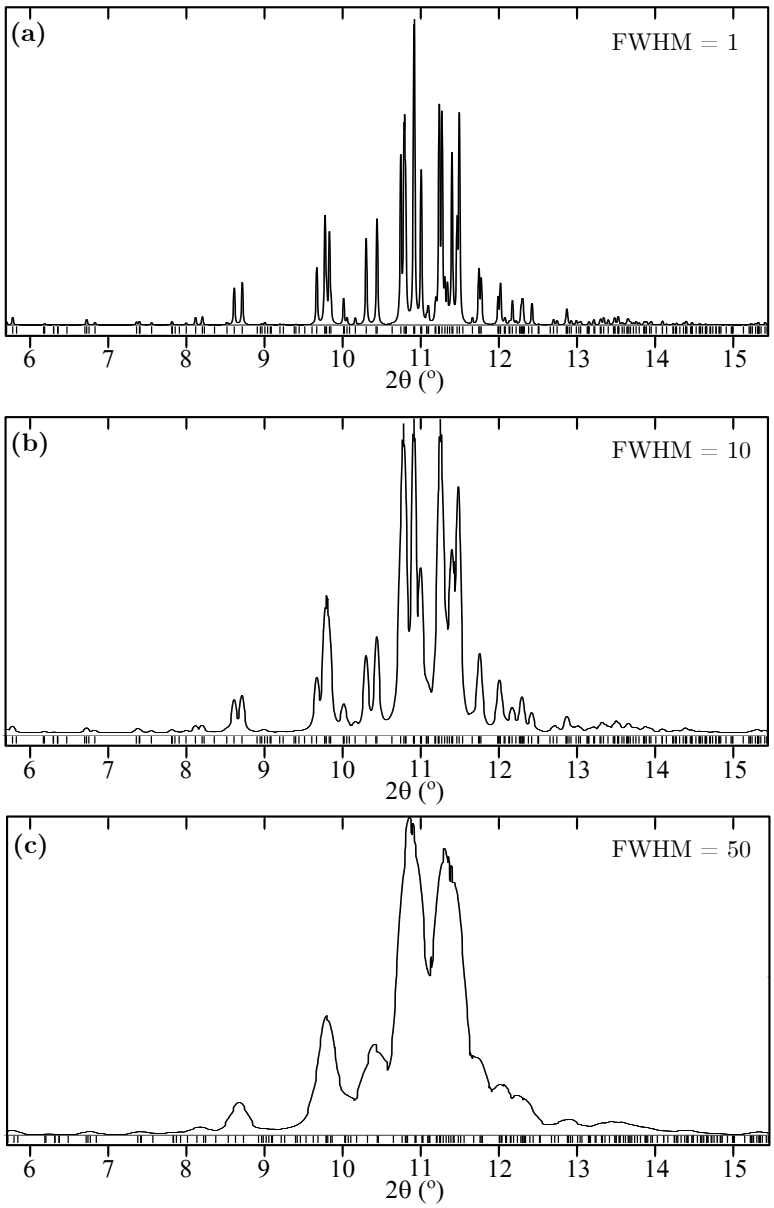

Figure 2.6: Simulated diffraction intensity *vs.* 2θ plots for the same crystal structure fitted with different peak widths. The FWHM of the diffraction peaks increases progressively from panel (a) to panel (c) as indicated. **(a)** Illustrates single-crystal diffraction data. **(c)** Illustrates broadened polycrystalline data.

Chapter 3

Experimental Techniques

The purpose of this chapter is to provide the reader with an overview of the experimental techniques used in the contributing work. The first half of the chapter covers high-pressure and high-temperature techniques, and the second half gives an experimental overview of the Raman and XRD diagnostics introduced in the previous chapter.

3.1 Diamond-Anvil Cells

The extreme static pressures generated in the contributing work were generated in diamond-anvil cells (DACs). DACs can produce high pressures in the laboratory by applying a large uniaxial force over a small area, which follows from the simple relation $P = F/A$. Anvil devices were pioneered by Percy Bridgeman[†] [Mcmillan 05] who originally used tungsten carbide anvils before they were first replaced by diamonds in 1959 [Jamieson 59, Weir 59]. The shift towards diamond anvils probably played a large part in the proliferation of DACs in high-pressure research. Diamonds are incredibly hard, which makes them an ideal anvil material,

[†]Bridgeman is considered one of the founders of modern high-pressure physics and was awarded the 1946 Nobel prize in physics for his contributing work to the development of high-pressure apparatus.

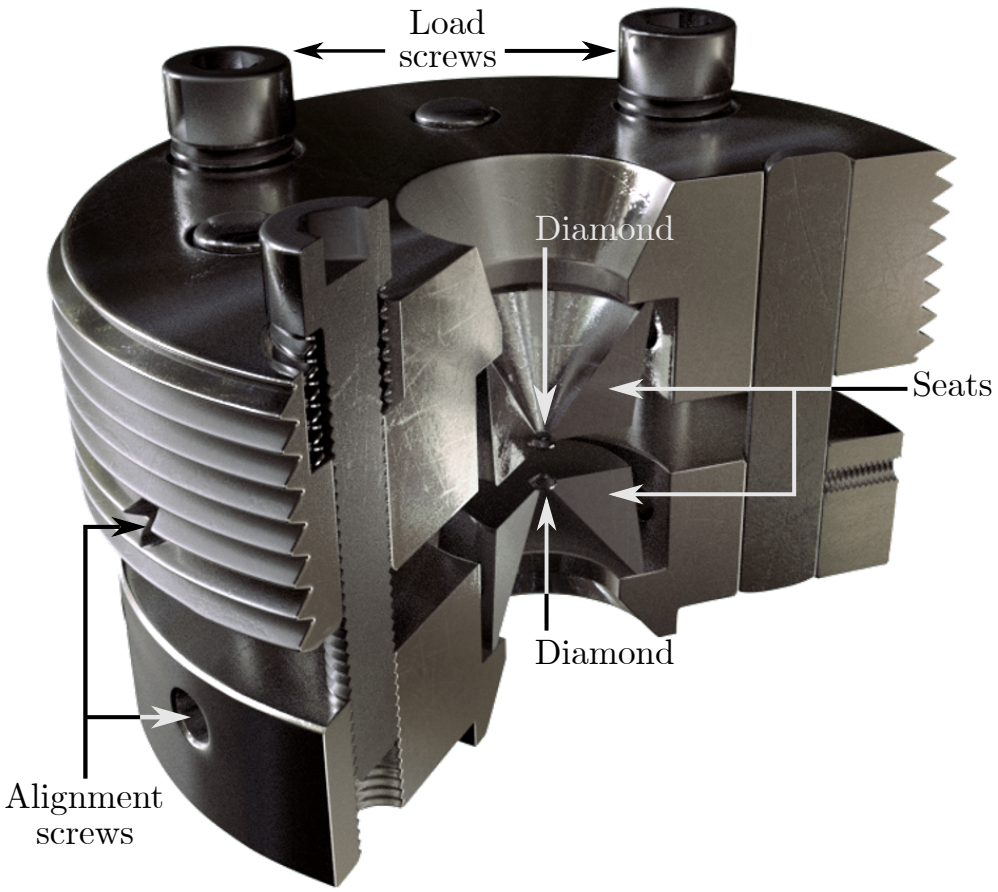

Figure 3.1: A cross-section illustration of a typical four-post symmetric-type DAC used in the contributing work.

but they are also transparent to large regions of the electromagnetic spectrum, allowing high-pressure samples to be probed *in situ* by spectroscopic diagnostics such as Raman spectroscopy and XRD as discussed in the previous chapter. The use of diamond anvils has enabled the experimentally achievable pressures to be pushed two orders of magnitude from the days of Bridgeman, and recent experiments using double-stage anvils reached record static pressures in excess of 1 TPa (1000 GPa) [Dubrovinskaia 16].

DACs have been prevalent in high-pressure science since the 1980s [Jayaraman 83] and many different designs exist which are each tailored towards specific experiments. For example the *Merrill-Bassett* cell was originally designed for

XRD experiments on single crystals under hydrostatic pressure [Merrill 74]. The four-post *symmetric-type* DAC shown in Figure 3.1 is also well suited for XRD experiments because its flat geometry allows the cell to be rotated over a large angle of $\sim 70^\circ$ without cutting the incident beam, and it can reach higher pressure than the Merrill-Basset cell. The XRD compatibility comes at the cost of a less reproducible alignment compared to other types of cells such as *piston-cylinder* cells, which can make achieving megabar pressures in symmetric-type DACs very challenging. If the diamond culets are not perfectly aligned along the axis of compression they are much more likely to break as pressure is increased. The symmetric-type DAC shown in Figure 3.1 was the main type used in the contributing work. Piston-cylinder cells were also used for megabar experiments, as shown in Figure 3.2a, along with a simple schematic of the sample-chamber and gasket clamped between the diamonds.

Ensuring that the DAC geometry is suitable for use with the desired diagnostics is one of a number of crucial factors which needs to be considered before preparing high-pressure experiments. Other important factors include, for example, the *diamond geometry*, which largely determines both the pressures which may be achieved and the diagnostics which may be used. When high-temperatures are required, the choice of *heating technique* requires careful consideration, along with the possible *pressure control methods* and suitable *pressure gauges*. It is also important to consider suitable *loading techniques*, which can vary immensely depending on the sample. Each of these key considerations is discussed in more detail below.

Diamond geometry — The size of the diamond culet is the key consideration regarding the targeted pressure range. Smaller culets can be pushed to higher pressures than larger culets, although the sample can be consequently an order of magnitude thinner, shortening the optical path length and making both Raman and XRD experiments more challenging. When XRD experiments are planned it is necessary to use Boehler-Almax (BA) diamonds [Boehler 04] in combination with the symmetric-type DAC mentioned above. BA diamonds are specifically

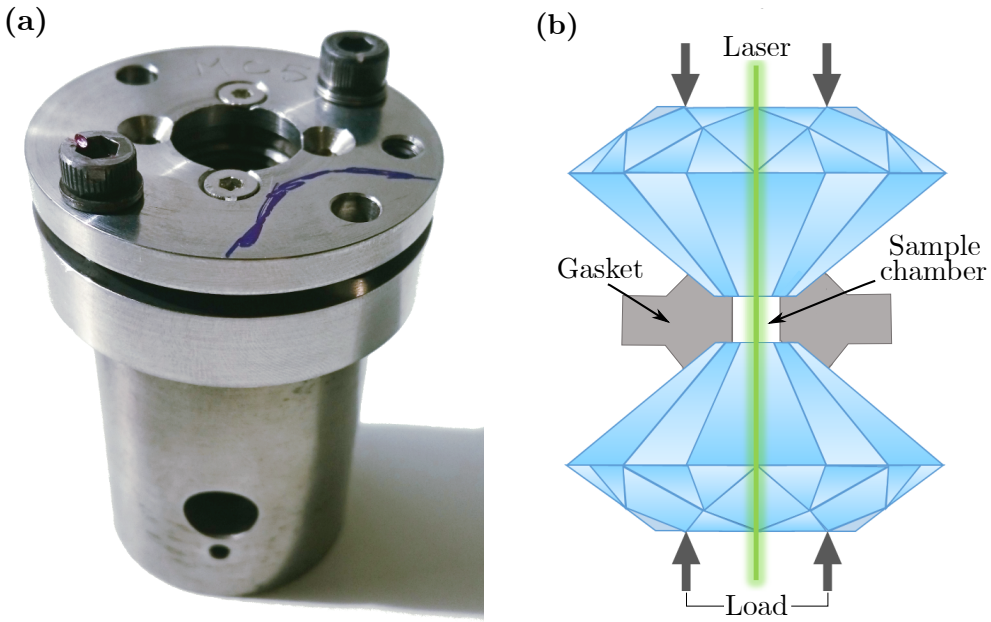

Figure 3.2: **(a)** Photograph of a typical piston-cylinder DAC used in the contributing work. **(a)** A schematic illustration of the basic operating principle in DACs.

made with conical supports which offer larger viewing apertures to the sample when paired with wide-opening seats as shown in the earlier Figure 3.1. Most culets used in the contributing work were around 200 μm, although smaller culets around 40 μm were also used for some megabar Raman experiments.

Gasket geometry and material — The sample, which is compressed between the two uniaxial anvils, is surrounded by a gasket typically made from a high tensile strength material. In all experiments of the contributing work rhenium foil was used as a gasket material, in some cases sputtered with gold to prevent hydrogen diffusion [Scheler 11]. Rhenium remains ductile at high pressures and has a very high-melting point. To prepare the sample chamber the rhenium foil, usually between 200-300 μm thick, was clamped between the two anvils up to a pressure of approximately 30 GPa and then released. A circular hole approximately 50% of the diameter of the diamond culets was cut into the centre of the impression using a pulsed IR laser, followed by ultrasonication in water and then acetone to remove any ablation fragments. The desired chamber thickness was typically around $10-15\%$ of the culet diameter to ensure an optimal amount

of sample with minimal risk of uneven chamber collapse on compression.

The sample chamber thickness was measured using the standard interferometry technique whereby the empty sample chamber is clamped between the two diamond anvils and a spectrum of visible light is sent through the optical cavity. The diamond culets reflect some of the light and the cavity acts as a Fabry-Perot interferometer [Hernandez 88]. The intensity of the light which passes through the cell is detected and plotted as a function of wavelength and transition maxima are observed for the wavelengths for which an integer multiple fits between the diamonds. Minima are observed where the cavity length is an integer multiple plus a half, thus the observed interference pattern (as shown in Figure 3.3) can be used to determine the optical path length.

This technique was later used to confirm that xenon had been successfully loaded into DACs. Xenon is Raman inactive but dense xenon has a higher refractive index that air. Therefore, following the above procedure, the measured gasket thickness would give an *apparent* increase on successful loading on xenon, as seen in Figure 3.3. For a more detailed description of the xenon-loading procedure the reader is referred to section 3.2.3.

Pressure control methods — The choice of pressure control method depends on the desired P-T conditions and the planned diagnostics. The simplest method of increasing pressure is to apply load to the diamonds by tightening the load screws of the cell. This method is was most frequently used when indenting and preparing the gasket prior to loading the sample, however this method can slightly misalign the diamonds away from the compression axis, particularly when working with the symmetric-type DACs. Additionally, this method is also subject to a large hysteresis because some of the applied load is lost to friction between the screws and the cell, making decompression experiments challenging.

The main alternative when performing Raman experiments in a piston-cylinder type DAC is the lever-arm, a device which allows fine incremental pressure control

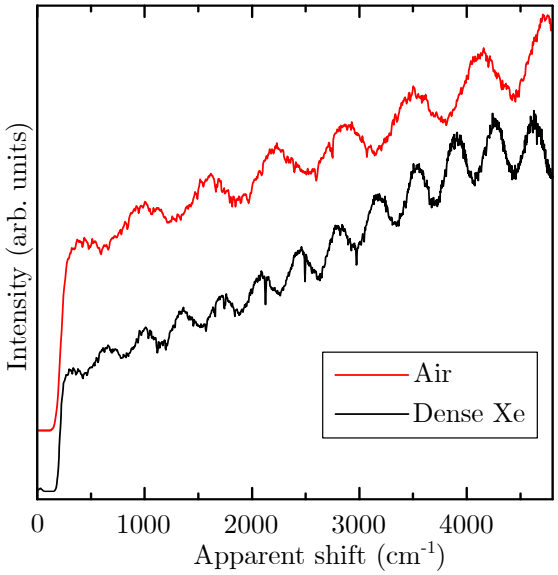

Figure 3.3: Example interference patterns used for measuring the gasket thickness. The red spectrum was acquired from an empty gasket chamber of thickness 8 μm. The black spectrum was acquired from the same gasket chamber after successfully loading dense xenon, showing an apparent thickness of 14 μm.

by turning a screw which actuates a lever and pressing-plate mechanism which uniaxially drives the piston into the cylinder. Lever-arms are compatible with either room or high-temperature experiments and provide an evenly applied load across the cell. The main disadvantage of the lever-arm is that the load must be transferred to the load-screws if the cell needs to be moved whilst at high pressure, which can be tricky and potentially lead to over compression and anvil failure, or pressure decrease and loss of the sample.

Lever-arms are not compatible with symmetric-type DACs and, when performing high-temperature experiments, increasing pressure using the load-screws should not be attempted because the cell may be extremely hot *and* connected to a high-current power supply. Even if it were possible to adjust the pressure by this method the potential misalignment might also prematurely end the experiment. Therefore, the best pressure control method for high-temperature experiments in symmetric-type DACs is through the use of gas-membranes. Gas-membranes allow small incremental loads to be applied remotely through controlling the pressure in a membrane which sits tightly between the cell and the canister which

is attached via the large screw thread on the outside of the cell shown in Figure 3.1. (The canister is later seen in Figure 3.7.) Gas-membranes can be used in addition to applying load on the load-screws. As mentioned above, some of the load on the screws is lost to friction within the cell. When gas-membranes are used during high-temperature experiments, the internal friction from the initial compression on load-screws tends to 'relax', which allows additional pressure from the gas-membrane to be automatically transferred to the load-screws upon cooling. The necessary use of gas-membranes during high-temperature experiments with symmetric-type DACs also precludes the use of external heaters because the gas-membrane assembly surrounds the entire DAC.

3.1.1 Pressure Gauges

In the contributing work two different techniques were used to determine the sample pressure: 1) the ruby luminescence scale and 2) the diamond edge scale. Both techniques are briefly described below.

Ruby Luminescence Scale — The formula of ruby is aluminium oxide (Al_2O_3) doped with chromium, where Cr^{3+} ions substitute for the Al^{3+} ions. The optical spectra of ruby have been studied extensively since its application in the first solid state laser, and due to the precense of the Cr^{3+} ions ruby exhibits the distinctive R_1 and R_2 emission shown in Figure 3.4a. The ruby luminescence scale allows *in-situ* pressure measurements to be made when a small amount of ruby is included within the sample chamber because the wavelength of the R_1 emission line is both pressure-dependent and easily observable with little modification to the types of Raman set-ups (discussed in section 3.4) commonly used in high-pressure experiments. The pressure-dependence of the R_1 fluorescence line of ruby has been reviewed extensively [Syassen 08] and is probably partly responsible for the proliferation of DACs in high-pressure research. Ruby is a chemically inert material and as such may be safely added to most samples without affecting their chemistry, however, smaller samples such as those in megabar experiments have

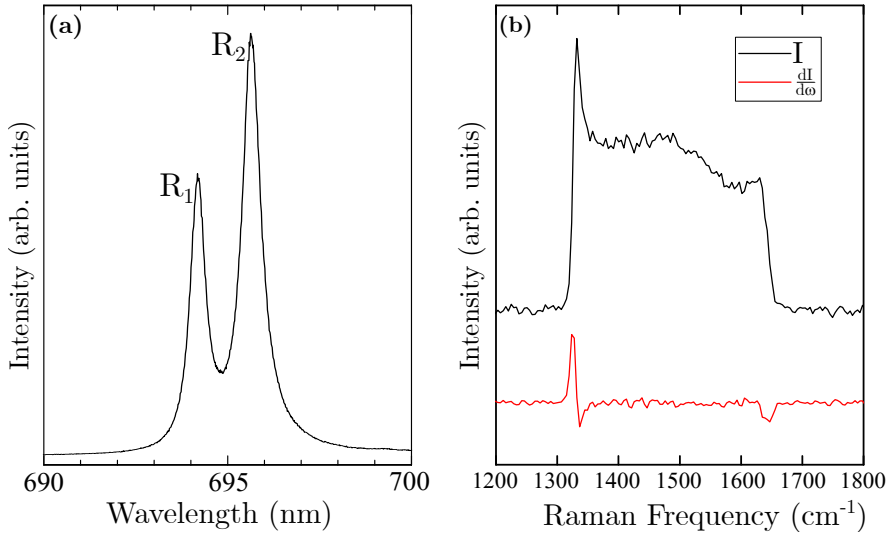

Figure 3.4: Spectra showing (a) the characteristic ruby luminescence at ambient pressure, and **(b)** the first-order diamond phonon at 168 GPa.

limited sample volume which may preclude the addition of any pressure gauge.

The fluorescence wavelength, which sits at 694.2 nm under ambient conditions, is also sensitive to temperature, therefore precluding its use in high-temperature experiments where the R_1 and R_2 lines broaden sufficiently to become indistinguishable [Datchi 07]. At extreme pressures the R_1 line becomes very broad again, limiting its use to pressures below 100 GPa. Interestingly, the fluorescence line of ruby is also sensitive to the amount of Cr^{3+} doping and in the contributing work zero-pressure wavelengths were recorded before beginning experiments.

Diamond-edge Scale — The second scale used in the contributing work is known as the *diamond-edge* scale. The technique is similar to the ruby luminescence scale in that it allows *in situ* pressure measurements to made in DACs without modification to the Raman set-up. The scale is based on observing the first-order phonon line of diamond, as shown in Figure 3.4b. The first-order phonon exhibits a pressure-dependent wavelength which has been revised and extended by Akahama *et al.* [Akahama 04, Akahama 06, Akahama 10].

The phonon line of diamond is observed at 1332 cm^{-1} under ambient conditions and is thus observable simultaneously with Raman modes of interest from

samples, allowing for real-time *in-situ* pressure measurement. Unlike the ruby fluorescence line, the diamond phonon has a very weak dependence on temperature [Liu 00] and was used as the pressure gauge in high temperature experiments in the contributing work.

A typical diamond spectrum used for pressure measurement is shown in Figure 3.4b, in which the edge towards higher frequencies arises from the stressed diamond culet. The wavelength that corresponds to the edge is chosen such that it corresponds to the minimum in the first-derivative of the observed intensity with respect to the wavelength (shown in red), as first suggested by Akahama *et al.* [Akahama 04]. The observed spectrum depends heavily on the spatial filtering of the Raman set-up as discussed later in section 3.4. The broadness of the observed peak reflects the fact that the strain profile through the anvils is not constant, i.e. the pressure is highest at the culet and lowest at the back of the diamond (the table). Spatial filtering in the experimental Raman set-up attempts to removed scattering which does not arise from the diamond culet.

3.2 Sample Loading

Each of the three systems studied in this thesis (N_2, N_2–Xe and N_2–H_2) required very different loading techniques, each of which is now described in the following subsections.

3.2.1 Cryogenically Loading Liquid-nitrogen

Nitrogen can be loaded into DACs via cryogenic loading or gas loading techniques. Both techniques aim to maximise the initial sample density upon loading. In the cryogenic loading technique the initial sample density is increased by condensing nitrogen at 77 K and ambient pressure. In the gas loading technique (described below) the initial sample density is increased by pressurising nitrogen gas at

ambient temperature to 0.2 GPa (2 kbar). Both techniques provide similar initial sample densities for nitrogen. Maximising the initial sample density is beneficial for both spectroscopy and XRD experiments because it increases the optical path-length of the sample, thus increasing the intensities of both spectral lines and diffraction spots. The denser initial sample also helps to minimise the gasket collapse which occurs on compression. Excessive gasket collapse potentially leads to asymmetrical sample chambers and eventual sample loss, particularly in high-temperature experiments. The cryogenic loading technique was used to load pure nitrogen in the contributing work contained in Chapter 7 because the geometry of the built-in resistive heater precluded gas loading.

The general procedure for cryogenically loading liquid nitrogen is as follows: Once aligned and prepared with a suitable gasket the DAC is placed on a hot-plate at around 50°C for 10 minutes to remove any moisture from the cell body. This is important to a) prevent water contamination of the sample and b) to prevent the load-screws from freezing tight during the final stage of the loading. The open DAC is then sealed into a cryogenic vessel and purged with gaseous research-grade nitrogen for a further 5 minutes. Once the vessel is purged, the nitrogen pressure in the vessel is raised to between 0.5 - 1 bar. The vessel is then submerged in liquid nitrogen, which decreases the vessel temperature sufficiently to condense the gaseous nitrogen contained within, thereby submerging the DAC. The DAC is then closed via the load-screws and allowed to slowly warm up to room temperature. The DAC is once again dried on a hot plate if resistive-heating experiments are to be conducted.

3.2.2 Gas Loading

Gas loading has the advantage over cryogenic loading that mixtures of known composition can be prepared before loading. The gas loading technique used in the contributing work used a set-up based on the design on Mills *et al.* [Mills 80]. Gas loading can be conducted with most chemical species which are gaseous at

ambient conditions and it therefore does not suffer from the tight constraint of cryogenic loading which is limited to systems which are liquid (or solid) at 77 K.

The general procedure for gas loading is as follows: The calibrated DAC, which is left open, is sealed in a large vessel which is pressurised with the loading-gas to 2000 bar (0.2GPa). The DAC is then closed whilst inside the sealed vessel by a stem-driven gear mechanism. The high-pressure vessel is then vented and the DAC can be removed. This method of loading was used for the nitrogen-hydrogen mixtures in Chapter 6.

3.2.3 Cryogenically Loading Solid Xenon and Additionally Gas Loading Nitrogen

The Xe-N_2 samples of Chapter 5 were loaded into DACs using a two-stage process developed specifically for the project which involved both cryogenically-loading solid xenon, and gas loading nitrogen as discussed above.

In the first stage, solid xenon is cryogenically loaded into the DAC under a dry nitrogen atmosphere inside a glove-bag. The general procedure is as follows: the calibrated DAC is dried on a hot-plate to prevent contamination of the sample with water-ice and to prevent the load-screws from freezing tight. The DAC is then moved into a nitrogen filled glove-bag which is purged with nitrogen at least three times. The DAC is then placed open, on its side, into a polystyrene tray which is then filled with liquid N_2 until a few millimetres below the height of the diamond culets. Once the DAC and diamonds cool to the liquid N_2 temperature, gaseous xenon is blown onto the diamonds culets where it solidifies on contact. (The freezing point of xenon under standard conditions is 161 K.) The solid xenon is then clamped in the DAC. Pure xenon is Raman inactive so the loading is confirmed by comparison of the refractive index within the sample chamber before and after loading using the interferometry technique for measuring gasket thickness discussed earlier. The xenon loading is checked for contamination via

Raman spectroscopy before continuing to the second stage of the loading process.

In the second stage of the loading, nitrogen gas is additionally loaded into the cell at 0.2 GPa using the high-pressure gas loading system. The general procedure for gas loading nitrogen on top of the xenon generally follows that described in the previous section, however the DAC, which in this case is initially closed when it is put into the gas-loaded, must be *partially* opened once the pressure inside the gas-loader is at 0.2 GPa so that *some* xenon is allowed to escape from the sample chamber to be replaced by N_2. This two-step loading-technique therefore requires calibration of the load-screws for gas loading before loading the cryogenic xenon.

The partially-open state of the DAC can be identified by the appearance of coloured-fringes on the gasket when in contact with the diamonds. However, the coloured-fringes can appear over a range of applied loads which affects the rate at which xenon can escape the sample chamber. Consequently, when partially opening the xenon-loaded cell in the high-pressure gas-loader there were two competing factors to consider: 1) how much to open the cell by, and, 2) how long to open the cell for.

One major disadvantage of this loading technique compared to gas loading mixtures is that the molar ratio of xenon to nitrogen could not be controlled, as discussed further in Chapter 5. However, the great advantage is that only a minimum volume of xenon is wasted, and xenon is extremely expensive. Gas loading can be wasteful unless extensive efforts are made to recycle the gas which is not loaded into the DAC, but the recycling process was not possible with the single xenon cylinder available.

3.3 High-temperature Techniques

Until now only high-pressure techniques have been discussed. It is possible to explore the behaviour of systems across pressure-temperature (P-T) space through the generation of simultaneous high-pressure high-temperature conditions in DACs using various heating techniques. For example, the extreme conditions at the centre of the earth were recently replicated experimentally by heating samples of iron to 5700 K at 377 GPa [Tateno 2010]. A number of different heating techniques are compatible with DACs, including: *laser-heating* [Bassett 01], *internal resistive-heating* [Zha 03], and *external resistive-heating* [Dubrovinskaia 03]. Each technique was used at various points in the contributing work, and each has its own advantages and disadvantages as discussed here.

Laser-heating — Laser-heating can be used to achieve the highest temperatures ($>$ 2000 K) by rapidly transferring energy from a pulsed laser to the sample. Laser-heating can be conveniently performed on most DAC designs without the need to modify or prepare the cell in any way, however it is often difficult to accurately measure the temperatures achieved because the heating can be extremely localised within the sample, causing large thermal gradients which decay very rapidly because of the high thermal conductivity of the diamond anvils. The diamonds may break in laser-heating experiments because of the extreme temperature gradients or they may also 'graphitise' depending on the experiment. If the sample is very transparent then it may be necessary to include a metallic coupler inside the sample which may chemically react in unpredictable ways at extreme conditions, thus contaminating the sample.

Resistive-heating — Elevated-temperatures (up to $\sim$1200 K) may be achieved through resistive-heating techniques. External resistive-heaters surround the body of the DAC and can be driven up to around 800 K. Internal resistive-heaters can reach temperatures in excess of 1000 K and are often used in combination with external heaters. One of the main advantages of resistive-heating techniques

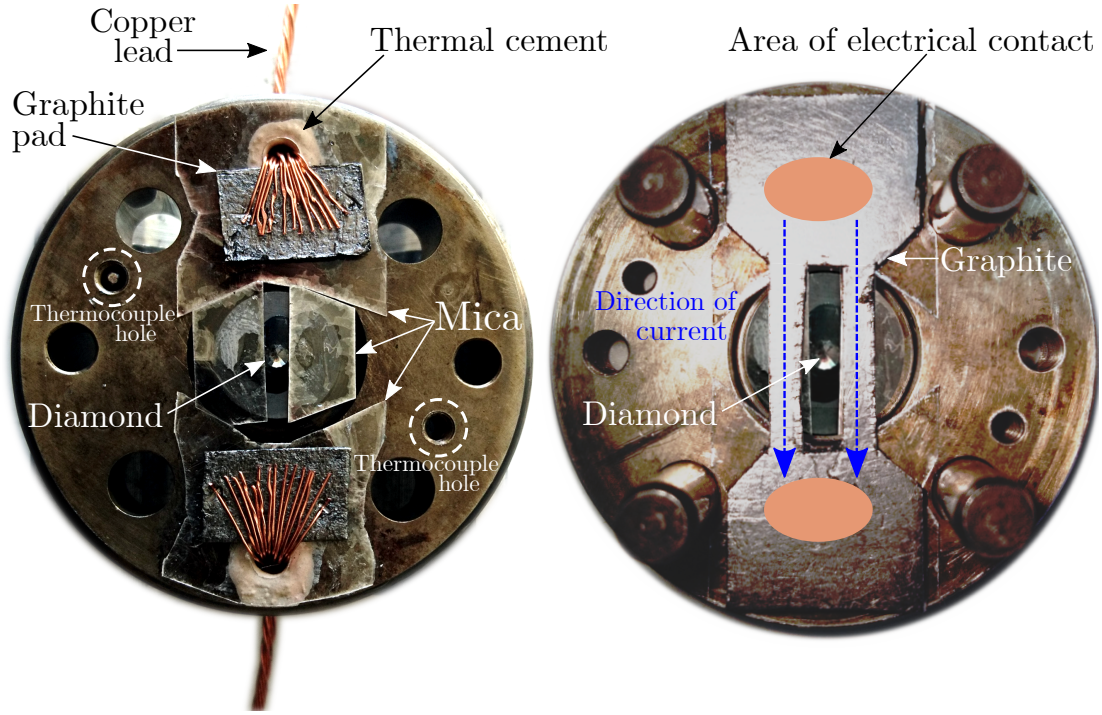

Figure 3.5: The top (left) and bottom (right) halves of a modified four-post symmetric-type DAC made of René-41 and equipped with a graphite heater. (Thermal cement has not yet been applied in the photo in order to better display the components.)

is the lack of thermal gradients across the sample chamber giving almost isotropic *P-T* conditions across the sample, effectively allowing the whole sample to be in thermodynamic equilibrium at least with itself. One of the main challenges associated with resistive-heating is thermal losses to the environment. Because the DAC is necessarily in thermal contact with the experimental set-up, which primarily consists of metallic components which may be water-cooled, a lot of the thermal energy which is pumped into the system can be lost to the environment. A typical sample chamber has a volume of only a new nanolitres, but because of thermal loss to the environment it is often necessary to power tens of Watts through the heaters for a few minutes to reach the desired temperatures.

The primary high-temperature technique used in the contributing work of this thesis was resistive-heating using graphite-heaters, as shown in Figure 3.5. As mentioned in the previous section symmetric-type DACs are necessary for XRD experiments because of their flat geometry. The limited space between the

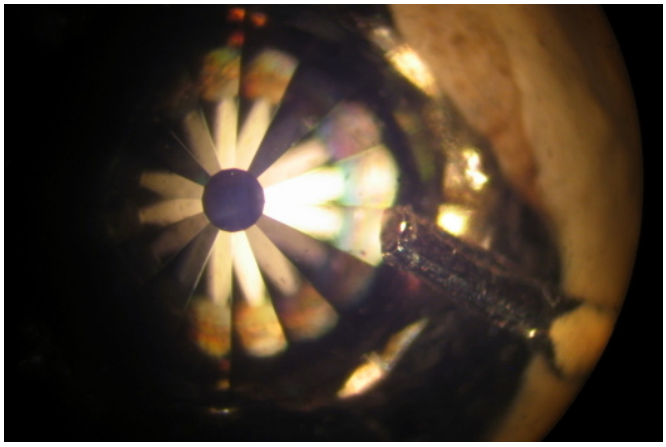

Figure 3.6: A photograph showing the proximity of the thermocouple (right) to the diamond culet (left). The green-ish ring on the diamond shows the depth of the diamond when pushed into the gasket and shows that the thermocouple could not be closer to the sample chamber.

two halves of a symmetric-type DAC is typically between 2-3 mm when closed, thus precluding the use of molybdenum-coil internal-resistive heaters (which also require narrow opening seats unsuitable for XRD experiments). Graphite sheets are thin and may be installed between the two halves of symmetric-type DACs, as shown in Figure 3.5.

The graphite sheet passes through either side of the sample and is made thinnest closest to the centre of the DAC. A current is supplied to the graphite through the copper-leads connected to a power-supply. The copper-leads and the graphite sheet are insulated from the cell using mica sheets and thermal cement which is thermally conducting and electrically insulating. The DAC shown in Figure 3.5 was modified to allow a thermocouple to be inserted through the top-half of the cell through either of the two smallest holes (as indicated in Figure 3.5) in order to be fixed in contact with the diamond near to the sample-chamber for more accurate temperature-measurement. The proximity of the thermocouple to the diamond culet is shown in Figure 3.6. Heaters of this type were successfully used in the work of Chapter 7 to achieve temperatures around 750 K at pressures around 70 GPa. A photograph of the DAC at the maximum temperature is shown in Figure 3.7.

Figure 3.7: A symmetric-type DAC equipped with a graphite heater. **(a)** After completion of a high-temperature Raman experiment. **(b)** During a high-temperature experiment. The green light is from the 514 nm laser. Note the red-hot copper leads as the sample reaches 750 K.

3.4 Experimental Raman Set-up

The Raman set-up used in the contributing work is illustrated in Figure 3.8. The function of each optical component is discussed stepwise according to the path of the laser beam, from the initial excitation to the final detection of the Raman scattered light. A more general review of experimental high-pressure Raman spectroscopy systems can be found in ref. [Goncharov 12].

The majority of Raman experiments in the contributing work were conducted using the 514 nm (green) excitation wavelength of an Argon ion laser. At higher pressures the laser excitation can cause the diamond anvils to fluoresce sufficiently to mask useful Raman signal, in which case the longer 647 nm (red) excitation wavelength of a Krypton ion laser was used to minimise the observed diamond fluorescence. Both lasers were typically used at powers around 25 mW.

The unfiltered laser beam is not perfectly monochromatic and is therefore passed through the first optical component which is a holographic Band Pass Filter (labelled *BPF* in the top-centre of Figure 3.8) which reflects only the

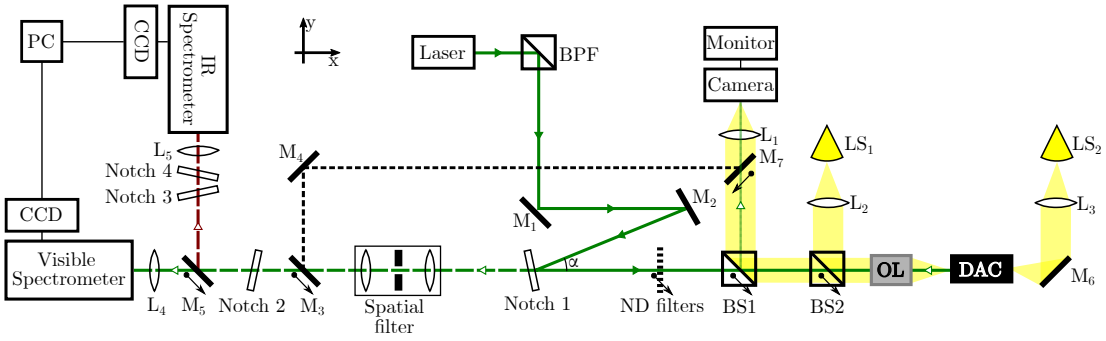

Figure 3.8: A diagram of the Raman set-up used in the contributing work. It operates in a 180° backscattering geometry with a 'Z'-configuration for beam filtering.

desired wavelength at a right-angle to the indecent beam, whilst scattering off the unwanted modes.

The monochromatic beam is then reflected through the "Z" configuration, consisting of mirrors *M1* and *M2* and the holographic notch filter (labelled *Notch 1*). The angle marked α is dictated by the notch filter which serves two functions at that specific angle. The first function of *Notch 1* is to reflect the incident beam into the x-direction of the set-up so that it can be incident on the sample. It acts similarly to the *BPF* in the sense that it reflects only the desired wavelength. The second function of *Notch 1* is to transmit only Raman scattered from the sample that is travelling to the left along the x-direction, thus discarding the unattenuated Rayleigh scattering. Practically, the Notch filter actually reflects a spectrum of radiation centred on the Rayleigh line which is approximately 200 cm^{-1} wide, therefore (anti-)Stokes shifts down to around 100 cm^{-1} may be observed using notch filters.

After reflecting from *Notch 1* the beam passes through the objective lens (*OL*) which focusses the laser onto the sample in the DAC. The objective lens is interchangeable for others with different magnification as might be required for different sample sizes. The objective lens then collimates the reflected light back along the x-direction where the Raman scattered light passes through *Notch 1* as described in the above paragraph. The objective lenses used in the contributing work necessarily had long working distances in order to focus on the

samples whilst allowing some space between the lens and the DAC during high-temperature experiments.

During the acquisition of spectra, the neutral-density filter (*ND*) and beam splitters (*BS1* and *BS2*) are removed from the beam path using flip-mounts (denoted by arrows). They are used when aligning the sample prior to the acquisition. The *ND* filter can be changed to allow a weak transmission of the laser light which can be observed along with the sample by focusing the front light source (from *LS1*) onto the sample which is reflected, along with the weak laser light, and then focused into the CCD of a camera connected to a monitor. Using this set-up is possible to select which area of the sample to probe, which is useful when the sample contains different regions. Transmitted light (from *LS2*) from visible or infra-red sources can also be used to obtain transmission spectra by removing the notch filters and adding mirror M_5 in the case of IR measurements.

The Raman scattered light then passes through the *spatial-filter*. The spatial-filter constrains the depth of the observed scattering in the sample by recollimating the signal after tightly focusing it through a pinhole. The spatial filter is a particularly important modification specifically for performing Raman spectroscopy with DACs because it reduces the observed noise from the fluorescence of the diamond anvils.

Finally, the beam passes through a second notch filter (*Notch 2*), which again decreases the Rayleigh scattering contribution to the signal. The signal is then focused into the spectrometer which diffracts the beam onto a CCD which outputs to a computer equipped with the WinSpec software which also controls the spectrometer. The spectrometer used in the contributing work was a Princeton Instruments Acton SpectraPro 2500i model equipped with changeable diffraction gratings of 300 and 1800 lines/mm. The CCD used for the Raman experiments was a Princeton Instruments model 7500-0003. The CCD used for infrared measurements was a Princeton Instruments NIRvana 640. The data were analysed using OriginLab and Fityk software packages.

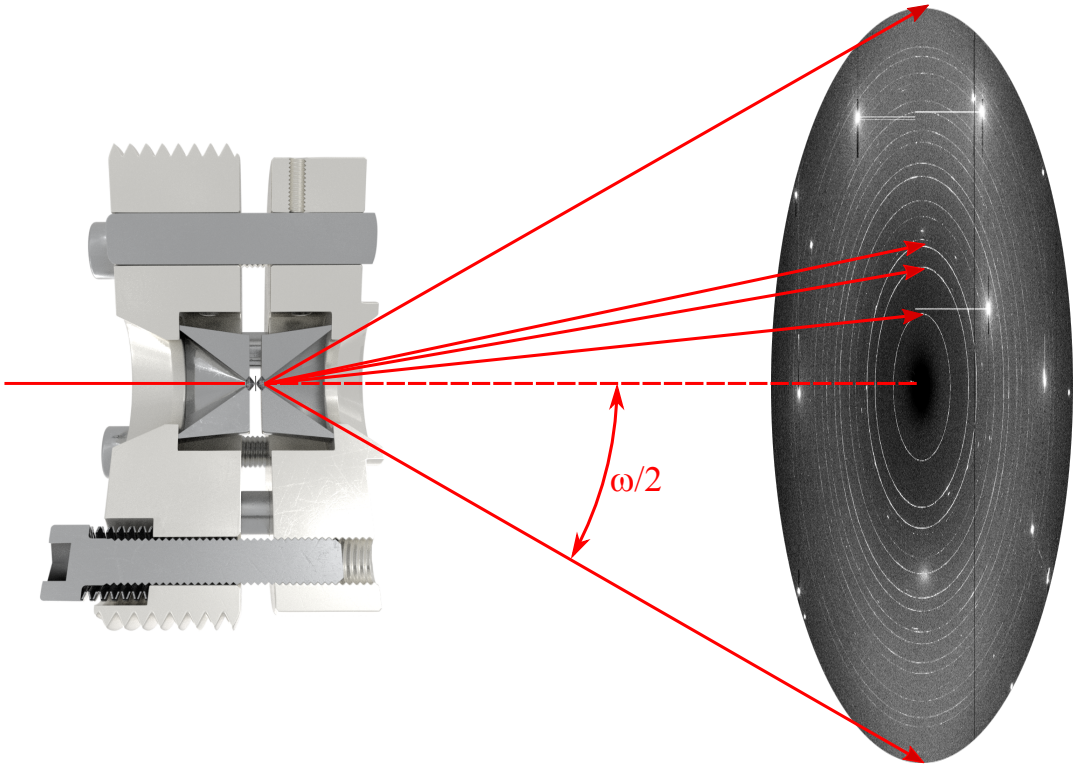

Figure 3.9: A schematic illustration of the diffraction geometry used in XRD experiments with DACs. The angle ω is limited by the cell geometry.

3.5 High Pressure X-ray Diffraction

Improvements in synchrotron technology are increasingly facilitating the use of X-ray diffraction (introduced in Section 2.2) on high-pressure samples in DACs. The tightly-focussed high-flux X-ray beams of synchrotrons are necessary for working with small samples in order to observe sufficient diffraction intensity from the sample whilst avoiding hitting the gasket material or DAC body. Several dedicated high-pressure beam lines were visited in the contributing work, including: ID09A (before it was moved to ID15B) at the ESRF, P02.2 at PETRA III, and I15 at Diamond.

Whilst each of the synchrotrons used in the contributing work operate slightly differently, the principle of operation is the same. Synchrotrons are particle accelerators which generate X-rays by accelerating a particle beam around a closed-loop using bending magnetic fields. The particles are accelerated in a linear

accelerator before being injected into the loop. The accelerating particles pass through an insertion device in which they are passed through an alternating magnetic field, stimulating the emission of synchrotron X-ray radiation. The X-ray radiation is then focused and collimated, and a single energy is selected using a monochromator. The X-ray beam is then injected into the instrumentation hutch where it passes through the sample and generates the diffraction pattern which is detected on a solid-angle area-detector.

3.5.1 Data Acquisition and Processing

The DAC is aligned in the instrumentation hutch before the data acquisition by mounting it on a goniometer and rotating it around the vertical axis so that the diamond culets are perpendicular to the axis of the X-ray beam. The DAC is then moved in the plane perpendicular to the beam so that the beam passes through the centre of the sample.

During the exposure, the DAC may be rotated about the vertical axis by angle ω which is limited by: the cell geometry, the diamond geometry and the seat apertures, as shown in Figure 3.9. Polycrystalline samples are rotated through ω during a single acquisition because the quality of the diffraction rings can be improved by passing more crystallites through the correct scattering conditions. Single crystal samples are rotated incrementally, with an exposure taken at each increment, so that a model of the reciprocal-lattice may be constructed by combining the individual shots of reciprocal space[‡].

The diffraction patterns are detected by a two-dimensional area detector which outputs raster image files of various formats. The images in the contributing work were processed with the Dioptas software package [Prescher 15] following the standard procedure which has three main stages: calibration, integration and

[‡]The single-crystal data presented in this thesis (Chapter 7) were analysed by collaborators Dr Jack Binns and Dr Michael Hanfland and were *not* analysed by the author.

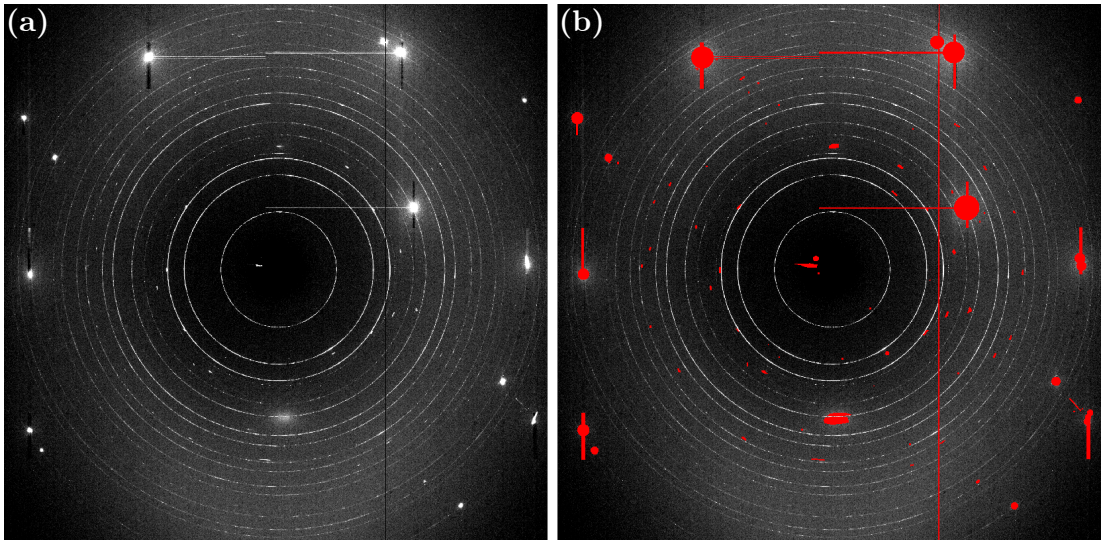

Figure 3.10: An example of a raw image plate. **(a)** The data are unmasked and diffraction spots from the diamond anvils are very clear. **(b)** The same image plate with masked regions shown in red.

masking.

The calibration stage defines the detector-DAC geometry so that the spatial relationship between the sample and the diffraction pattern is known and so that the reflections can be accurately indexed. The detector-DAC geometry is determined by acquiring a diffraction pattern from a calibration sample with known Bragg reflection positions, commonly CeO_2. A number of parameters must also be specified, such as: the X-ray wavelength, the detector pixel-size and the sample-detector distance. For each acquisition a 'dark image' may also be taken in which the X-ray beam is not incident on the sample. The dark image is subtracted from the diffraction image to remove any detector artefacts such as light spots from previous overexposed images.

One of the difficulties associated with processing diffraction data from DACs is contamination of the pattern with reflections from the diamond anvils, which are often very intense, despite the relatively low scattering intensity of carbon, because of the relative thickness of the diamonds compared to the samples (mm *vs.* μm). Diffraction artefacts not arising from the sample may be manually *masked*, thus excluding those areas from the integration. An example of masked

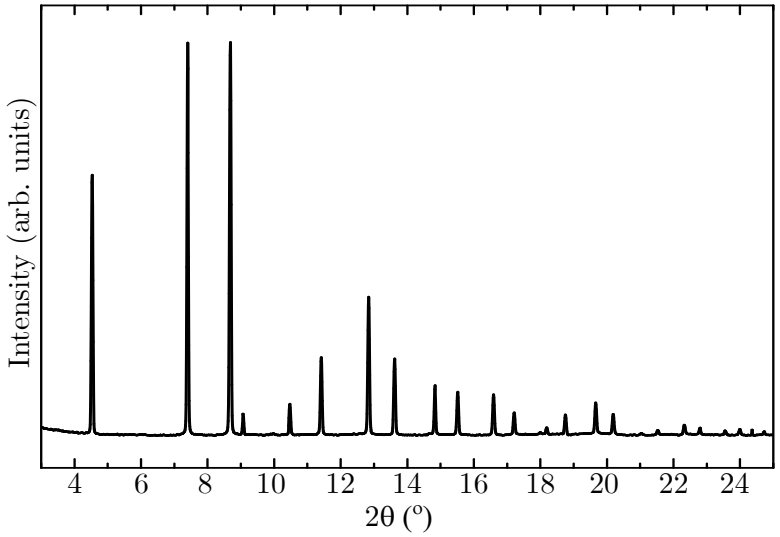

Figure 3.11: An example intensity *vs.* 2θ plot generated from the data in Figure 3.10. The data are from the contributing work into xenon-nitrogen mixtures which is discussed in detail in Chapter 5.

data (red areas) is shown in Figure 3.10.

After the calibration and masking stages the integration of the two-dimensional image is performed in which the sum of the detected intensity along the azimuthal lines (i.e. rings) is plotted as a one-dimensional function of the scattering angle 2θ. An example plot is given in Figure 3.11.

Chapter 4

Review of Nitrogen at Extreme Conditions

This chapter presents the reader with an overview of elemental nitrogen under extreme conditions. Nitrogen is central to each of the three following experimental chapters of this thesis, so it is appropriate to provide a review here to avoid repetition in subsequent chapters.

4.1 Introduction

The discovery of nitrogen is largely accredited to Daniel Rutherford who, at the University of Edinburgh in 1772, was the first to (rudimentarily) isolate nitrogen gas [Rutherford 72].

A neutral nitrogen atom has seven electrons, arranged in the electron configuration: $1s^2$, $2s^2$, $2p_x^1$, $2p_y^1$, $2p_z^1$. The three unpaired valence electrons in the p-orbitals make atomic nitrogen a triradical which is highly reactive and can form nitrides with many different elements. Elemental nitrogen exists as a homonuclear diatomic gas under ambient conditions. The N_2 molecule is a relatively

inert chemical species, unlike the highly reactive atomic nitrogen, because it possesses the only triple-bond of the elemental diatomics. The triple-bond has a large bond-dissociation energy[†] of 945.41 kJ mol^{-1} (9.79 eV/bond) and a short bond-length (1.0976 Å) [Greenwood 12].

Nitrogen is the lightest of the group 15 elements (pnictogens) and its valence orbitals ($2s$ and $2p$) have similar radii. As with most of the first-row p-block elements, the similar valence radii cause a large electrostatic attraction between the valence electrons and the atomic nuclei, resulting in nitrogen's characteristically large electronegativity. The electronegativity of nitrogen is sufficient to induce hydrogen-bonding in systems containing N-H bonds (such as ammonia), much like its neighbouring oxygen in the periodic table. Nitrogen is not able to form long chains of atoms under standard conditions, unlike its neighbouring carbon, or the close-by phosphorus and sulphur, both of which can exists as many allotropes under standard conditions.

The nitrogen molecule is used in extreme-conditions research as an archetypal diatomic molecule to explore high-pressure phenomena in both experimental and theoretical investigations. The pressure-temperature (P-T) phase diagram of nitrogen (shown in Figure 4.1) has been a focus-point in high pressure research for the past 20 years. Nitrogen exhibits exceptional polymorphism under extreme conditions compared to other archetypal diatomics, such as hydrogen or oxygen, and at least 15 unique solid nitrogen phases have been identified in the literature at the time of writing this thesis. The chronology of the discovery of nitrogen phases is presented in Table 4.1. Eight of the 15 known phases have been discovered since the turn of the millennium, with the earliest observations dating back over a century, demonstrating that the study of molecular systems under extreme conditions has undergone substantial developments in recent decades.

The nitrogen phases are appropriately categorised according to the bonding

[†]It is second amongst all diatomics to its isoelectric analogue carbon monoxide, CO, which has a bond-dissociation energy of 1074.83 kJ mol^{-1} (11.16 eV/bond) [Darwent 70].

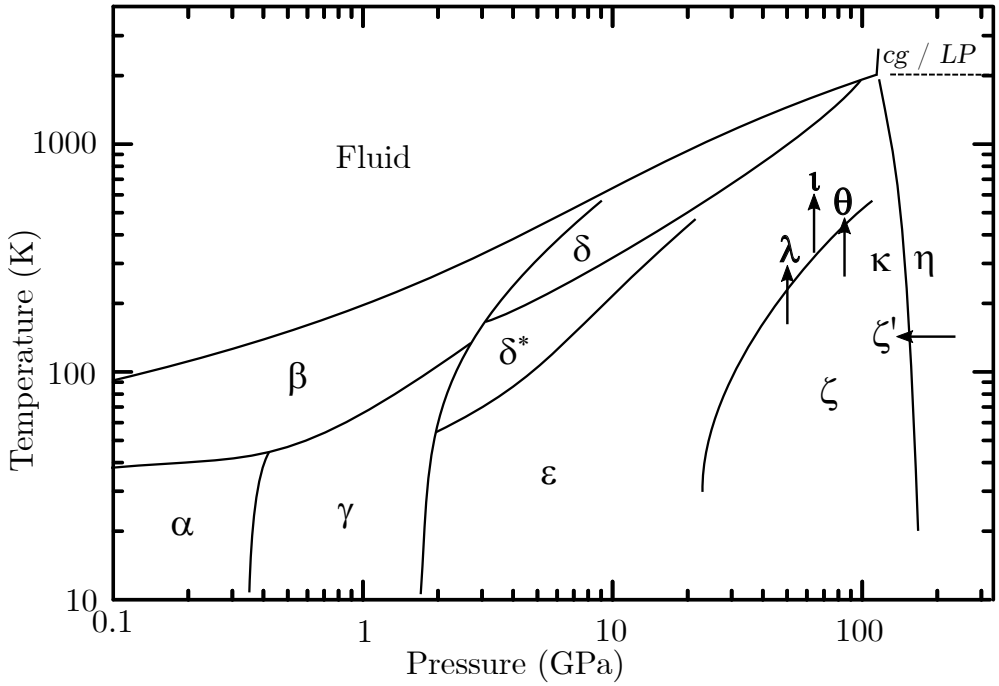

Figure 4.1: The temperature-pressure phase diagram of nitrogen showing all 15 known solid nitrogen phases. (The diagram is adapted from ref. [Gregoryanz 07].) The phases indicated with arrows require those specific P-T paths to be accessed and have stability regions which overlap large areas of the phase-diagram. The λ, ι and θ phases shown in bold are discussed in detail Chapter 7.

characteristics which define their structure. Each of the known phases is briefly discussed herein, and structural data for each phase have been collated into Table 4.2. Chapter 7 specifically focusses on the contributing work of this thesis relating to the ι-phase of nitrogen.

4.2 Molecular Phases: α, β, γ, δ, δ^*, ϵ, ζ, ζ', θ, ι, κ, and λ

The majority of the known nitrogen phases are 'molecular' in the sense that their structures comprise N_2 molecules between which there is no electron transfer.

The first samples of solid nitrogen were prepared at atmospheric pressure in early cryogenic experiments of the 20th century. The boiling point of molecular nitrogen at atmospheric pressure is 77 K. The freezing point is 63 K, below which

Phase	Year	Article
α	1916	[Eucken 16]
β		
γ	1955	[Swenson 55]
δ	1981	[Cromer 81]
ϵ	1985	[Schiferl 85]
ζ		
δ^*	1993	[Scheerboom 93]
η	2000	[Goncharov 00]
ζ'	2001	[Gregoryanz 01]
θ	2002	[Gregoryanz 02]
ι		
cg	2004	[Eremets 04b]
κ	2007	[Gregoryanz 07]
LP	2014	[Tomasino 14b]
λ	2016	[Frost 16]

Table 4.1: A chronology of the discovery of nitrogen phases. Although nitrogen was first solidified in the 1880s [Olszewski 84] the discovery of the α and β-phases has here been accredited to Eucken *et al.* [Eucken 16] who, in 1916, correctly attributed a discontinuity in the low-temperature heat-capacity to a phase-transition which was later shown to be the $\beta \leftrightarrow \alpha$ transition.

Phase	Space Group	a (Å)	b (Å)	c (Å)	β (°)	V (Å^3)	P (GPa)	Article
α	$Pa\bar{3}$	5.433	-	-	-	160.4	0.38	[Schuch 70]
β	$P6_3/mmc$	3.595	-	5.845	-	65.4	2.94	[Schiferl 83]
γ	$P4_2/mnm$	3.957	-	5.109	-	80.0	0.42	[Schuch 70]
δ	$Pm\bar{3}n$	5.881	-	-	-	203.4	9.5	[Hanfland 98]
ϵ	$R\bar{3}c$	5.928	-	-	85.14	207.6	7.8	[Mills 86]
ζ	Orthorhombic	6.533	2.574	6.844	-	115.1	90	[Gregoryanz 07]
δ^*	$P4_2/ncm$	8.603	-	5.685	-	420.8	14.5	[Stinton 09]
η	Amorphous	-	-	-	-	-	-	[Gregoryanz 01]
ζ'	**?**	**?**	**?**	**?**	**?**	**?**	-	-
θ	Orthorhombic	6.797	7.756	3.761	-	198.3	95	[Gregoryanz 02]
ι	$P2_1/c$	9.909	8.832	8.736	92.1	764.0	56	Chapter 7
cg	$I2_13$	3.454	-	-	-	41.2	115	[Eremets 04b]
κ	Monoclinic	6.918	6.202	2.289	91.8	98.2	130	[Gregoryanz 07]
LP	$Pba2$	4.160	4.248	4.369	-	77.2	112	[Tomasino 14b]
λ	$P2_1/c$	3.051	3.066	5.705	131.7	39.8	40	[Frost 16]

Table 4.2: Structural information for the nitrogen phases. Lattice parameters were all determined at room temperature, except for α, γ and ϵ-nitrogen which were determined at 19.6, 20.5 and 110 K respectively. Only β, δ, δ^* and ι-nitrogen have been studied via single-crystal XRD. Prior to this thesis there were no published structural data for the ι-nitrogen phase (see Chapter 7). The ζ'-phase has not been probed by XRD and its structure is completely unknown.

nitrogen crystallises into the β-phase, which is characterised by rotationally disordered molecules centred on a hexagonal close packed (hcp) [Schiferl 83, Schuch 70]. The rotational disorder is suppressed on reducing the temperature below 35 K where nitrogen transitions to the α-phase. The α-phase is characterised by ordered molecules centred on a face centred cubic (fcc) lattice [Schiferl 83].

The development of compressibility apparatus in the 1950s [Stewart 55] brought with it the discovery of the first high-pressure phase of nitrogen, the γ-phase [Swenson 55]. α-nitrogen transitions to the ordered tetragonal γ-phase when compressed to 0.4 GPa [Schuch 70]. The complete low-pressure rotational-ordering in the α and γ-phases is lost on isobaric heating as both phases enter β-phase [Schuch 70].

The room-temperature isothermal-compression-line of nitrogen is the most comprehensively explored P-T region of the phase-diagram. It is characterised by a series of seven phases-transitions which are as follows: fluid $\xrightarrow{2.4\text{ GPa}}$ β $\xrightarrow{4.9\text{ GPa}}$ δ $\xrightarrow{10.5\text{ GPa}}$ δ^* $\xrightarrow{16.3\text{ GPa}}$ ϵ $\xrightarrow{62\text{ GPa}}$ ζ $\xrightarrow{110\text{ GPa}}$ κ $\xrightarrow{150\text{ GPa}}$ η-phase.

The δ and δ^* phases exhibit a degree of rotational order-disorder in which some molecules preferentially align along specific directions [Stinton 09]. The rhombohedral ϵ-nitrogen [Mills 86, Olijnyk 90] structure was determined from powder XRD data and is probably completely rotationally ordered at higher pressures, although (as discussed in the introduction to Raman spectroscopy in section 2.1.4) the Raman spectra show signs of subtle changes in molecular ordering with pressure. ϵ-nitrogen transforms to ζ-nitrogen on compression to 62 GPa, which then transforms to κ-nitrogen on further compression at 110 GPa [Gregoryanz 07]. The structures of the ζ and κ-phases remain undetermined and the data presented in Table 4.2 are the most probable based on the current literature. Spectroscopic studies suggest that the ζ and κ-phases are molecular based on the absence of vibrational modes other than those originating from the N≡N molecule. Decompression of the non-molecular η-phase to below 87 GPa results in back-transformation to the little studied ζ'-phase which is also probably

molecular based on spectroscopy measurements [Gregoryanz 01].

The final three molecular phases to introduce are the θ, ι and λ-phases which are displayed in bold in the phase-diagram in Figure 4.1. The formation of the θ, ι and λ-phases is strongly P-T path-dependent and successfully reproducing their synthesis conditions appears to be experimentally challenging. Their formation conditions lie off the room-temperature isothermal-compression line. The θ and ι-nitrogen phases require elevated temperatures to be accessed, whereas λ-nitrogen, which shares very similar and complex Raman spectra with θ-nitrogen, has only been synthesised at low-temperatures:

θ-nitrogen can be accessed by heating ϵ-nitrogen to 600 K at 95 GPa [Gregoryanz 02]; by heating λ-nitrogen to 800 K at 70 GPa [Frost 16], or; by isothermal compression of ϵ-nitrogen to 97 GPa at 920 K [Tomasino 14a].

ι-nitrogen can be formed by heating ϵ-nitrogen to 750 K at 65 GPa [Gregoryanz 02]; by isothermal decompression of θ-nitrogen to 69 GPa at 850 K [Gregoryanz 02], or; by quenching the melt between 48 and 114 GPa [Goncharov 08], although it is not clear at what P-T conditions the onset of ι-nitrogen occurs in ref. [Goncharov 08] because no data specific to ι-nitrogen are presented.

λ-nitrogen has only been accessed through cryogenic compression at 77 K, from atmospheric pressure to at least 31 GPa, followed by isobaric heating to room temperature [Frost 16].

Once formed each of the θ, ι and λ-phases can be recovered to ambient-temperature and each of them back-transforms to directly ϵ-nitrogen on decompression between 23 and 32 GPa. Subsequent compression is not sufficient to reverse the transition. The P-T stability regions of these phases overlap with those of several other molecular phases, indicating that their structures may be amongst the most kinetically or thermodynamically stable [Frost 16]. Chapter 7 contains further discussion of the ι, θ and λ-nitrogen phases introduced here.

4.3 Non-molecular Phases: η, cg, and LP

Non-molecular phases of nitrogen have received considerable attention over the past 20 years. The significant difference in bond-dissociation-energy between the nitrogen triple and single-bonds make single-bonded nitrogen a theoretically perfect high energy density material (HEDM) because it would have a maximal chemical energy density whilst producing only inert nitrogen as a reaction product [Eremets 04b].

The nitrogen triple bond was predicted to dissociate at pressures readily achievable in DACs over 30 years ago [Barbee 93, Mailhiot 92, McMahan 85]. Above 150 GPa at room temperature a pressure-induced destabilisation of the nitrogen triple-bond results in the transition to the semiconducting η-phase which has been observed up to at least 268 GPa without further transitions [Eremets 01, Goncharov 00, Gregoryanz 01]. η-nitrogen is probably amorphous based on the absence of diffraction lines in XRD experiments, and it may contain clusters of non-molecular nitrogen [Eremets 04b]. The amorphous state is thought to be a precursor to an atomic state [Gregoryanz 01].

Introducing heat to sufficiently high-pressure nitrogen samples can overcome the transition barrier to atomic phases. Heating nitrogen to 2000 K at 110 GPa produces a single-bonded cubic network of sp^3-hybridised nitrogen atoms known as the "cubic-gauche" (or cg) phase [Eremets 04b]. Heating to over 2000 K above 126 GPa results in a mixture of cg and a layered polymeric phase (known as LP) [Tomasino 14b] which also exhibits sp-hybridisation and an extended structure, thus defining a very distinct family of polymeric nitrogen phases. The cg and LP phases are recoverable to around 50 GPa at room temperature, displaying quite large areas of stability.

The high-pressure region of the P-T phase-diagram of nitrogen has been largely mapped using spectroscopic techniques to distinguish between different phases. Consequently, and with the exception of the atomic phases, the struc-

tures of the high-pressure nitrogen phases remain largely undetermined. A number of phases are experimentally accessible which are stable over very similar P-T conditions and it may only be possible to explain why once those structures have been determined. The phase-diagram is further complicated by the P-T path dependence of the observed phase-transitions. Simply being at the correct P-T conditions is not necessarily the only requisite for entering the phase of interest. The path followed to those P-T conditions, and the length of time for which those P-T conditions are held, may be important factors when working with nitrogen at extreme conditions. To illustrate with an example, the $\lambda \rightarrow \theta$ transition at 800 K at 70 GPa [Frost 16], and the $\epsilon \rightarrow \iota$ transition at 750 K and 65 GPa [Gregoryanz 02], occur at very similar conditions yet yield different structures due to the different initial phase.

The need for high-quality structural data of the high-pressure nitrogen phases is a contemporary issue in high-pressure physics which is being facilitated by developments in dedicated high-pressure beamlines at synchrotrons introduced in section 3.5. Chapter 7 presents a structural study of the ι-phase of nitrogen, the structure of which was unknown prior to the contributing work. The following chapter presents the first comprehensive experimental study of the nitrogen–xenon system at high pressures.

Chapter 5

Nitrogen-Xenon

5.1 Introduction

Mixtures of elemental gasses under pressure have attracted much attention in extreme-conditions research since the discovery of solid van der Waals compounds in the high-pressure helium-nitrogen system [Vos 92]. Each binary mixture of the four lightest elemental gasses: H_2, He, N_2 and O_2 has been studied experimentally at high-pressure, as well as almost all binary combinations of these with the noble gasses, as shown in table 5.1.

	H_2	**He**	**N_2**	**O_2**
H_2				
He	[Loubeyre 92]			
N_2	[Spaulding 14]	[Vos 92]		
O_2	[Loubeyre 95]	[Weck 10]	[Sihachakr 04]	
Ne	[Loubeyre 92]	[Loubeyre 93]	[Plisson 14]	[Weck 10]
Ar	[Loubeyre 92]	—	[Klee 91]	[Weck 10]
Kr	[Kleppe 14]	—	—	—
Xe	[Somayazulu 10]	[Barrat 92]	[Howie 16a]	[Dewaele 16]
D_2	[Howie 14]	[Loubeyre 96]	[Kim 11]	—

Table 5.1: Table displaying the binary-mixtures of elemental-gases which have been studied under high-pressures. N.B.: Table 5.1 is only meant to illustrate the extent to which elemental mixtures have been studied at high-pressures and is not meant to be exhaustive resource.

Nitrogen and its phase-diagram are discussed in Chapter 4 and the reader is referred there for an in-depth review of nitrogen at extreme conditions to avoid repetition here. In the context of this chapter it is interesting to note that nitrogen becomes non-molecular and semi-conducting at 240 GPa [Eremets 01, Gregoryanz 01].

Xenon is the heaviest of the (non-radioactive) noble gases. Like nitrogen it is colourless and odourless at ambient conditions. It is also chemically inert due to its closed-shell electron configuration ([Kr] $4d^{10}$ $5s^2$ $5p^6$). It was first predicted to form stable compounds with fluorine and oxygen by Linus Pauling in 1933 [Pauling 33] and one of the first experimentally demonstrated compounds was discovered about 30 years later with the covalently bonded xenon tetrafluoride, XeF_4 [Claassen 62].

Xenon solidifies into an fcc solid at around 2 GPa under room-temperature compression. It undergoes a gradual transition from fcc to hcp between 14 and 75 GPa [Jephcoat 87]. The fcc to hcp transition can be completed at lower pressures through the addition of heat [Caldwell 97]. Xenon has been shown to become metallic upon further compression to between 130-150 GPa at room-temperature, as confirmed through direct measurement of electrical transport properties [Eremets 00] and suggested through earlier optical measurements [Goettel 89, Reichlin 89].

The chemical reactivity of xenon increases with high-pressure high-temperature conditions. Xenon-containing van der Waals compounds have been discovered at high-pressures, such as $Xe(H_2)_7$ around 5 GPa [Somayazulu 10] and $Xe(O_2)_2$ around 3 GPa [Weck 10]. Xenon has even been shown to enter a non-zero oxidation state in the Xe-O_2 system when laser heated [Dewaele 16]. Doping the high-pressure xenon system with small amounts of oxygen (0.6 mol.% O_2) has been shown to drastically reduce the metallization pressure of xenon from 130 to 49 GPa [Dewaele 12].

Prior to the work of this chapter the experimental studies on the nitrogen–xenon system presented no structural data and were limited to pressures up to 13 GPa and temperatures of only 408 K [Kooi 99b, Kooi 99a]. The Raman spectra of these studies hinted towards the plausibility of orientationally disordered xenon-nitrogen van der Waals compounds based on Raman spectroscopy, although the lack of structural investigation prevented definitive conclusions. Nitrogen–xenon compounds had previously been predicted to form above 146 GPa [Peng 15] in which xenon atoms are coordinated by non-molecular nitrogen. The incomplete experimental ground-work on the high-pressure xenon-nitrogen system showed the possibility of interesting physics which motivated the investigation of this chapter.

5.2 Methods

Raman spectroscopy was conducted using both 514 and 647 nm excitation wavelengths as described in section 3.4 and pressure was monitored using the ruby fluorescence and diamond-edge scales described in section 3.1.1. BA diamonds with 200 μm culets were used in experiments up to 50 GPa in symmetric-type DACs with wide-opening seats to allow detection of wider scattering-angles in XRD experiments. 60 μm culets were used in piston-cylinder type DACs up to 180 GPa and for the optical measurements.

Sample-loading — The xenon-nitrogen mixtures were loaded into DACs using a two-stage process developed specifically for this project. The loading procedure involved initially cryo-loading pure xenon solid, followed secondly by secondly gas-loading nitrogen. The loading process is discussed in detail in the DAC loading methods section 3.2.3.

X-ray Diffraction — X-ray diffraction data were acquired at PETRA-III at the P02.2 Extreme Conditions Beamline. Patterns were generated using a monochromatic beam of wavelength $\lambda = 0.4872$ Å. The patterns were recorded on a

PerkinElmer XRD 1621 detector. Data were also acquired at ID09 at the ESRF with a monochromatic beam of wavelength $\lambda = 0.4139$ Å. Data were recorded on a MAR555 flat panel detector. Intensity *vs.* 2θ plots were obtained by integrating the image plate data in DIOPTAS [Prescher 15]. Indexing was carried out in GSAS-II [Toby 13]. Le Bail and Rietveld refinements were carried out in Jana2006 [Petricek 14].†

5.3 Results

Opening summary — The results in this section are presented stepwise according to the sample compression-path, from loading at 0.2 GPa to the maximum pressure of 180 GPa. For clarity, the results are summarised concisely in this paragraph. For the sake of discussion it will be useful for the reader to bear in mind the micrograph shown in Figure 5.1. The sample-regions marked 'A' and 'B' in Figure 5.1 both contain a new van der Waals compound, $Xe(N_2)_2$. In sample-region 'A' the $Xe(N_2)_2$ is embedded in an excess of xenon atoms. In sample-region 'B' the $Xe(N_2)_2$ is embedded in an excess of nitrogen molecules. In both sample-regions $Xe(N_2)_2$ adopted a cubic structure below 14 GPa, herein referred to as $Xe(N_2)_2$-I. In both sample-regions $Xe(N_2)_2$ adopted a body-centred tetragonal structure above 14 GPa, herein referred to as $Xe(N_2)_2$-II.

Due to the nature of the loading technique it was not possible to accurately control the relative molar ratio of xenon and nitrogen upon loading the sample. Some samples were prepared which consisted almost entirely of one or the other xenon or nitrogen-rich regions, however it was actually beneficial to have both regions at the same pressure in the same DAC and some of the highest-quality XRD data was obtained from samples such as the one shown in Figure 5.1.

Below 5 GPa: the fluid state — All of the xenon-nitrogen mixtures studied

†As per the declaration at the beginning of this thesis, a significant contribution to all of the work was made by the author, however it should be noted that the x-ray diffraction analysis in this chapter was performed by Dr Jack Binns.

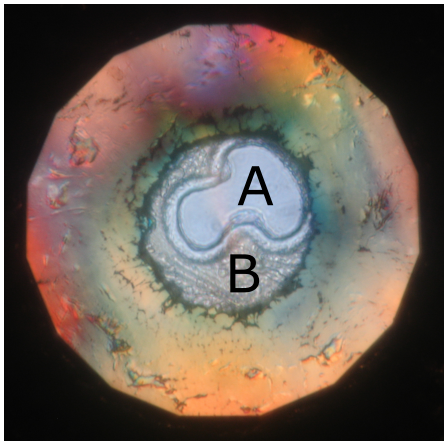

Figure 5.1: Micrograph of a xenon-nitrogen sample at 5.3 GPa containing both (A) xenon-rich and **(B)** nitrogen-rich regions. Both sample-regions contain $Xe(N_2)_2$-I or $Xe(N_2)_2$-II depending on the pressure.

in the contributing work formed homogeneous fluids upon loading at 0.2 GPa. Raman spectra from the fluid phase appeared no different from those of pure nitrogen. Upon room-temperature compression to 1.8 GPa the homogeneous fluids spontaneously phase-separated into xenon-rich and nitrogen-rich fluids as shown in Figure 5.2a. Nitrogen has a solubility in solid xenon of about 7.5% mol [Kooi 99a] and nitrogen Raman vibrational modes were observed in both sample-regions (discussed below). The difference in nitrogen concentration was observed by the difference in the intensity of the nitrogen Raman vibrational mode. When the sample pressure was held constant in the phase-separated fluid state, the xenon-rich and nitrogen-rich fluids spontaneously coagulated over periods of 24-48 hours.

On further compression, the central xenon-rich fluid 'bubble', shown in Figure 5.2b, solidified into a single-crystal with a structure corresponding to the known fcc xenon structure at 3 GPa, as confirmed though XRD. At the same pressure, the surrounding nitrogen-rich medium remained a fluid containing crystallites of the known xenon fcc structure as determined by XRD (shown in Figure 5.3a). This process was successfully repeated with approximately ten different samples.

Between 5 and 14 GPa: $Xe(N_2)_2$-I — Upon compression to 5 GPa the surrounding nitrogen-rich fluid solidified into a highly polycrystalline powder. An

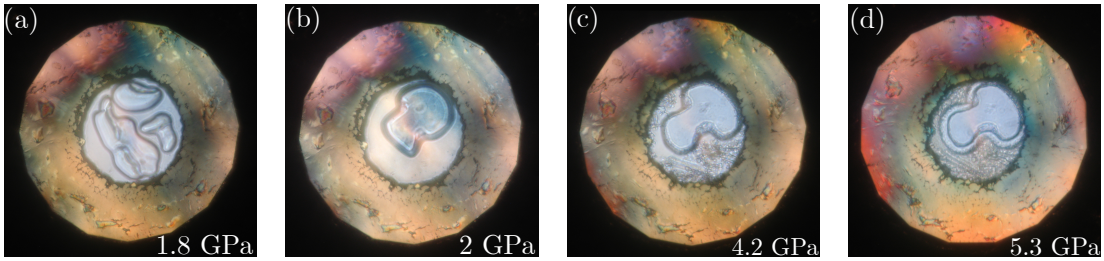

Figure 5.2: Micrographs of a xenon-nitrogen sample on room-temperature compression over 24 hours. **(a)** Fluid phase-separation into xenon-rich and nitrogen-rich fluids. **(b)** Spontaneous coagulation of xenon-rich fluid (centre) over 24 hours. **(c)** Solidification of the central xenon-rich sample-region surrounded by fluid nitrogen containing xenon crystallites. **(d)** Solidification of both xenon-rich and nitrogen-rich regions at 5.3 GPa.

X-ray diffraction pattern from the polycrystalline region is shown in Figure 5.3b. The highly polycrystalline solid is visible in Figure 5.2d as the grainy surrounding medium. Through X-ray powder diffraction analysis the new solid was observed to have a cubic structure with $a = 9.2361(3)$ Å at 5.6 GPa, making it too large to be pure xenon and different from any known nitrogen phase. (The Raman spectra also showed activity which could not arise from pure xenon - discussed below.) All observed Bragg peaks were accounted for by indexing with space-group $Fd\bar{3}m$ (see Figure 5.4a). Rietveld refinement was possible with several patterns, and two atomic sites were refined; Xe(0, 0, 0) and N $\left(\frac{5}{8}, \frac{1}{8}, \frac{1}{8}\right)$ resulting in a cubic Laves-type structure. The $Xe(N_2)_2$-I structure can be thought of as a xenon host-lattice in the diamond-structure with a tetrahedron of rotationally disordered N_2 molecules occupying each vacancy, as shown in Figure 5.5. The $Xe(N_2)_2$-I solid shares its structure-type (and stoichiometry) with previously discovered noble gas van der Waals compunds: $Xe(O_2)_2$ [Weck 10], $Ne(He_2)$ [Loubeyre 93] and $Ar(H_2)_2$ [Loubeyre 94]. The freely rotating N_2 molecules were modelled in the refinement as normal atomic positions with the site occupancy fixed equal to two. The thermal displacement parameter of the doubly occupied site, which was allowed to refine, increased during the refinement, effectively distributing the electron density over a larger spherical volume and therefore approximating the time averaged charge distribution of a tumbling N_2 molecule. The shortest N...N inter-atomic distance is 2.1655(1) Å at 5.6 GPa. Additional crystal structure and

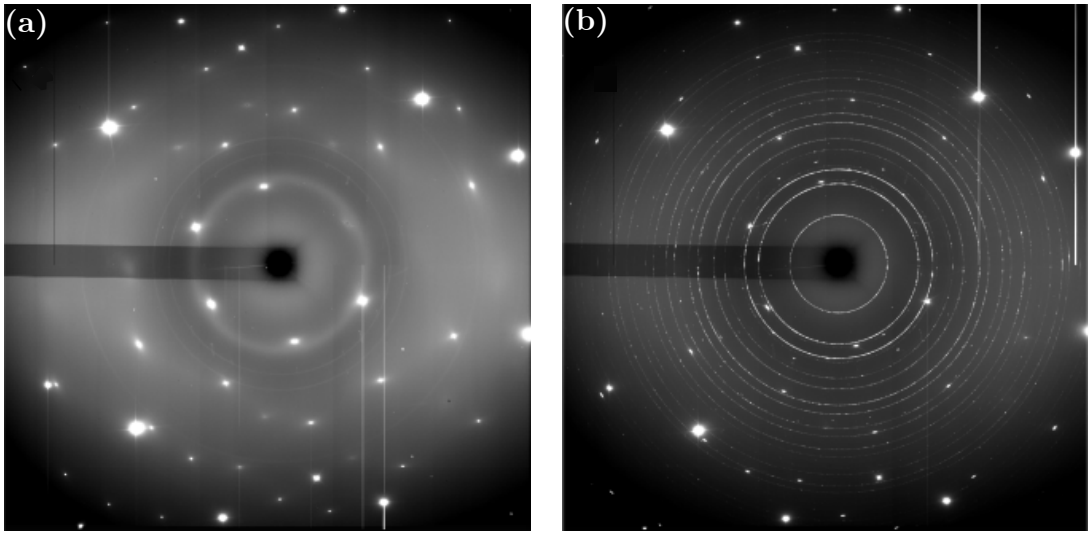

Figure 5.3: X-ray diffraction patterns from of the same nitrogen-rich sample region on compression. (a) A diffraction pattern acquired at 3 GPa. The known xenon fcc phase is shown in addition to the first diffraction peak from liquid nitrogen. **(b)** A diffraction pattern acquired at 5.6 GPa. The polycrystalline $Xe(N_2)_2$ provided high-quality powder data. Very intense peaks are due to scattering from the diamond anvils.

refinement information can be found in Appendix A.

Raman spectroscopy measurements at 5 GPa are shown in Figure 5.8. The xenon-rich crystal (marked 'A' in the inset) exhibited a low intensity vibrational mode which was down-shifted in frequency by about 10 cm^{-1} compared to pure nitrogen at the same pressure. Raman spectra from the polycrystalline nitrogen-rich region (marked 'B' in the inset) exhibited a broadened nitrogen vibron due to the overlap of nitrogen vibrons from both the $Xe(N_2)_2$-I solid and pure nitrogen. Spectra from a sample of pure nitrogen are included in black for comparison.

Above 14 GPa: $Xe(N_2)_2$-II — Increasing pressure further to 14 GPa, the $Xe(N_2)_2$-I structure transitioned to a body-centred tetragonal $I4_1/amd$ structure, $Xe(N_2)_2$-II, with unit cell dimensions of $a = 5.7228(3)$, $c = 9.2134(10)$ Å at 18.7 GPa. The $I4_1/amd$ space group was identified through systematic absence analysis. Two atomic sites were refined via Rietveld refinement: Xe(0, 0, 0) and N(0.5, 0.721(2), 0.179(1)). The N position is displaced from an inversion centre by

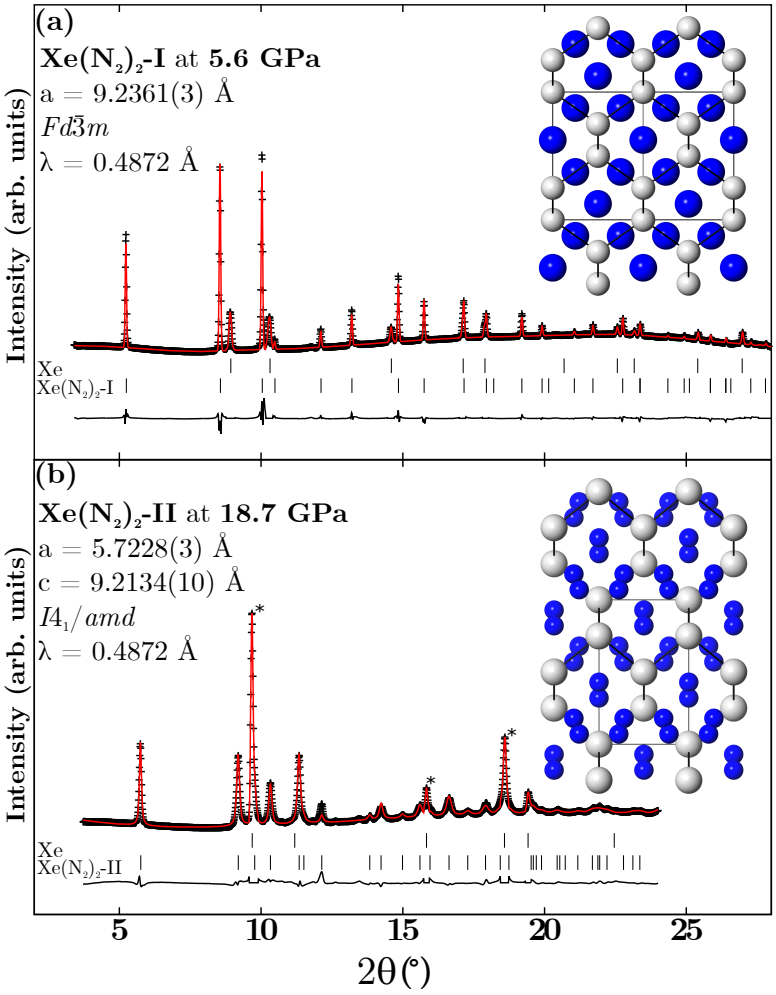

Figure 5.4: Integrated polycrystalline X-ray diffraction patterns at 5.6 and 18.7 GPa. (a) $Xe(N_2)_2$-I at 5.6 GPa. **(b)** $Xe(N_2)_2$-II at 18.7 GPa. Peaks marked with asterisks are from xenon. Insets show the respective crystal structures. The relationship between the two is shown in Figure 5.6. The blue spheres in the $Xe(N_2)_2$-I structure represent freely rotating N_2 molecules, whilst in $Xe(N_2)_2$-II the blue spheres represent individual nitrogen atoms. (The Author would like to acknowledge and thank Dr Jack Binns for producing this Figure.)

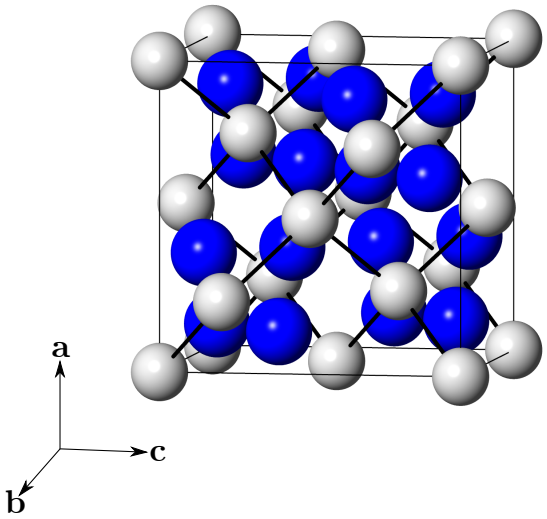

Figure 5.5: The cubic $Fd\bar{3}m$ crystal structure of $Xe(N_2)_2$-I. Xenon atoms are shown in grey. Freely rotating N_2 molecules are represented by blue spheres.

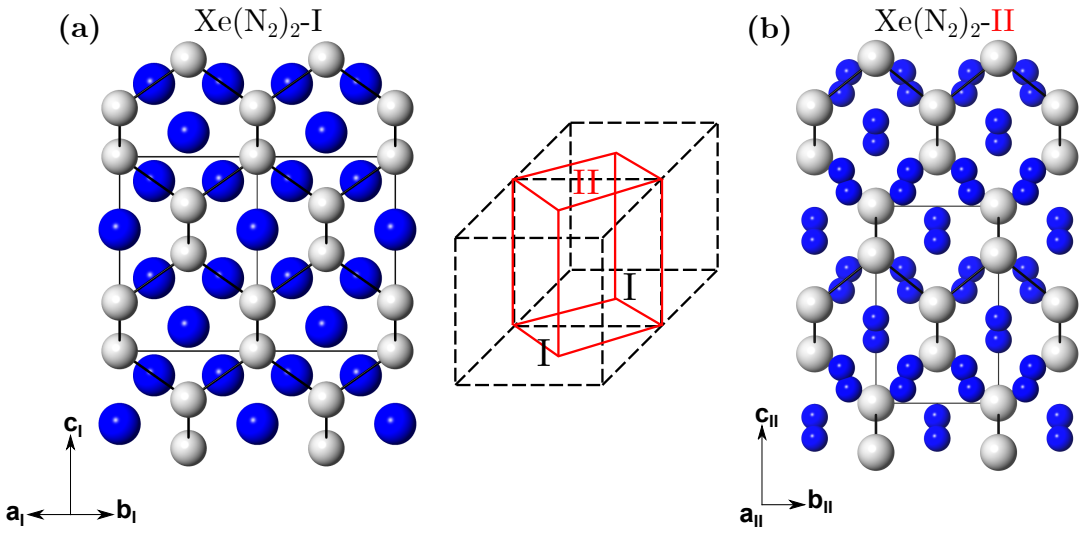

Figure 5.6: The crystal structures of (a) $Xe(N_2)_2$-I and (b) $Xe(N_2)_2$-II. The diagram in the centre of the figure illustrates the geometrical relationship between the two structures. **(a)** The $Xe(N_2)_2$-I structure as viewed along the cubic face diagonal. In **(a)** the blue spheres represent tumbling N_2 molecules. **(b)** The $Xe(N_2)_2$-II structure as viewed along the tetragonal a-axis. In **(b)** the blue spheres represent nitrogen atoms.

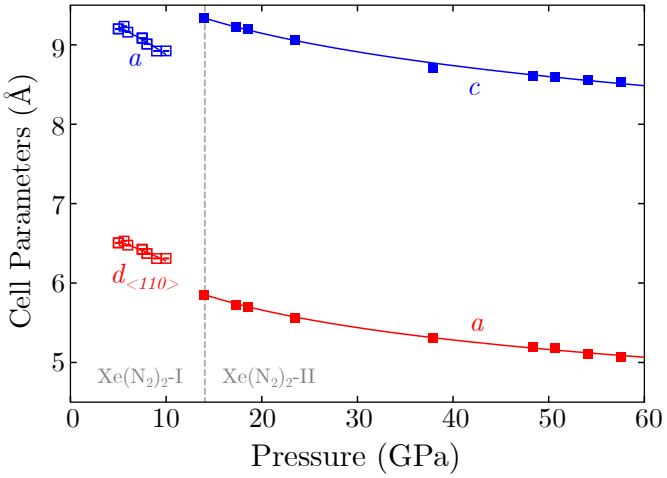

Figure 5.7: Response of cell parameters to applied pressure for $Xe(N_2)_2$. $Xe(N_2)_2$-I data are shown for the unit-cell length a (open blue squares) and $d_{<110>}$ (open red squares). $Xe(N_2)_2$-II data are plotted for unit-cell lengths c (closed blue squares) and a (closed red squares).

0.52(2) Å resulting in four N_2 molecules aligned along the c-axis. The defining characteristic of the phase transition is that the nitrogen molecules, which are rotationally disordered in $Xe(N_2)_2$-I, become ordered upon entering the $Xe(N_2)_2$-II phase. The two $Xe(N_2)_2$ structures are illustrated in figure 5.6. The ordering is supported by the poorer fit to the data ($R = 0.1672$ *vs.* $R = 0.094$) when using the aforementioned spherical N_2 model. In $Xe(N_2)_2$-II the shortest N...N interatomic distance is 2.5238(1) Å at 18.7 GPa, which is about 0.5 Å larger than in the lower pressure $Xe(N_2)_2$-I. Therefore, the alignment of the N_2 molecules relieves unfavourable close N...N contacts whilst maintaining the same N_2 coordination number.

The unit cell dimensions of $Xe(N_2)_2$-II were monitored up to 58 GPa (see Figure 5.7). Upon the phase transition, the cell elongates by 0.323(3) Å (an increase of 3.6%) along the c-axis, and contracts by - 0.519(1) Å (a decrease of 8.1%) along the tetragonal a-axis. The known fcc $\rightarrow$ hcp transition in pure xenon was observed from 38 GPa upwards. The appearance of strong xenon reflections which overlapped with those of $Xe(N_2)_2$-II prevented reliable determination of the unit cell dimensions above 58 GPa.

The $Xe(N_2)_2$-I $\rightarrow$ $Xe(N_2)_2$-II transition could not be clearly identified from the Raman spectra (see Figure 5.8), probably because the transition is characterised primarily by a loss of rotational disorder without any change in the co-ordination of the nitrogen molecules. The transition pressure of 14 GPa is similar to that of the room temperature transition $\delta^* \rightarrow \epsilon$-nitrogen at 16.3 GPa which is also partly characterised by a loss of rotational freedom. Presumably the inequivalent nitrogen sites in $Xe(N_2)_2$-II exhibited different but very similar vibrational frequencies in the Raman spectra which were too close to distinguish at the onset of the phase-transition. On increasing pressure to 20 GPa a shoulder on the nitrogen vibrational mode became observable, however it was no longer distinguishable by around 60 GPa due to broadening and weakening of the vibrational bands.

No further phase-transitions were observed on compression to the maximum pressure of 180 GPa, and the nitrogen remained molecular. The frequency of the $Xe(N_2)_2$ mode exhibited the same pressure dependence in both nitrogen-rich and xenon-rich environments, albeit with a constant frequency offset of $\sim$ 20 cm^{-1} (shown in Figure 5.8b). The $Xe(N_2)_2$ vibrational mode exhibited a maximum at around 30 GPa, which is approximately 50 GPa lower than the frequency maximum exhibited by nitrogen. The identical pressure dependence suggested that the vibron from the xenon-rich solid was due to small crystallites of the $Xe(N_2)_2$ phases which had formed in the xenon crystal, however it was impossible to identify $Xe(N_2)_2$ in the diffraction patterns from the xenon-rich regions, probably due to a low concentration relative to pure xenon.

Optical measurements — The optical properties of $Xe(N_2)_2$-II in nitrogen and in xenon were investigated by transmission spectroscopy in the visible range using a black-body-spectrum halogen light source (between 400-1000 nm), and in the near infra-red range a supercontinuum laser (between 1000-1800 nm). Following standard procedure, two spectra were acquired at each pressure-step: a 'light' spectrum in which the light-source was focussed into the sample, and a 'dark' spectrum in which the light-source was blocked from the sample. The 'dark' spectra were subtracted from the corresponding 'light' spectra to remove signal

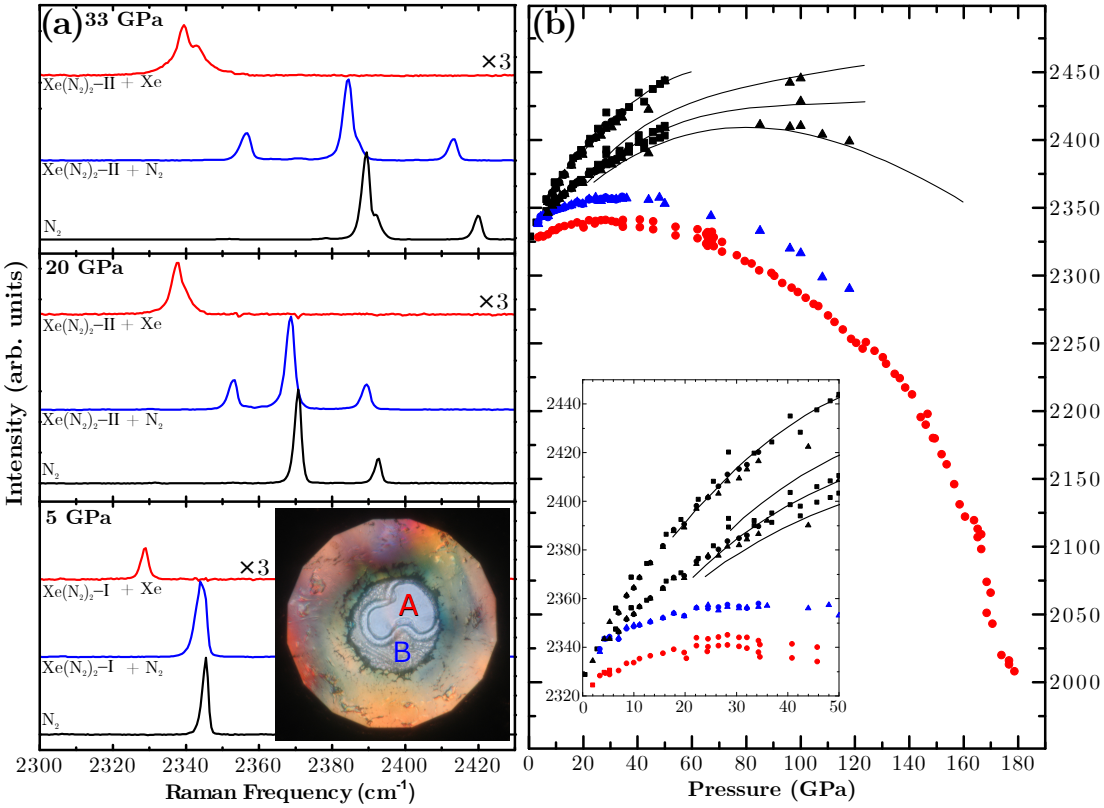

Figure 5.8: Raman spectroscopy data acquired from $Xe(N_2)_2$ in both xenon-rich and nitrogen-rich sample regions. Red spectra are from $Xe(N_2)_2$ embedded in xenon - acquired from the sample-region marked "A" in the inset. Blue spectra are from $Xe(N_2)_2$ embedded in nitrogen - acquired from the sample-region marked "B" in the inset. Vibrational spectra of pure N_2 are shown in black for comparison. **(a)** Raman spectra of $Xe(N_2)_2$-I at 5 GPa and of $Xe(N_2)_2$-II at 20 and 33 GPa. **Inset**: Photo of the sample at 5 GPa. **(b)** Raman Frequency plotted against pressure up to the maximum pressure studied of 180 GPa. **Inset**: An enlarged view of the data below 50 GPa.

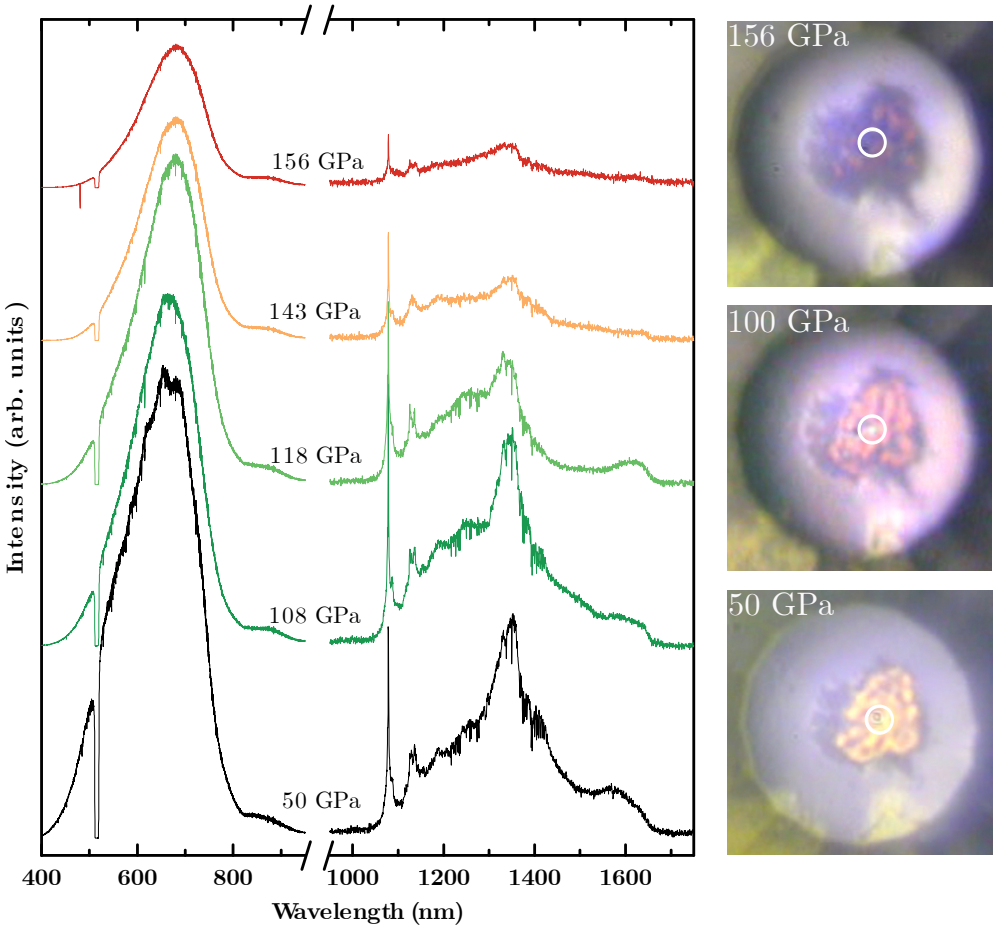

Figure 5.9: Transmission spectra and corresponding micrographs of $Xe(N_2)_2$-II embedded in nitrogen up to 156 GPa. Left: Transmission spectra in the visible and mid infra-red regions of $Xe(N_2)_2$-II embedded in nitrogen up to 156 GPa. **Right:** Micrographs of $Xe(N_2)_2$-II in nitrogen. The sample darkens on compression. The while circles show where 514 nm laser light was incident on the sample in the photograph.

from the ambient light-sources in the laboratory. An example of transmission spectra in both visible and near infra-red are shown in Figure 5.9.

Transmission measurements present several complications inherent to working with DAC, particularly at megabar pressures. For example, the intensity of the transmitted light is affected not only by changes in the sample, but also by changes in gasket geometry caused by increasing pressure, and by chromatic aberrations caused by stresses in the diamonds. Consequently no quantitative conclusions could be drawn from the transmission measurements, although the observation of opaque reflective $Xe(N_2)_2$-II in xenon (Figure 5.10b) might be evidence for

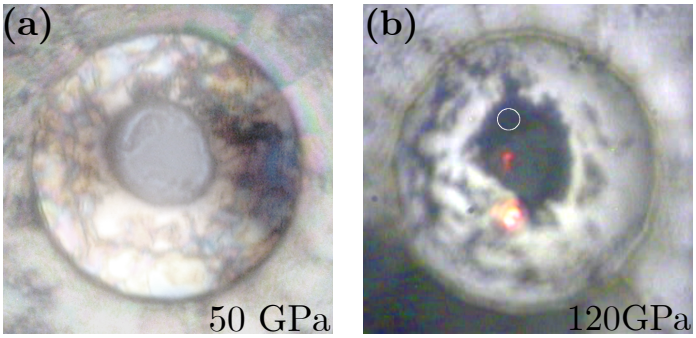

Figure 5.10: A sample of $Xe(N_2)_2$-II embedded in xenon (centre) and in nitrogen (surrounding region). (a) At 50 GPa the sample is transparent to visible light. **(b)** By 120 GPa the $Xe(N_2)_2$-II embedded in xenon becomes more reflective than the $Xe(N_2)_2$-II embedded in nitrogen. The white circles show where 647 nm laser light is shining on the sample in the photo. The image is a composite of three images.

metallisation of xenon at the slightly reduced pressure of 120 GPa compared to 130-150 GPa in pure xenon [Eremets 00]. Further investigations involving direct measurement of electrical transport properties would be required to confirm and metallic properties of $Xe(N_2)_2$-II in xenon. Absorbance spectra given in Figure A.1 in Appendix A show that $Xe(N_2)_2$-II in xenon is more absorbing to visible light than $Xe(N_2)_2$-II in nitrogen at the same pressures.

The sample shown in Figure 5.10 contains both nitrogen-rich and xenon-rich solids containing $Xe(N_2)_2$-II. In Figure 5.10a both regions are transparent to visible light at 50 GPa, where the polycrystalline nitrogen-rich solid around the edge of the sample appears slightly darker. By 120 GPa (Figure 5.10b) the central xenon-rich solid transmitted no observable light and reflected laser light, whilst the surrounding nitrogen-rich solid transmitted some light and did not reflect the laser light. The sample shown in Figure 5.9 contains only the polycrystalline nitrogen-rich solid and is still clearly transmitting at 156 GPa.

5.4 Discussion

This study constitutes the first comprehensive experimental study of the xenon-nitrogen system at high-pressures. The new $Xe(N_2)_2$ van der Waals compound transitions from a cubic structure ($Fd\bar{3}m$) to a body-centred tetragonal structure ($I4_1/amd$) at 14 GPa. The nitrogen molecules, which are rotationally disordered in the cubic structure, become ordered upon entering the tetragonal structure. A similar phenomenon is observed in pure nitrogen at a similar pressure of 16.3 GPa, where the partially disordered δ^*-nitrogen transitions to ϵ-nitrogen which is believed to be rotationally ordered [Mills 86]. Interestingly, the N≡N bond in the $Xe(N_2)_2$ compound was observed up to the maximum pressure studied of 180 GPa which surpasses the non-molecular limit in pure nitrogen where κ-nitrogen transition to the amorphous η-nitrogen at 150 GPa. Vibrational Raman spectra up to 175 GPa (shown in Figure 5.11) demonstrate the persistence of the N_2 vibrational band which, due to the broadening and negative frequency shift, probably weakens with increasing pressure. Laser heating to 3000 K was conducted by colleagues at the Spring-8 synchrotron at 120, 150, 160 and 180 GPa in attempt to encourage chemical reaction between nitrogen and xenon, however no changes were observed in the sample. The temperatures were estimated using the standard technique of fitting a Plankian distribution to the thermal emission spectrum [Goncharov 09]. The persistence of the N≡N bond to at least 175 GPa contradicts previous theoretical predictions of the formation of XeN_6 above 146 GPa whereby xenon atoms were predicted to be coordinated by two chaired N_6 molecules [Peng 15].

Doping the high-pressure xenon system with small amounts of oxygen has been shown to drastically reduce the metallisation pressure at ambient-temperature from 130 GPa to 49 GPa [Dewaele 12]. Whilst the observations made in this chapter are not sufficient to make any definitive claims about the metallisation of xenon doped with nitrogen, visual observations of the xenon-rich sample containing $Xe(N_2)_2$-II becoming opaque and reflective by 120 GPa might be considered

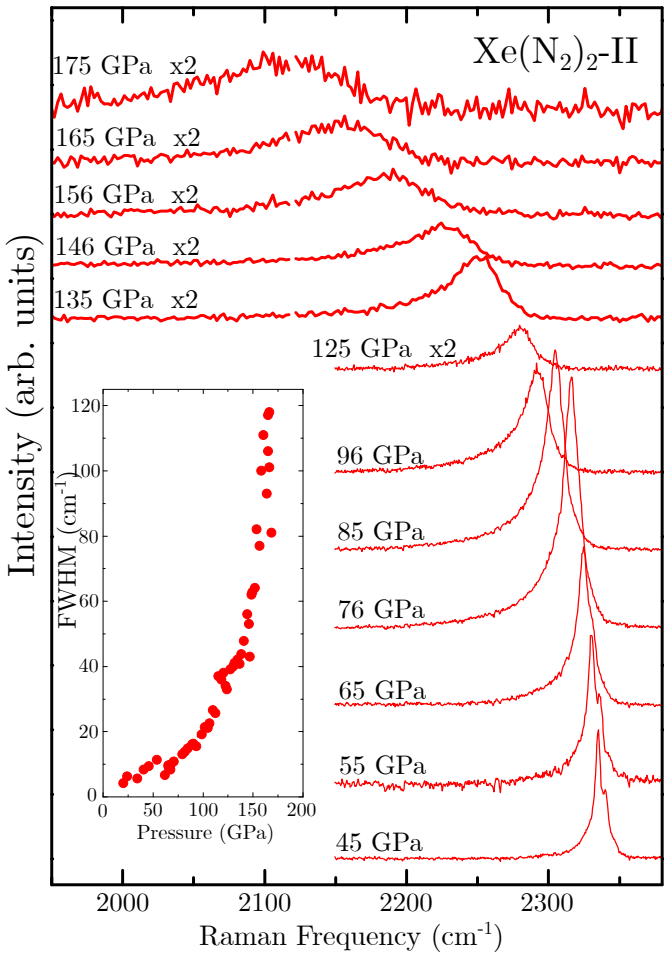

Figure 5.11: Vibrational Raman spectra of $Xe(N_2)_2$-II embedded in a xenon up to 175 GPa. Inset: Full-width-half-maximum plotted as a function of pressure. The vibrational band broadens and decreases in frequency with increasing pressure, suggesting that the N_2 inter-atomic bond weakens with pressure.

evidence for a reduced metallisation pressure. Further investigations involving direct measurement of electrical transport properties would be required to confirm and metallic properties of $Xe(N_2)_2$-II in xenon.

The discovery of a xenon-nitrogen van der Waals compound adds to the small but growing collection of known xenon-containing compounds at high-pressure conditions, other examples being $Xe(H_2)_7$ [Somayazulu 10] and $Xe(O_2)_2$ [Weck 10]. Over the last decades efforts have been made within high-pressure research to explain the observation that the terrestrial atmosphere contains less xenon than expected [Anders 77] and it appears as though the research is shifting away from geo-sciences and more towards the chemistry of xenon which was once considered totally inert [Sanloup 05].

The published work of this chapter can be found in the Publications section at the end of this thesis.

Chapter 6

Nitrogen-Hydrogen

6.1 Introduction

Molecules containing only nitrogen and hydrogen atoms are not unusual at ambient conditions. Indeed, the Haber process ($N_2 + 3H_2 \rightleftharpoons 2NH_3$) has been used to synthesise ammonia (NH_3) on an industrial scale since the early 1900s [Haber 22]. Other nitrogen-hydrogen compounds can exist at ambient conditions, such as: ammonium azide ($(NH_4)N_3$), hydrazine (N_2H_2), hydrazoic acid (HN_3) and tetrazene (N_4H_4), however, all of these are volatile and unstable to explosive conversion to N_2 and H_2. Understanding the behaviour of nitrogen and hydrogen molecular mixtures is of importance to many scientific fields ranging from the study of internal structures of astronomical bodies to the chemistry of amines ($-NH_2$), which spans from protein chemistry to biology.

The chemistry of nitrogen-hydrogen mixtures at extreme-conditions has only been experimentally investigated within the last ten years. Density functional theory (DFT) studies have predicted a number of novel nitrogen-hydrogen structures to be accessible at modest pressures, including N_2H, NH_4 and an N_9H_4 structure containing two-dimensional metallic nitrogen planes [Hu 11, Qian 16, Yin 15]. Although these structures remain to be observed experimentally, the va-

riety of predicted high-pressure structures suggests that ammonia may not be the most thermodynamically stable hydronitrogen at extreme conditions, an interesting implication of which is that the ice-giant planets (Uranus and Neptune, which consist primarily of water, ammonia and methane [Scandolo 03],) may contain less ammonia than currently thought.

The interaction of hydrogen and nitrogen at extreme-conditions is also of interest from an energetic material stand-point. The significant difference in bond-dissociation-energy between the nitrogen triple and single-bonds make extended nitrogen structures theoretically perfect high energy density materials (HEDMs) as they would have a maximal chemical energy density whilst producing only inert nitrogen as a reaction product [Eremets 04b]. The computational work of Rice *et al.* [Rice 07] finds that extended nitrogen structures (discussed in Chapter 4) might be stabilised to lower pressures by terminating nitrogen chains with hydrogen atoms. In their calculations the hydrogen was introduced to the nitrogen system *at* high-pressure (> 80 GPa), which, although not experimentally possible, certainly provides motivation for experimental investigation into how the behaviour of nitrogen at extreme conditions is modified by the inclusion of hydrogen.

The reverse perspective on the same issue is how the inclusion of nitrogen might affect the evolution of hydrogen structures with pressure. The study of pure hydrogen under extreme-conditions is a continual focus-point in extreme-conditions research because the hydrogen system represents an archetypal quantum solid which has been predicted to enter a metallic state once sufficiently compressed [Wigner 35]. Ashcroft [Ashcroft 04a] suggested that appropriately doping dense hydrogen could result in a significant increase in the average electron density, thereby promoting the onset of different hydrogen phases at pressures more readily achievable in DACs. Part of the motivation for the work of this chapter was to explore the effects of doping hydrogen with nitrogen, which seemed a promising candidate for producing interesting physics bearing in mind the predicted interactions described above.

Literature Review — Recent experimental work has explored nitrogen-hydrogen mixtures of various compositions up to 60 GPa at room-temperature [Ciezak 09, Galtsov 07, Goncharov 15, Laniel 18, Spaulding 14, Wang 15]. A consistent observation throughout the literature is a fluid-solid transition around 6 GPa which is characterised by the onset of strong inter-species interactions as observed in Raman spectroscopy. Spauding *et al.* [Spaulding 14] observed two different van der Waals solids in nitrogen-hydrogen mixtures, $(N_2)_6(H_2)_7$ and $N_2(H_2)_2$, depending on the mixture composition. The structure of the $(N_2)_6(H_2)_7$ solid was solved by single-crystal XRD and was found to be characterised by a host-guest structure of H_2 molecules contained within channels of orientationally ordered N_2 molecules. The structure of the $N_2(H_2)_2$ solid was recently determined by Laniel *et al.* [Laniel 18], and was similarly characterised by a host-guest structure of H_2 molecules encaged with N_2 molecules, except in this case the N_2 molecules show some orientational disorder at the same pressures ($\sim$ 9 GPa).

At pressures above 50 GPa all nitrogen-hydrogen compositions have been observed to undergo a chemical reaction, with changes in Raman spectra being attributed to the production of ionized NH_3 in an amorphous N_2 structure [Spaulding 14] or to single-bonded nitrogen oligomers [Goncharov 15, Wang 15]. Decompression of the solid phase to pressures below 10 GPa recovered hydrazine in all cases [Goncharov 15, Laniel 18, Spaulding 14, Wang 15].

The only study on the deuterium–nitrogen system observed quite different behaviour with a transition to a non-crystalline solid at 5 GPa and an incommensurate host-guest structure with stoichiometry $(N_2)_{12}D_2$ at 10 GPa [Kim 11]. The host-guest type structure of H_2 or D_2 molecules encaged in N_2 molecules is a shared characteristic of both systems, but the isotope effect on structure adds an additional level of complexity to the nitrogen-hydrogen system. Although isotope effects are not investigated in the work of this thesis it would be an interesting direction for future studies.

This Work — In this chapter the reactivity of nitrogen-hydrogen mixtures and their high-pressure structures was explored as a function of composition and pressure. Room and high-temperature (890 K) Raman experiments demonstrated a *P-T* path-dependent synthesis of hydrazine *or* ammonia which has possible implications for gas-giant planets. Powder XRD data revealed that up to at least 59 mol% H_2 the nitrogen-hydrogen mixtures adopted the hexagonal $R\bar{3}m$ structure of Spaulding *et al.* [Spaulding 14] which formed mixed powders with the cubic $P\bar{4}3m$ solid of Laniel *et al.* [Laniel 18] when the hydrogen content was increased up to 75 mol%. The 75 mol% H_2 mixture was compressed up to 242 GPa, demonstrating the first megabar study of the nitrogen-hydrogen system in which the two species were not mutually soluble.

6.2 Methods

Sample Preparation — Nitrogen-hydrogen mixtures were prepared at 5 MPa and given several days to homogenise before being gas loaded into DACs at 200 MPa. Eight different nitrogen-hydrogen compositions were studied in total, with compositions of: 16, 28, 43, 50, 59, 67, 75 and 83 mol% H_2 as determined from the relative partial pressures[†]. The pure species were also studied under the same conditions for comparison. External resistive-heaters were used for high-temperature Raman experiments in piston-cylinder type DACs. Raman spectroscopy was conducted using 514 and 647 nm excitation wavelengths as described in section 3.4 and pressure was monitored using the ruby-fluorescence and diamond-edge scales described in section 3.1.1. Rhenium gaskets were gold-sputtered to prevent hydrogen diffusion into the gasket. BA diamonds with 200 μm culets were used in experiments up to 50 GPa in piston-cylinder type DACs, and in symmetric-type DACs for XRD experiments. 40 μm culets were used in piston-cylinder type DACs for the megabar pressures.

[†]N.B. All nitrogen-hydrogen mixture compositions in this chapter are referred to by their mol% H_2.

X-ray Diffraction — X-ray diffraction data were acquired at PETRA-III at the P02.2 Extreme Conditions Beamline (Hamburg, Germany). Patterns were generated using a monochromatic beam of $\lambda = 0.4847$ Å. Data were recorded on a Mar 345 IP area detector and integrated in Dioptas [Prescher 15].

6.3 Results

Room-temperature Raman Spectroscopy — All nitrogen-hydrogen compositions were homogeneous fluids below 8 GPa which exhibited no phase-separation either visually or in Raman spectroscopy. In this fluid state only weak intermolecular interactions were observed and all Raman modes were accounted for by those of the pure species, although a slight hardening of the hydrogen Raman vibron with increasing nitrogen content was observed. Figure 6.1 acts as a summary of the Raman spectra collected across the eight different compositions up to 50 GPa at room-temperature. Spectra of the pure species are included for comparison. Whilst previous studies have published composition-specific Raman spectra, comprehensive Raman across all concentrations has not been made available as found here. Interestingly, the solidification pressure around 8 GPa is higher than that for either of the pure species: 2.4 GPa for nitrogen and 5.5 GPa for hydrogen. The fluid to solid transition around 8 GPa was confirmed by XRD measurements and was accompanied by the appearance of additional Raman modes as seen in Figure 6.2.

The nature of the additional Raman excitation bands in the solid state depended strongly on the composition of the initial mixture. The hydrogen rotational modes (Figure 6.1b) showed little deviation from the behaviour of pure hydrogen under the same conditions, supporting the rotationally disordered hydrogen in the suggested structures of refs. [Spaulding 14] and [Laniel 18]. The hydrogen vibron showed significant hardening and splitting with the addition of nitrogen (Figure 6.1d), indicating that the H_2 molecules occupied distinct crys-

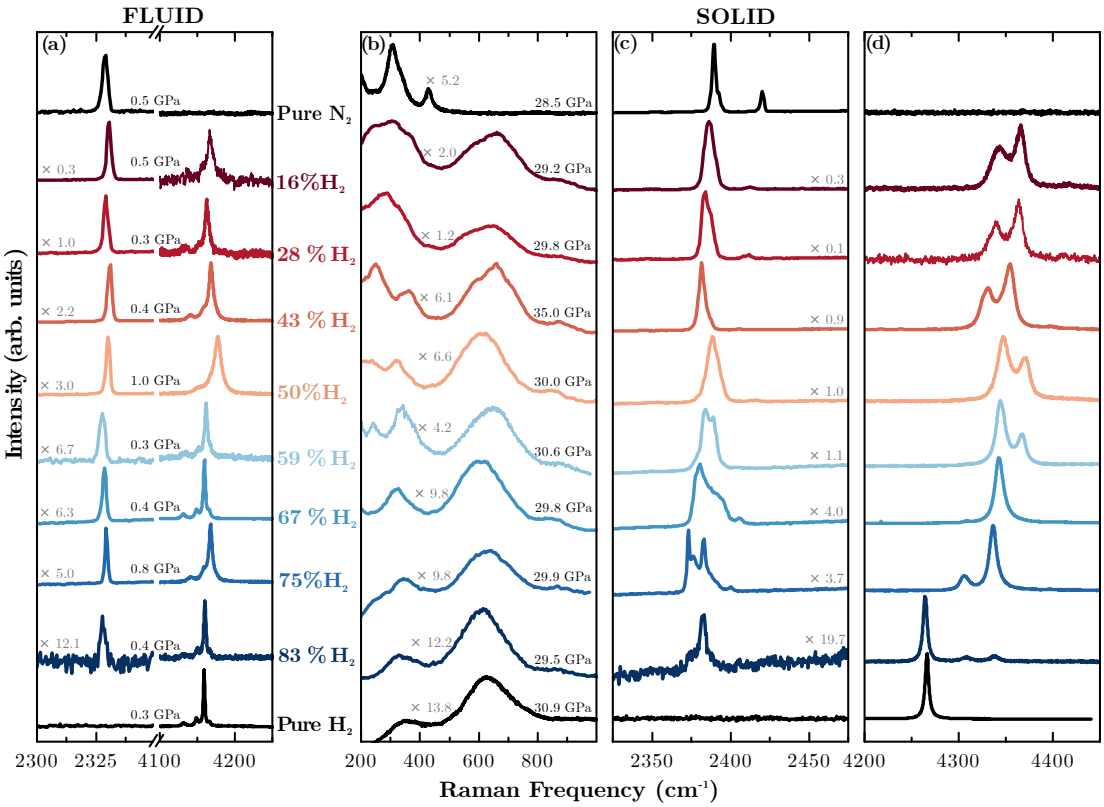

Figure 6.1: Evolution of the Raman spectra with composition in (a) the fluid phase at around 0.5 GPa and in (b-d) the solid phase at around 30 GPa: **(b)** the low-frequency Raman modes; **(c)** the N_2 vibrational modes; and **(d)** the H_2 vibrational modes. The pure species are included for comparison in black. The intensities have been rescaled relative to the hydrogen vibron as indicated to allow for easier comparison.

tallographic sites within the solid. At around 50 GPa the highest frequency hydrogen vibrons for each mixture showed a positive frequency shift of over 200 cm^{-1}, which is similar to observations of the hydrogen embedded in noble gas matrices [Loubeyre 92]. The split hydrogen vibrons showed no sign of the classical hydrogen vibron turnover in frequency (around 35 GPa) and continued to increase in frequency up to the highest pressures studied in all compositions. Due to the scaling in the summary Figure 6.1 some of the weaker hydrogen vibrational modes are not visible. Full compression spectra for each of the individual compositions summarised in Figure 6.1 can be found in Appendix B. An example of peak fitting is given in Figure 6.3.

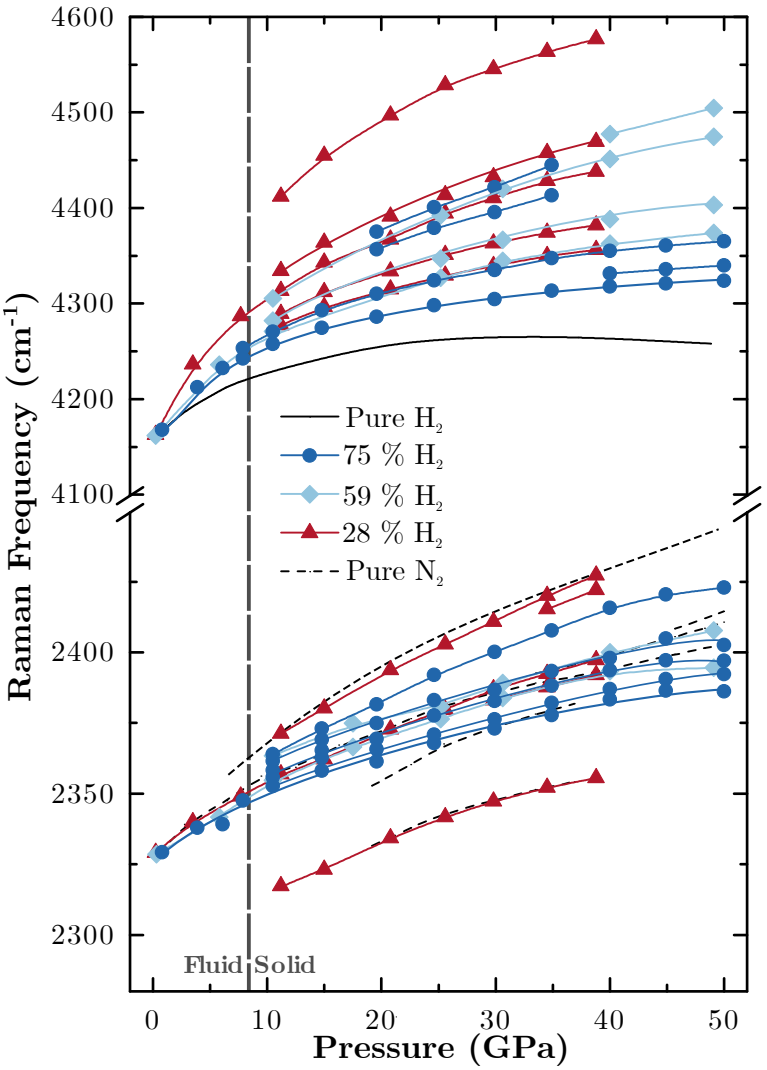

Figure 6.2: A plot of Raman frequency against pressure for the nitrogen-hydrogen compositions of: 28, 59 and 75 mol% H_2. Solid black lines are pure H_2. Dashed black lines are pure N_2. The onset of strong inter-species interactions is clear on crossing the fluid → solid transition marked by the vertical dashed line. The three compositions in the Figure were also studied via XRD (shown in Figure 6.4).

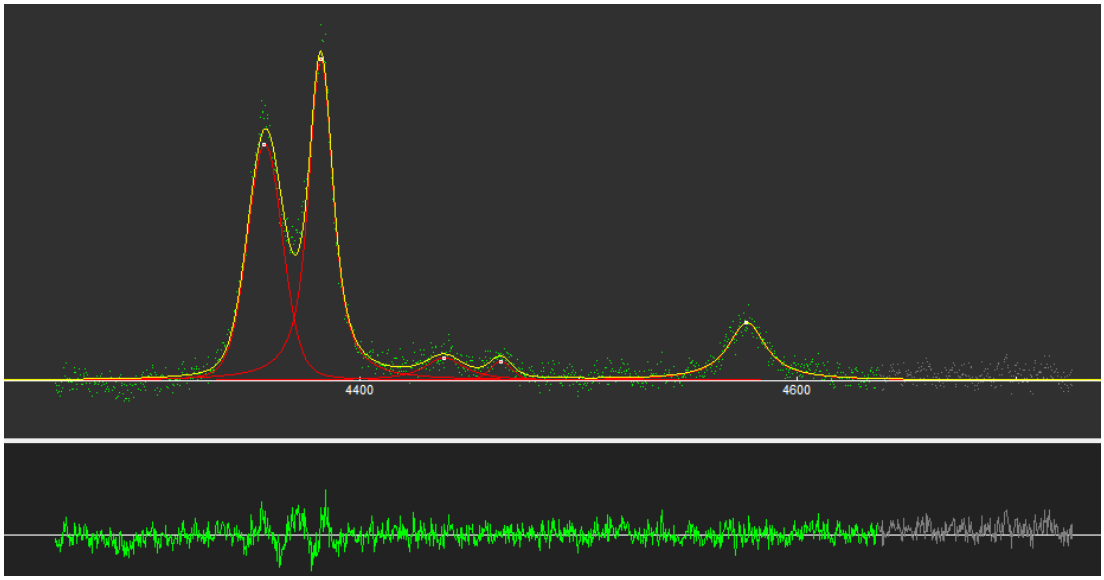

Figure 6.3: An example of peak fitting in this study using Fityk [Wojdyr 10]. The spectrum is of 28 mol% H_2 at 38.8 GPa.

X-ray Diffraction — Powder XRD was performed on samples with compositions of 28, 59 and 75 mol% H_2 in order to further probe the structure of the nitrogen-hydrogen solids. The compositions of of 28, 59 and 75 mol% H_2 were chosen because they span the range of behaviours observed in the Raman spectra, and are representative of hydrogen-rich, nitrogen-rich and roughly equal compositions. The integrated diffraction patterns are shown in Figure 6.4 and were collected at just above the solidification pressure between 9 and 10 GPa.

The diffraction patterns from the two most hydrogen-deficient samples (28 and 59 mol% H_2) revealed mixed powders of two structures. Firstly, δ-N_2 was observed, which is consistent with room-temperature compression of pure N_2 between 4.9 and 10.5 GPa [Stinton 09]. Diffraction lines from δ-N_2 are marked with blue arrows in Figures 6.4a and 6.4b. The intensity of the δ-N_2 diffraction lines decreased with deceasing nitrogen content. Secondly, the diffraction lines not arising from δ-N_2 were accounted for by the hexagonal $R\bar{3}m$ nitrogen-hydrogen structure proposed by Spaulding *et al.* [Spaulding 14]. The $R\bar{3}m$ structure had unit cell dimensions of: $a = 14.0656(11)$ Å, $c = 7.9521(8)$ Å at 10 GPa and is labelled in black in Figure 6.4.

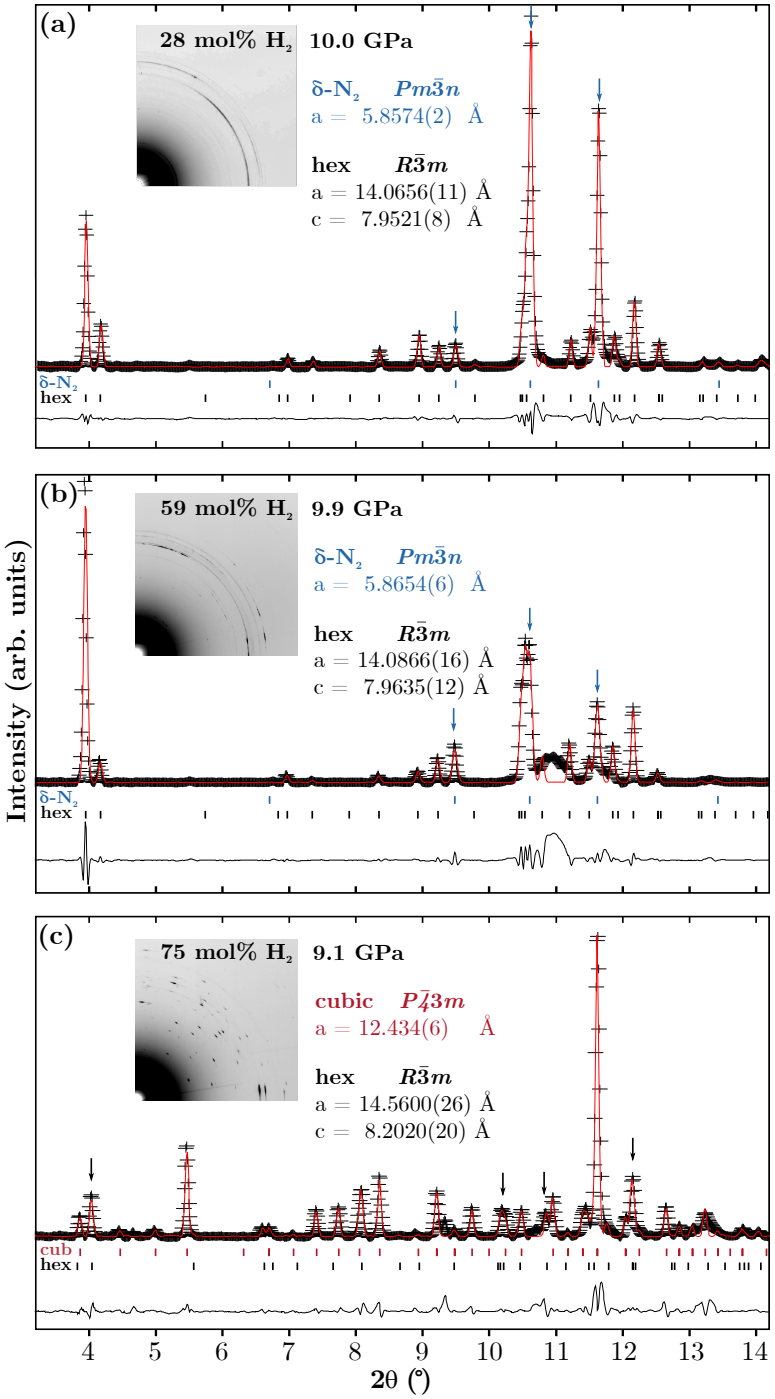

Figure 6.4: Le Bail fits (red lines) to experimental powder XRD data (black crosses) for three samples of different hydrogen content: (a) 28 mol% H_2, (b) 58 mol% H_2 and (c) 75 mol% H_2. In **(a)** and **(b)** the diffraction lines marked with blue arrows are indexed to δ-N_2, the principal vibron of which is also observed in the Raman spectra. All other peaks are indexed by an $R\bar{3}m$ hexagonal structure. (The unindexed line in **(b)** at 11° does not correspond to any nitrogen structure and is believed to be due to sample contamination.) In **(c)** the peaks marked with black arrows can only be fitted by the $R\bar{3}m$ phase which has not been observed before in such a hydrogen-rich composition. All others lines are indexed by a cubic $P\bar{4}3m$ space group. **Insets:** Sections of the unintegrated diffraction images. XRD data in this chapter were collected and analysed by the author.

In the 75 mol% H_2 sample (Figure 6.4c) the diffraction lines showed the aforementioned hexagonal $R\bar{3}m$ solid mixed with another solid which was not δ-N_2. The new diffraction lines were be indexed to a cubic $P\bar{4}3m$ solid with a = 12.4346(6) Å at 9.1 GPa, consistent with the structure proposed by Laniel *et al.* [Laniel 18]. The cubic phase is labelled in red in Figure 6.4c.

High-temperature Raman Spectroscopy — Nitrogen-hydrogen mixtures of all compositions exhibited loss of intensity of the hydrogen and nitrogen Raman vibrational bands over hour-long time-scales above the critical pressure of 50 GPa at room-temperature. The loss of vibron intensity occurred simultaneously with the emergence of a broad asymmetric peak centred around 3400 cm^{-1} (highlighted in blue in Figure 6.5a) which can be attributed to the formation of N–H vibrational modes and therefore indicates a chemical reaction between the two species. On subsequent decompression to below 10 GPa the broad peak around 3400 cm^{-1} evolved into two sharp peaks accompanied by four lower frequency modes at 4 GPa (see the blue spectrum in Figure 6.5a), unambiguously identifying hydrazine [Jiang 14] in the decompressed sample. The blue spectrum of Figure 6.5a shows a mixture of solid hydrazine and unreacted molecular nitrogen and hydrogen. Solid hydrazine was observed on decompression below 10 GPa in all isothermal compression-decompression experiments at room-temperature after the sample had been held above 50 GPa to allow the formation of N-H bonds. Interestingly, ammonia (NH_3) rather than hydrazine (H_2N–NH_2) was recovered on decompression at room-temperature after heating the sample to high-temperatures.

The decrease in vibron intensity and emergence of a Raman peak around 3400 cm^{-1} which occured at room-temperature above 50 GPa was observed in the fluid-state at much lower pressures around 3 GPa when the sample was heated. In the 50 mol% H_2 sample in Figure 6.5b the hydrogen vibron had completely disappeared by 890 K at 3 GPa (see the red spectrum) and the peak attributed to N-H bonds was sharply defined. On cooling back to room-temperature, a fluid $\rightarrow$ solid transition was observed visually at 450 K, and the Raman peak around 3400 cm^{-1} began to broaden (highlighted in green in Figure 6.5b), ultimately

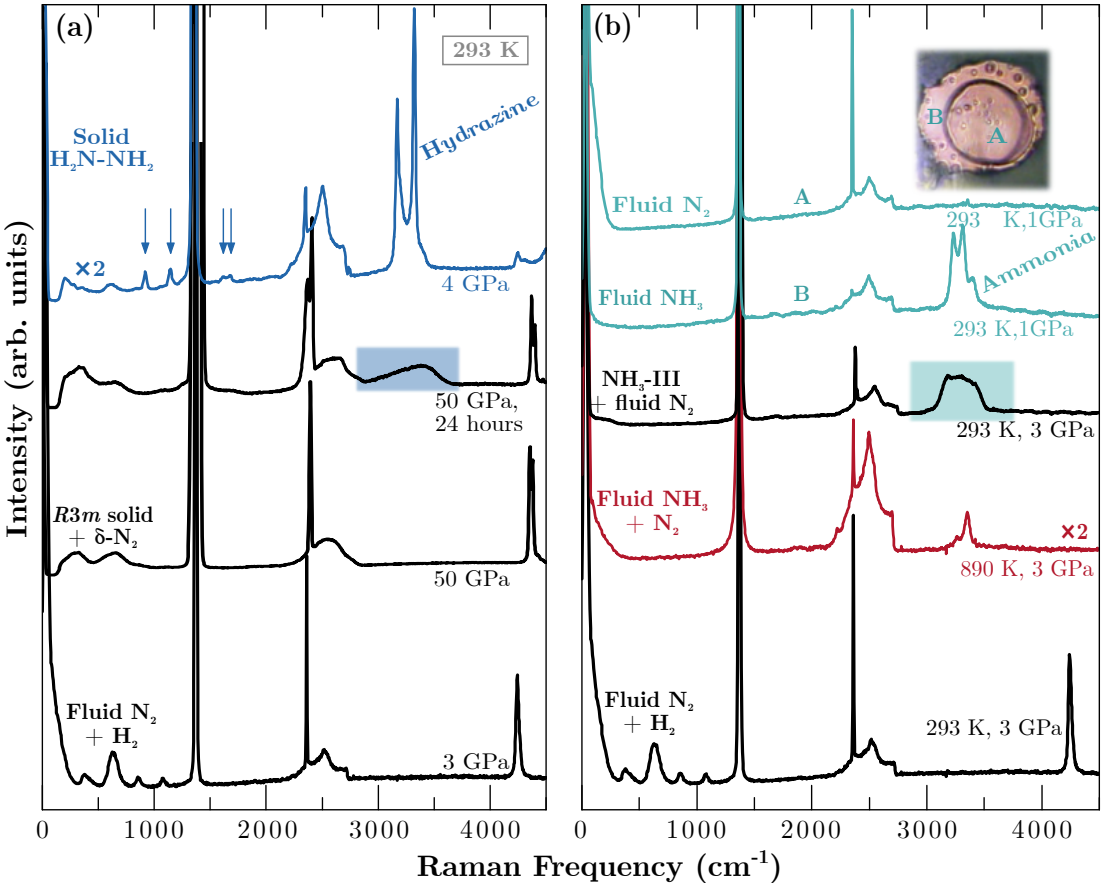

Figure 6.5: Raman spectra of a 50 mol% H_2 composition demonstrating the *P-T* path-dependent synthesis of (a) hydrazine and (b) ammonia from the same initial sample composition and *P-T* conditions. Inset: Photograph of the sample after decompression to 1 GPa showing a bubble of N_2 surrounded by NH_3.

appearing very similar to the room-temperature decompressed sample of Fig 6.5a, but at the much lower pressure of 3 GPa. The broad peak highlighted in Fig 6.5b corresponds to phase-III of ammonia at 3 GPa [Ninet 16, Ojwang 12]. On decompression to 1 GPa the broad ammonia peak evolved into 3 sharp peaks unambiguously indicating fluid ammonia [Lundeen 75] which was consistent with the observed fluid $\rightarrow$ solid transition around 450 K at 3 GPa [Ojwang 12].

Megabar Raman — Megabar Raman studies of the nitrogen-hydrogen system have so far only investigated very lightly doped samples. For example, 95 mol% H_2 and 4 mol% H_2 compositions were studied up to 241 and 250 GPa respectively (supplementary information of ref. [Eremets 11] and of ref. [Spaulding 14]). In each case the observed sample behaviour was that of the majority constituent, suggesting that there is a solid solubility of at least 5 mol% of either H_2 or N_2 in the other up to megabar pressures. In this work a nitrogen-hydrogen mixture of 75 mol% hydrogen composition was compressed up to 242 GPa. The 75 mol% hydrogen composition was chosen to match the stoichiometry of ammonia. In the 75 mol% hydrogen composition the observed sample behaviour is not that of either of the pure species even at low pressures as discussed previously (see for example the XRD data in Figure 6.4c), making this the first megabar study of the nitrogen-hydrogen system in which there species were not mutually soluble.

The decreasing intensity of the hydrogen and nitrogen vibrons which occurred over hour-long time scales at room-temperature and 50 GPa occurred over second-long timescales by 70 GPa, suggesting that the formation of N-H bonds was facilitated by higher pressures. Further compression resulted in complete loss of the hydrogen vibron at 138 GPa. The broad peak centred around 3400 cm^{-1}, arising from N-H bonding, continuously hardened to at least 172 GPa (see Figure 6.6a). Pressure was increased to 242 GPa, however broadening and loss of intensity prevented unambiguous identification of any peaks at pressures higher than 172 GPa and consequently no further changes were observed up to the maximum pressure.

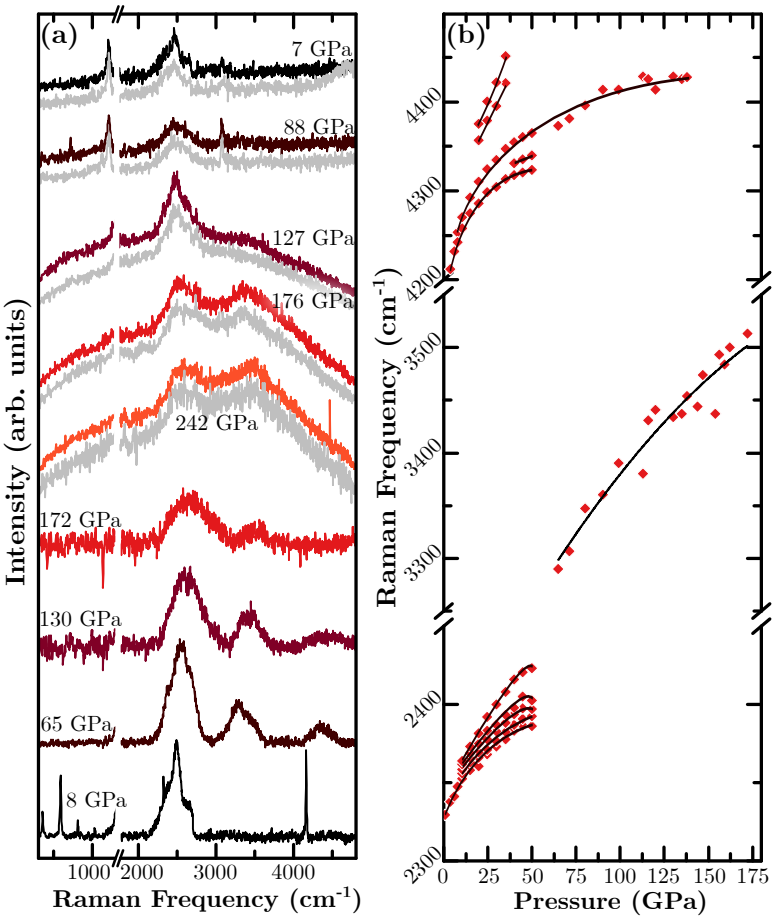

Figure 6.6: Raman data of the 75 mol% H_2 composition up to 242 GPa. **(a)** Evolution of Raman spectra with pressure on compression and decompression. The grey spectra were acquired from the gasket close to the sample for comparison and show that all decompression peaks arose from the diamond/gasket. **(b)** The Raman frequency plotted against pressure corresponding to the spectra shown in (a).

The disappearance of Raman modes above 172 GPa roughly corresponds to the formation of the Raman-inactive η-N_2 phase of pure nitrogen at 150 GPa [Goncharov 00], however unlike the η-N_2 phase which is visibly dark, the nitrogen-hydrogen sample remained transparent up to the maximum pressure of 242 GPa.

At 242 GPa no detectable structural or chemical changes could be stimulated by exposing the sample to intense super-continuum laser light. On decompression the sample remained Raman-inactive and transparent to 7 GPa at which pressure the cell opened and the sample was lost. All Raman features in the decompression spectra can be accounted for by comparison with the gasket material (which is shown in grey for comparison in 6.6a).

6.4 Discussion

Megabar Raman — The results of the megabar experiment are perhaps the most intriguing of this Chapter and are the first to show nitrogen-hydrogen mixtures in the megabar regime in which they are not mutually soluble. At the maximum pressure of 242 GPa the sample of 75 mol% H_2 composition remained transparent yet Raman inactive. Under these conditions pure nitrogen is also Raman inactive (η-nitrogen) but is optically opaque. Pure hydrogen is transparent under these conditions, but does exhibits a Raman signal, so the megabar system differentiates itself from either of its pure constituents. Perhaps even more intriguing was the observation that the sample remained Raman inactive on decompression to at least 7 GPa (when the sample was lost). Pure nitrogen would be expected back transform though the $\zeta', \zeta, \epsilon, \delta^*, \delta$-phases from 242 $\rightarrow$ 7 GPa, whereas the nitrogen-hydrogen mixture showed no indications of structural changes on decompression. Based on the observations of this one experiment it might be suggested that the presence of hydrogen stabilised the Raman-inactive η-N_2-*like* sample to lower pressures as suggested by Rice *et al.* [Rice 07]. However, the lack of a hydrogen vibrational mode in the Raman spectra may indicate

that the hydrogen from the sample had diffused into the rhenium gasket due to imperfect gold sputtering ([Scheler 11]). The experiment should be repeated and a clear-path has been laid for a direction of future study.

High-temperature Raman — The recovery of ammonia rather than hydrazine on decompression after high-temperature conditions has not been observed in the current literature and may be a kinetic effect due to the fact that the sample was in the fluid state rather than the solid. However, it is unclear based on these results alone whether temperature or pressure is the dominant factor. In the high-temperature experiment the reaction conditions closely mimicked those of the industrial Haber–Bosch equilibrium reaction ($N_2 + 3H_2 \rightleftharpoons 2NH_3$ [Haber 22]) in terms of temperature (around 800 K), but the *pressure* in the experiment was at least two orders of magnitude greater (3 GPa *vs.* 0.02 GPa) and may represent the highest pressure experimental demonstration of the Haber–Bosch process. In order to explore more realistically what kinds of nitrogen-hydrogen species exists in the ice-giant planets (in which conditions can reach 1000s of Kelvin and 100s of GPa [Nellis 12]) it would be necessary to conduct experiments which combine the high-temperature and high-pressure conditions which have been investigated separately here. The P-T path-dependence shows that on recovery to room-temperature the same initial configuration can produce ammonia or hydrazine, yet what species are present when the sample is at the extreme conditions similar to those in ice-giant planets is not yet known.

X-ray Diffraction — The powder XRD patterns acquired from the solid nitrogen-hydrogen mixtures in this work were compatible with the structures determined through single-crystal XRD by Spauding *et al.* [Spaulding 14] and very recently by Laniel *et al.* [Laniel 18]. Although these findings are not new the work of this chapter was exploratory and successfully repeated the experiments of others finding consistent results. The new findings of the mega-bar and high-temperature Raman experiments show that there remain unanswered questions about the behaviour of the nitrogen-hydrogen system at extreme conditions and a path has been suggested for future studies.

Chapter 7

ι-Nitrogen

7.1 Introduction

Chapter 4 introduced the reader to the elemental nitrogen system at extreme conditions. The aim of the contributing work in this chapter was to determine the structure of the high-temperature polymorph, ι-nitrogen, which had remained unknown prior to this investigation.

The ι-phase of nitrogen is one of two known molecular phases which is accessible only at high-temperature high-pressure conditions, the other phase being θ-nitrogen [Gregoryanz 02]. The ι and θ-nitrogen phases have remained relatively unexplored since their discovery 16 years ago, for three key reasons: 1) the experimental conditions required for their synthesis are very challenging, 2) the phases appear to be sensitive to the P-T path taken to the synthesis conditions of their formation, and, 3) once formed it is challenging to extract structural information from high-pressure nitrogen samples in DACs.

The reported successful P-T paths to both ι and θ-nitrogen are shown in the nitrogen phase-diagram in Figure 7.1. The two phases have largely been probed only via Raman and infra-red spectroscopies, which, whilst revealing information

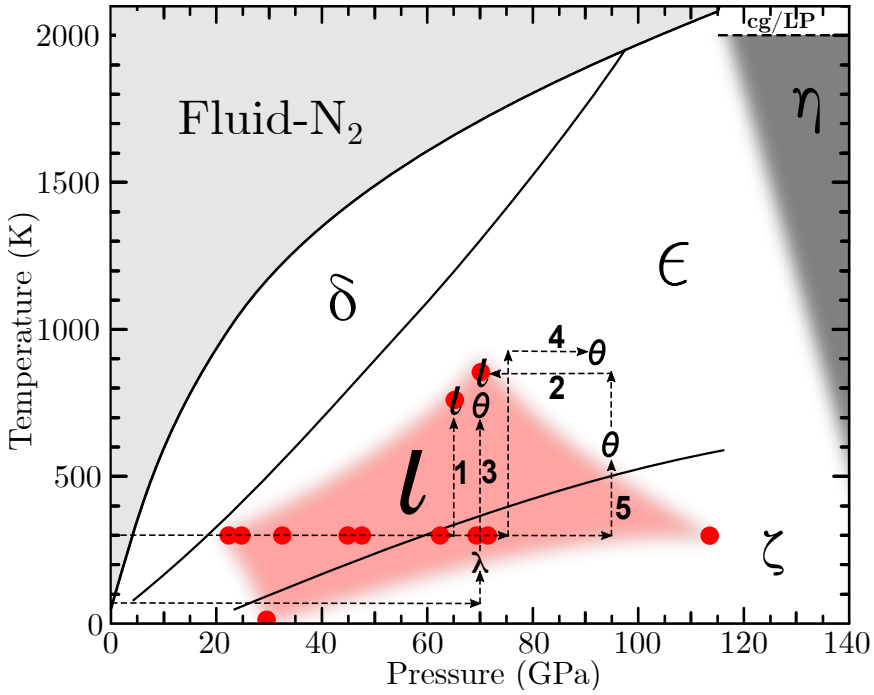

Figure 7.1: a) The nitrogen phase-diagram. The reported P-T paths to the high-temperature molecular phases ι-nitrogen (paths 1 and 2) and θ-nitrogen (paths 3, 4 and 5) are shown with dashed arrows. The red overlay illustrates the observed stability region of ι-nitrogen. The P-T path are as follows: **Path 1)** Isobaric heating of ϵ-nitrogen to 750 K at 65 GPa. **Path 2)** Isothermal decompression of θ-nitrogen to 69 GPa at 850 K. **Path 3)** Isobaric heating of λ-nitrogen to 800 K at 70 GPa. **Path 4)** Isothermal compression of ϵ-nitrogen to 97 GPa at 920 K. **Path 5)** Isobaric heating of ϵ-nitrogen to 600 K at 95 GPa. P-T paths and data points are taken from refs. [Frost 16, Goncharov 08, Gregoryanz 02, Tomasino 14a]. Black phase-boundaries are based on refs. [Goncharov 08, Tomasino 14a, Weck 2017]. Phases α, β, γ, δ', ζ', κ, θ and λ are omitted for clarity.

about the constituent molecules, tell little about the crystal structure. The remainder of this chapter strictly focusses on ι-nitrogen until the discussion section at the end, however it is worthwhile to mention θ-nitrogen here because it is the only other molecular high-temperature phase and its structure remains unknown.

Literature review — There are a number of discrepancies in the literature regarding the P-T conditions necessary to access ι-nitrogen, with no single research group being able to reproduce the results of another. The discovering article, ref. [Gregoryanz 02], provides the only published data from a sample of ι-nitrogen to date, having first synthesised ι-nitrogen by heating ϵ-nitrogen to 750 K at 65

GPa (P-T path 1 in Figure 7.1), and by isothermal decompression of θ-nitrogen to 69 GPa at 850 K (P-T path 2).

In Raman experiments into the melting-curve of nitrogen, ref. [Goncharov 08] claims to have accessed ι-nitrogen by temperature quenching fluid nitrogen between 48 and 114 GPa, although nowhere in the article or supplementary materials are ι-nitrogen spectra presented and it is not clear at what P-T conditions the onset of ι-nitrogen was observed. In simliar XRD work on the melting curve, ref. [Weck 2017] observed the recrystallization of the fluid into δ-nitrogen and ϵ-nitrogen (as illustrated by the melt-line in Figure 7.1) without observing ι-nitrogen despite passing through the P-T conditions necessary for its formation. Ref. [Tomasino 14b] reported that they were unable to synthesise ι-nitrogen despite an *extensive search over a wide range of pressures, temperatures, and thermal paths*, remarking that heating rate may be an important factor. Thus, the original experiments of ref. [Gregoryanz 02] have remained unrepeated (until this work) and the characterisation of ι-nitrogen has been hindered by an apparent sample sensitivity to the P-T path taken to the formation synthesis conditions.

The spectroscopic data of ref. [Gregoryanz 02] are of sufficient quality to distinguish ι-nitrogen from other nitrogen phases, and indeed correctly identify ι-nitrogen as containing only molecular N_2 units. However, the powder XRD data provide little insight into the structure and primarily consist of intense diffraction lines from the rhenium gasket. In the 16 years since the discovery of ι-nitrogen many advancements have been made in high-pressure XRD techniques, and it was the aim of this study was to investigate the structure of ι-nitrogen by utilising modern high-pressure crystallography techniques in combination with improved DAC designs, resistive heating techniques and high-pressure Raman techniques.

This work — The structure of ι-nitrogen was probed with Raman spectroscopy and single-crystal X-ray diffraction techniques. The data were of sufficient quality to solve and refine a structural model for ι-nitrogen[†] which was found to

[†]The analysis and subsequent refinement of the single-crystal X-ray diffraction data pre-

be the most complex nitrogen phase with an unusually large primitive unit-cell containing 48 N_2 molecules.

The discussion section at the end of this chapter includes a review of the ι, θ and λ-nitrogen phases which was motivated by the sparsity of discussion relating to those phases in the literature. When referring to the nitrogen phase-diagram, these phases are often overlooked and they may be related to each other in terms of structure.

7.2 Methods

Sample Loading — Research-grade nitrogen was cryogenically loaded into DACs as described in section 3.2.1.

Heating Techniques — The elevated temperatures of 750 K were achieved through graphite internal resistive heaters described in detail in section 3.3. Typically, the heating rates used in successful experiments were around 100 K min^{-1}, which is much slower than the 50 K sec^{-1} reported in the unsuccessful experiments of ref. [Tomasino 14a]. The power needed to achieve and maintain temperatures of 750 K was typically around 250 Watts (i.e. 50 Amps across 5 Volts). Resistive-heating was chosen over laser-heating because it is easier to control and monitor the sample temperature whilst minimising temperature-gradients by heating the entire sample chamber such that the temperature profile across the sample is more uniform.

DAC Constraints — Four-post symmetric-type DACs were necessary for the XRD experiments because they allow for larger oscillations in ω without cutting the X-ray beam. Piston-cylinder type DACs can reach higher pressures due to their more reproducible and consistent alignment with increasing pressure, however they are limited to Raman spectroscopy experiments. Pressures

sented in this chapter was the sole work of collaborators Dr Jack Binns and Dr Michael Hanfland.

above 50 GPa are not generally attempted in symmetric-type DACs because the variable alignment is more pronounced with smaller diamonds and can lead to misalignment and anvil failure with increasing pressure. Symmetric-type DACs have very tight spatial constraints inside the cell, thus necessitating the use of graphite heaters (instead of coil heaters) to generate the high-temperature conditions because the graphite lies flat between the two halves of the cell. The high-temperature conditions also necessitated use of DACs made of low thermal-expansion René-41 in order to better control the pressure at high-temperatures. Boehler-Almax (BA) diamonds with 200 μm culets were used with corresponding wide-angle BA seats which allowed rotation of the sample through $\omega = 60^\circ$ during XRD data acquisition.

Pressure Control — The pressure in the loaded DACs was initially increased to 40 GPa on the load-screws, followed by a further increase from 40 to 65 GPa using a gas-membrane. The pressure was monitored with the diamond edge scale described in experimental section 3.1.1. After the high-temperature $\epsilon \rightarrow \iota$-nitrogen phase-transition had been observed visually (as seen in Figure 7.2) the power-supply was cut, and the DACs were allowed to cool to room-temperature whilst the pressure was monitored. The sample-pressure typically increases as DACs cool because the initial load on the screws which was lost to internal friction begins to relax at high-temperature conditions. The pressure was kept constant as the DAC cooled by removing pressure from the gas-membrane. Once at room-temperature, and with the load from the gas-membrane completely removed, it was possible to disconnect the DAC from the experimental set-up and recover the ι-nitrogen single-crystals intact.

X-ray Diffraction — Single-crystal X-ray diffraction data were acquired at PETRA-III at the P02.2 Extreme Conditions Beamline (Hamburg, Germany). Patterns were generated using a monochromatic beam of wavelength $\lambda = 0.2889$ Å which was focused to a spot size of 4×4 μm. The patterns were recorded on a PerkinElmer XRD 1621 detector. The sample was rotated about ω over a range of 56° in 1° steps. Despite the high quality of the data (shown later in Figure 7.4)

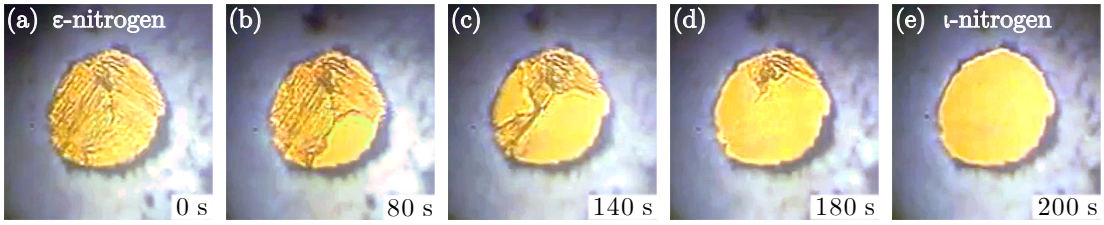

Figure 7.2: Micrographs showing the visual change across the $\epsilon \rightarrow \iota$ phase-transition at 750 K and 65 GPa. (a) ϵ-nitrogen has a birefringent (coarse) visual appearance. (b-d) ϵ-nitrogen transforms to ι-nitrogen as crystals grow across the sample chamber. (e) ι-nitrogen has a smooth visual appearance. The sample chamber is approximately 60 × 60 um. The time of the transition is shown in seconds on each frame.

a low data coverage along one of the crystal axes (which was almost perpendicular to the diamond culets) and an incomplete data set prevented determination of the atomic positions. Consequently, additional single-crystal X-ray diffraction data were collected at the ID15B beamline at ESRF (Grenoble, France), using a monochromatic beam $\lambda = 0.411$ Å focused to a spot size of 10 × 10 μm. Data were recorded on a MAR555 flat panel detector. The sample was rotated about ω over a range of 60° in 0.5° steps and a full data set collected.

7.3 Results

ι-nitrogen was accessed following the experimental conditions of ref. [Gregoryanz 02] by isobarically heating ϵ-nitrogen to 750 K at 65 GPa. The P-T path is illustrated by path 1 in Figure 7.1. The $\epsilon \rightarrow \iota$-nitrogen phase-transition was initially observed visually as seen in Figure 7.2. ϵ-nitrogen samples tends to have a coarse (or birefringent) visual appearance which became smooth on transformation to ι-nitrogen. Grain boundaries were observed moving slowly across the sample, with the transition going to completion typically within three to four minutes. The resistive-heating technique used in the contributing work allowed the P-T conditions in the sample to be held constant for minutes, rather than seconds, thus allowing the completion of the phase transition.

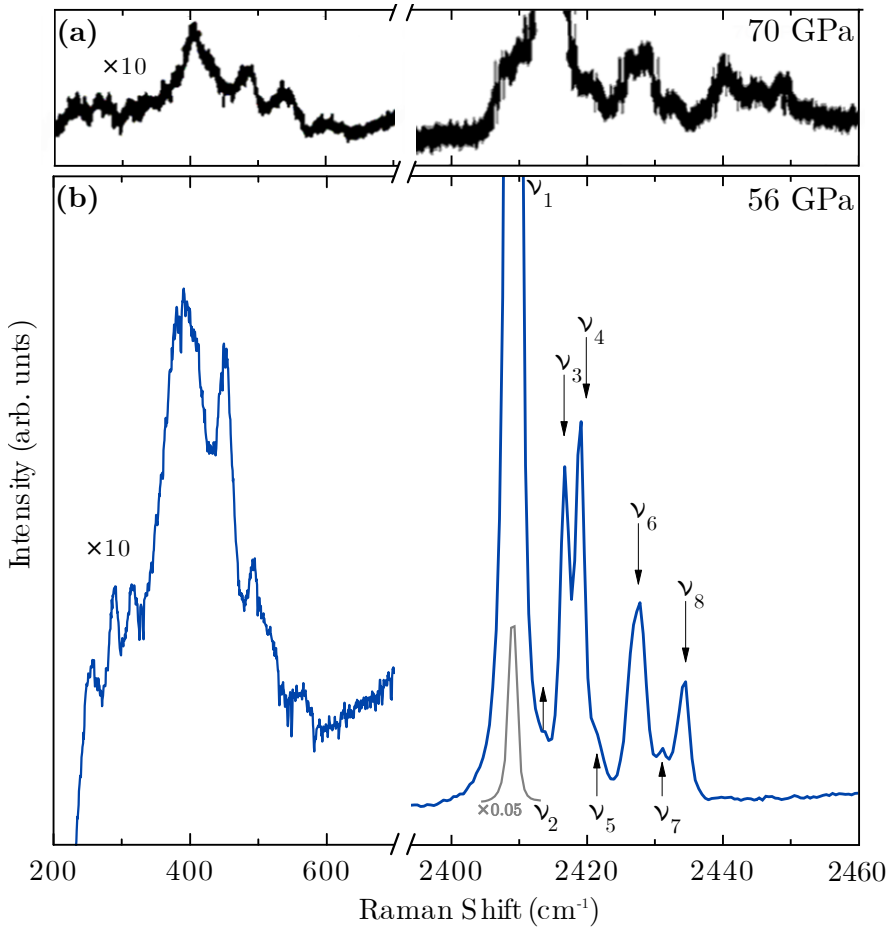

Figure 7.3: Raman spectra of ι-nitrogen. (a) The spectra from the previous work of ref. [Gregoryanz 02]. **(b)** The spectra from the contributing work of this thesis. The intensity of the low-frequency modes has been multiplied by a factor of 10 for clarity. The grey inset spectrum in Figure (b) shows ν_1 scaled by a factor of 0.05 to display its full singlet profile.

Raman Spectra — Once recovered to room-temperature the phase-transition was confirmed by comparison of the Raman spectrum with the ι-nitrogen Raman spectrum presented in ref. [Gregoryanz 02]. The ι-nitrogen Raman spectra obtained in the contributing work (shown blue in Figure 7.3) display the ι-phase with significantly improved resolution and signal to noise ratio such that individual modes may now be distinguished. The original spectra of ref. [Gregoryanz 02] are included in black in Figure 7.3 for comparison with the spectra of this work. The relative shift in vibron frequency is due to the difference in sample pressure.

The lowest frequency vibrational mode (labelled ν_1) is the most intense by

a factor of approximately 10. A scaled down inset of ν_1 is shown in grey in Figure 7.3 to display its singlet profile. An additional seven vibrational modes are found within +30 cm^{-1} of ν_1, making the ι-nitrogen vibrational spectrum unusually dense for a simple molecular system. The Raman spectrum exhibits only vibrational modes originating from molecular N_2 centres, thus precluding non-molecular nitrogen bonding. The ι-nitrogen crystal-structure (discussed below) contains twelve crystallographically unique N_2 molecules, each of which presumably contributes a unique vibrational band to the Raman spectrum. The bands labelled ν_6 and ν_8 probably consist of overlapping modes because other bands (ν_3 and ν_4) have narrower half-widths by comparison, thus eliminating non-hydrostatic broadening effects. The well-defined lattice modes are very close in frequency and it is therefore more difficult to assign the lattice mode frequencies.

X-ray diffraction — X-ray diffraction data acquired by the author at the P02.2 Extreme Conditions Beamline at PETRA-III confirmed that the ι-nitrogen sample shown in the micrographs in Figure 7.2 contained a single-crystal. High-pressure nitrogen samples are notorious for forming polycrystalline samples which contain only similarly oriented crystallites, thus providing diffraction patterns which are not ideal for either powder or single-crystal analysis. An example of the high-quality diffraction data is shown in Figure 7.4. The data shown in Figure 7.4 were used to determine the unit cell dimensions and the space group by analysis of systematic absences, however an incomplete data set, combined with the low coverage along the one of the crystal axes, prevented attempts at a direct structure solution.

A second data set from the same sample was acquired by Michael Hanfland at the ID15B beamline at the ESRF from which a structural model was refined by Dr Jack Binns as discussed in the following paragraph. The details of the data collection, the data refinement, and the refined structural parameters are given in Appendix A in tables A.1, A.2 and A.3 respectively. A total of 1276 reflections were indexed to a monoclinic lattice with unit-cell dimensions of; a

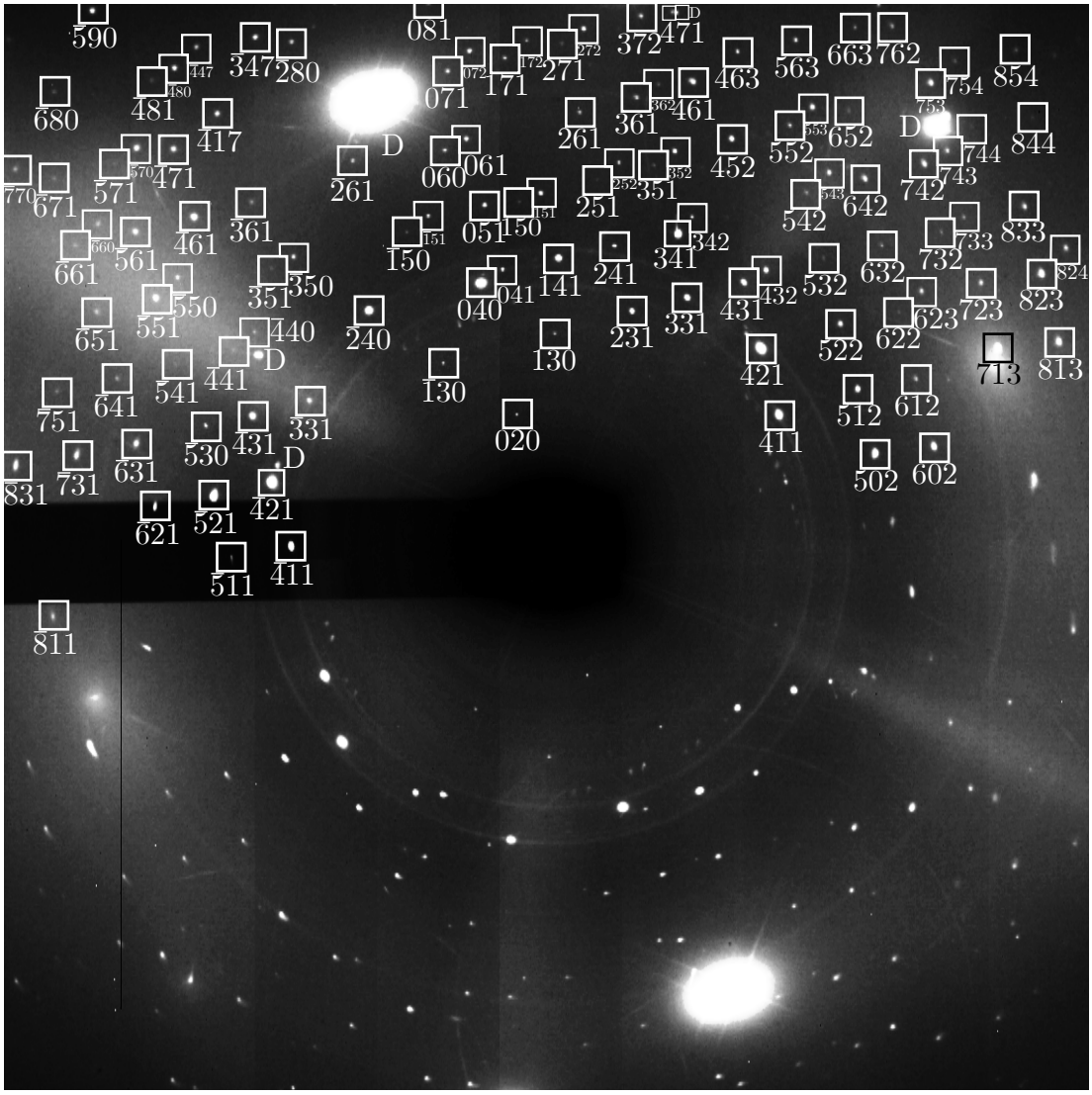

Figure 7.4: Single crystal X-ray diffraction data of ι-nitrogen collected over a 56° rotation in ω. Squares mark nitrogen reflections with the given *hkl* indices. Diamond reflections are labelled with the letter 'D'. Indices are not shown on the lower half of the image plate to clearly display the quality of the raw data.

= 9.899(2), b = 8.863(2), c = 8.726(2) Å, β = 91.64(3)°, V = 765.2(3) Å^3 at 56 GPa. Systematic absence analysis clearly indicated space group $P2_1/c$. (The worked example of the $2_1/c$ screw-axis generating systematic absences given in section 2.2.2 was chosen specifically because it relates directly to the ι-nitrogen crystal structure determined in this chapter.)

The number of atoms per unit-cell was determined by dividing the experimentally determined unit-cell volume (765.2 Å^3) by the volume per atom of ϵ-nitrogen at the same pressure (8 Å^3/ atom) which was taken from the nitrogen equation of state from ref. [Gregoryanz 07], giving a total of 96 atoms (95.7), or 48 molecules, per unit-cell. The number of molecules was consistent with the experimentally determined $P2_1/c$ space group which contains 12 crystallographically unique sites. Projections of the crystal structure are shown in Figure 7.5. Each unit-cell contains 36 molecules which are oriented primarily in the *bc* plane (shown in blue) and which comprise eight layers. The remaining 12 molecules are oriented primarily along the a axis (shown in red).

The structure was solved using the SHELXT software which provides an inital structural model for refinement using dual-space direct methods [Sheldrick 15a]. The refinement of the crystal structure was carried out against $|F^2|$ with the SHELXL refinement package which minimses the difference between the observed and calculated structure factors by least squares refinement [Sheldrick 15b]. The data were integrated to an atomic resolution of 0.6 Å with a low R_{int} = 0.0342 for 641 unique reflections, indicating that all of the atomic sites were included in the model. The N-N bond lengths were all typical for molecular nitrogen, and the e.s.d.s on the bond lengths and atomic positions (given in appendix C) were also low. In geometry optimisation calculations performed in collaboration with Dr Miguel Martinez-Canales (discussed in the next section) the atomic positions converged to positions, on average, less than 0.005 Å away from the experimentally refined positions. The calculated enthalpy of ι-nitrogen was also very competitive and better than that of the ϵ-nitrogen from which it formed above 20 GPa, further increasing confidence in the structure.

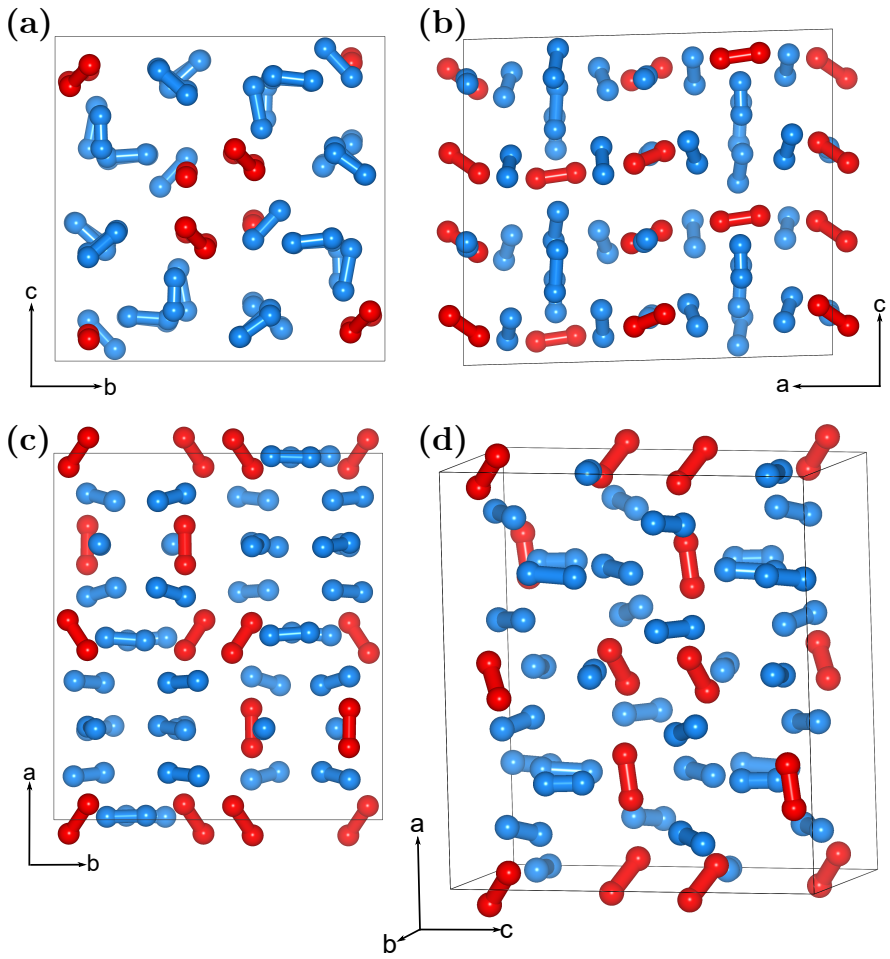

Figure 7.5: Projections of the crystal structure of ι-nitrogen along each of the three axes. (a-c) Projections along the a, b and c axes respectively. (d) A perspective projection of the unit cell. Layered N_2 molecules are shown in blue and oriented molecules are shown in red.

7.4 Discussion

As per the aim of this chapter, this work constitutes the first structural study of ι-nitrogen to determine the crystal structure unambiguously. The inclusion of 48 molecules in the unit cell makes ι-nitrogen the most complex elemental nitrogen structure determined to date and previously proposed structures can be discarded [Katzke 08]. For comparison, the next largest primitive unit-cell belongs to δ^*-nitrogen which contains 16 molecules [Stinton 09]. The ϵ-nitrogen phase, from which ι-nitrogen was formed in this work, contains only eight molecules in its primitive unit cell [Mills 86] which do not exhibit the layering observed in ι-nitrogen.

Thermodynamics — DFT calculations based on the experimentally determined crystal structure were performed in collaboration with Dr Miguel Martinez-Canales to better explore the enthalpy of the structure relative to other known nitrogen phases. The results are shown in Figure 7.6a where the calculated enthalpy is shown relative to the lowest enthalpy predicted structure of ref. [Pickard 2009]. The calculations found that the ι-nitrogen structure has a lower enthalpy than the ϵ-nitrogen from which it is formed above 30 GPa. The single-bonded cubic-gauche (cg) phase quickly becomes the lowest enthalpy structure towards higher pressures as expected. The experimentally determined volume-per-atom for ι-nitrogen at 56 GPa is shown as the red data point in Figure 7.6b. The single data point shows a slight volume decrease on crossing the $\iota \rightarrow \epsilon$-nitrogen transition as anticipated. In future work it would be valuable to extend the range of pressures for which the volume-per-atom has been experimentally determined. Of particular importance would be exploring the behaviour of ι-nitrogen along room-temperature compression.

It is interesting that the synthesis conditions for ι-nitrogen are intermediate between those of the room-temperature molecular phases and the high-temperature non-molecular phases. Although the nitrogen remains molecular in ι-nitrogen, ac-

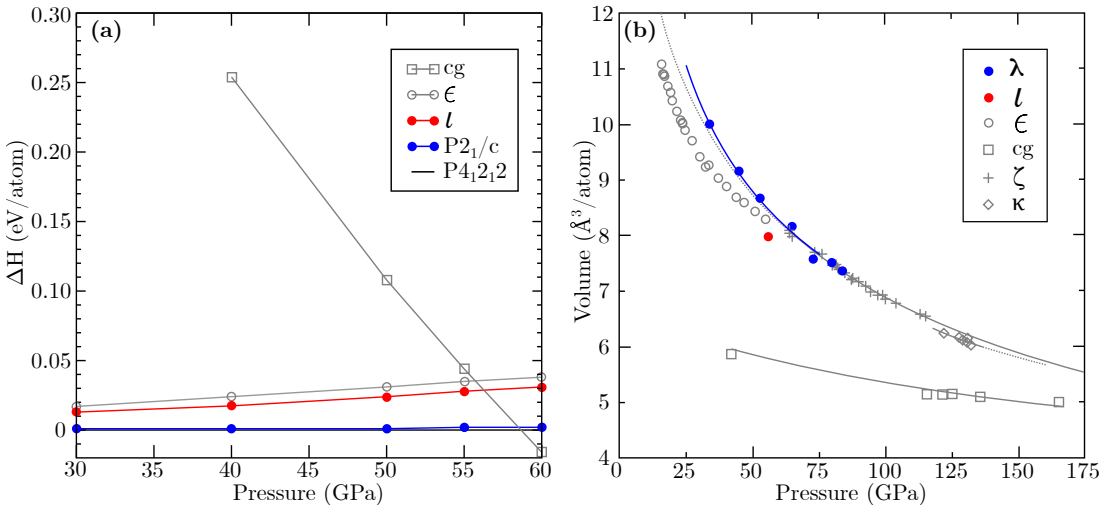

Figure 7.6: a) Calculated enthalpies of various phases of nitrogen plotted as a function of pressure and with pressure with respect to the $P4_12_12$ structure of ref. [Pickard 2009]. **b)** Pressure-volume relations for various nitrogen phases reproduced and modified from ref. [Gregoryanz 07]. The λ-nitrogen data are taken from ref. [Frost 16].

cording to both the Raman spectra and the bonding distances from XRD, the structure may demonstrate an intermediate step in the pressure-induced evolution of bonding because the alignment of one in every four molecules perpendicular to the molecular planes is reminiscent of the tetrahedral molecular geometry of sp^3-hybridised systems like *cg*-nitrogen. ι-nitrogen might therefore be considered an intermediate structure between the low enthalpy molecular phases (such as λ-nitrogen) and the polymeric phases (such as *cg*-nitrogen).

The θ and λ-nitrogen phases — The layering observed in ι-nitrogen is similar to that observed in the proposed structure for λ-nitrogen. λ-nitrogen a molecular phase which can only be accessed by low-temperature compression from ambient pressure to above 31 GPa [Frost 16]. The interlayer spacing in ι-nitrogen varies between 1.172 and 1.264 Å at 56 GPa depending on the molecular orientation. The interlayer spacing in λ-nitrogen is 1.162 Å at 40 GPa. λ-nitrogen is believed to have a $P2_1/c$ structure based on cross-reference of the experimentally determined UCDs from powder XRD data [Frost 16] with those predicted by DFT calculations in ref. [Pickard 2009]. Accordingly, the unit cell contains only a single N_2 molecule, however, Raman spectra of λ-nitrogen exhibit three

vibrational modes, suggesting at least three distinct N_2 sites. For this reason the predicted $P2_1/c$ structure of ref. [Pickard 2009] and the λ-nitrogen volume-per-atom data of ref. [Frost 16] are labelled accordingly in Figure 7.6. If the structure of λ-nitrogen is indeed the layered $P2_1/c$ structure as proposed, it may be closely related to ι-nitrogen which is intriguing considering their quite disparate synthesis conditions.

The Raman spectra of λ-nitrogen are similar to the spectra of θ-nitrogen (as discussed in ref. [Frost 16]) which is the only high-temperature molecular phase other than ι-nitrogen. The structure of θ-nitrogen remains unknown with only a tentative indexing of an orthorhombic structure based on powder XRD data [Gregoryanz 02]. The θ, ι and λ-nitrogen phases may constitute a family of phases distinct from those exhibited along the traditional room-temperature isothermal-compression-line. The distinguishing characteristics of the θ, ι and λ-nitrogen phases are: 1) They are sensitive to the P-T path taken to the P-T conditions of their formation and they cannot be accessed at room-temperature. 2) They can be *recovered* to room-temperature once formed, and each of them back-transforms to ϵ-nitrogen on room-temperature decompression: ι-nitrogen at 23 GPa, θ-nitrogen at 30 GPa, and, λ-nitrogen at 32 GPa. Subsequent compression alone is not sufficient to recover any of the phases. 3) They have stability regions which overlap with each-other and with large areas of the classical nitrogen phase-diagram. Figure 7.7 displays data collated from the literature to illustrate the stability regions of the phases once formed. The λ-nitrogen stability region is taken from ref. [Frost 16], but the stability regions of ι and θ-nitrogen have not previously been illustrated in this way. ι and θ-nitrogen are often omitted from phase-diagrams entirely and these figures aim to reinforce the complicated P-T dependence of the phases exhibited by nitrogen at extreme conditions by making clear the extent to which different phases overlap. A clear direction for future work would be to conduct structural studies on the θ and λ-nitrogen phases if single crystals can be synthesised. In principle the exact methodology of the contributing work could be followed to produce sample of θ-nitrogen suitable for

single-crystal XRD analysis.

The elusiveness of ι-nitrogen — Finally, the experimental observation of a slow phase-transition may illuminate the discrepancies in the literature regarding the (ir)reproducibility of the P-T conditions necessary to access ι-nitrogen. As observed in this work, the transition from ϵ to ι-nitrogen occurred over minute-long time scales whilst the sample was held under the steady state P-T conditions made possible by resistive-heating methods. The transition therefore is probably characterised by a kinetic barrier which is overcome by the heat which was continually supplied to the sample. Laser-heating techniques, as used in studies which failed to access ι-nitrogen [Tomasino 14b], are not suitable for inducing well-characterised temperatures for long periods of time because the transient peak temperatures decay quickly due to the high-thermal conductivity of the diamond anvils. Laser-heating also induces very intense but localised heating, which can cause large thermal gradients and can induce phase-mixtures. The kinetically controlled phase-boundary indicated by the slow transition at steady-state P-T may be due to the substantial molecular rearrangement which occurs when the sample transitions from the un-layered ϵ-phase to the layered ι-phase. A large kinetic barrier might explain why ι-nitrogen was not been observed in the recent work on the melting-curve of nitrogen [Weck 2017] where, in order to enter the high-pressure fluid-state, the P-T conditions of the sample passed through those required to synthesise ι-nitrogen. The barrier to the formation of ι-nitrogen effectively 'locks-in' the phase once formed such that it can be recovered to room-temperature conditions without back-transforming to ϵ-nitrogen. ι-nitrogen has previously been recovered down to 23 GPa at room-temperature and down to 30 GPa at 10 K [Gregoryanz 02] as shown in Figure 7.7a.

Conclusion — The contributing work of this chapter constitutes the first structural study of ι-nitrogen to determine the crystal structure unambiguously, as per the original aim. The ι-nitrogen structure is the most complex elemental nitrogen structure determined to date, and the subsequent calculations based on the experimentally determined structure show that complex structures may

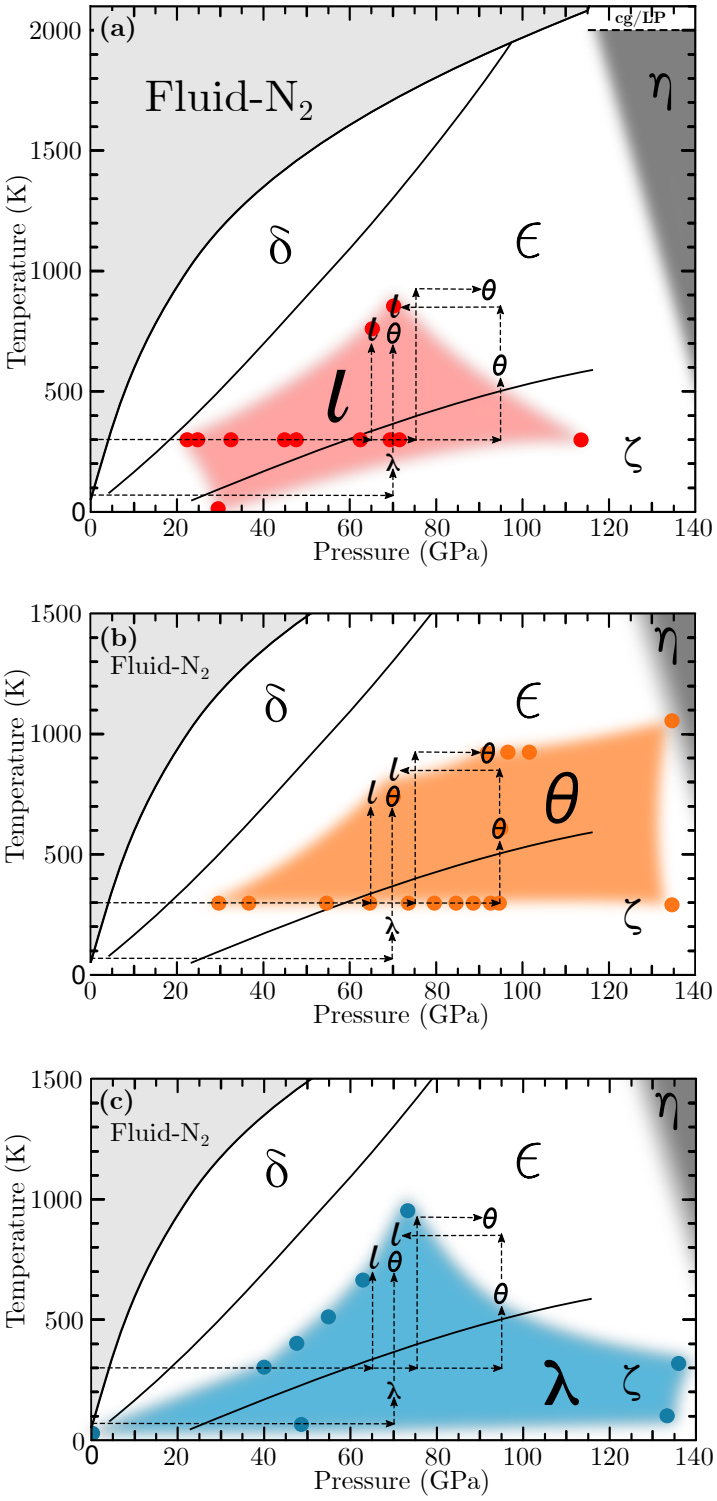

Figure 7.7: Nitrogen phase-diagrams overlayed with the experimentally observed stability regions of (a) ι-nitrogen (b) θ-nitrogen and (c) λ-nitrogen, once the phases have been formed. The data points are taken from: ref. [Goncharov 08, Gregoryanz 02] for ι-nitrogen, refs. [Gregoryanz 02, Tomasino 14a] for θ-nitrogen, and, ref. [Frost 16] for λ-nitrogen.

become favourable in molecular systems at extreme conditions. Why such a complex *molecular* crystal might be more favourable than a simpler one remains the subject of future investigation.

Traditionally it was expected that increasing pressure would result in structures with more efficient geometrical packing. Several metallic elements have been observed to transition from fcc (packing efficiency ∼0.74) to bcc (∼0.68) with increasing pressure, which corresponds to a decrease in atomic coordination from 12 to 8. The transitions to less efficient packing structures in the transition and heavy alkali metals have been rationalised in terms of increasing d-orbital occupancy with increasing pressure. The d-orbital bands in these metallic systems lie close in energy to the sp-valence bands, and increased d-band occupation leads to an increased favourability of open structures [Errandonea 02, Skriver 85]. An extreme example of increasing structural complexity with pressure is a barium structure with *768 atoms in the representative unit* at 19 GPa [Loa 12].

In the lighter metals similar observations have been attributed to an increase in the p-orbital occupancy, and sodium, for example, has been observed to transition to a structure with *512 atoms in the unit cell* at 118 GPa just above ambient-temperature [Gregoryanz 08]. The mechanism of s-p or s-d electronic transfer favouring open structures in metals is not directly applicable in the case of ι-nitrogen because it is probably insulating. (Although no direct electron transport properties were measured in the contributing work the ι-nitrogen sample remained transparent to visible light.) s-p electronic transfer may increase structural favourability by other mechanisms however. As aforemetioned, the alignment of one in every four molecules perpendicular to the molecular planes in ι-nitrogen is reminiscent of the tetrahedral molecular geometry of sp^3-hybridised systems, such as the single-bonded cubic-gauche nitrogen. A comparison of the two structures is shown below in Figure 7.8. It is already known therefore that at extreme pressures nitrogen undergoes sp^3-hybridisation, so a hypothesis for the favourable complexity of the ι-nitrogen structure might be that the degree of sp-mixing is much lower than in cubic-gauche nitrogen, but still sufficient to

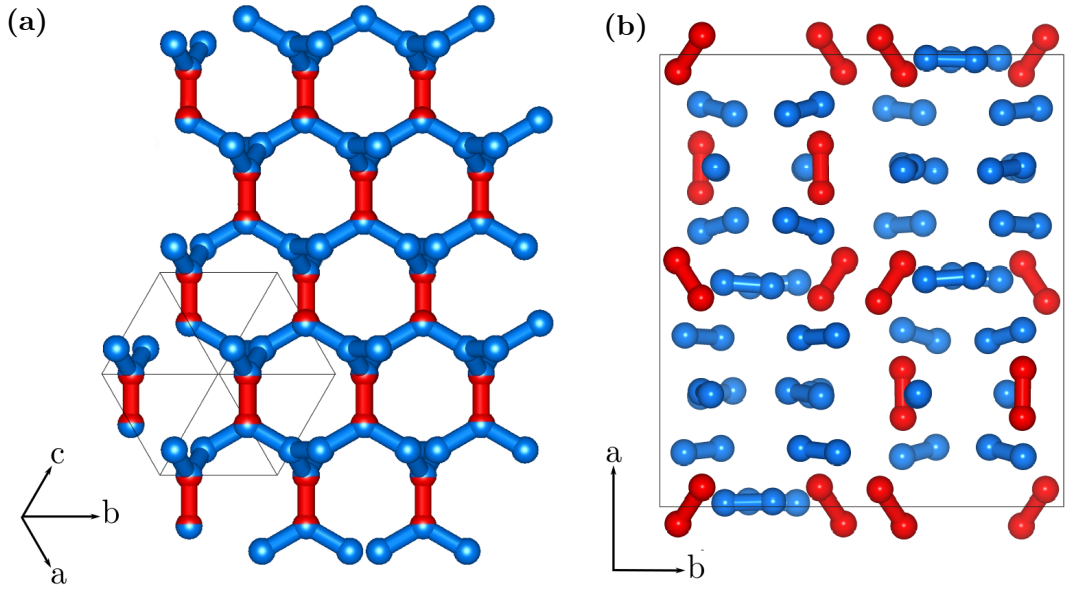

Figure 7.8: The structures of cg-nitrogen (a) and ι-nitrogen (b). Layered molecules are shown in blue and those (roughly) perpendicular are shown in red.

allow a slight overlap of *sp*-bonding orbitals.

Chapter 8

Conclusions

The three experimental chapters of the contributing work are discussed below with an emphasis on the main findings and future work.

Nitrogen–Xenon — The investigation into the binary nitrogen–xenon system at high-pressure was successful and resulted in a publication. Prior to this work, the experimental studies on the xenon-nitrogen system presented no structural data and were limited to low pressures. This work therefore constitutes the first comprehensive set of experiments, finding a new $Xe(N_2)_2$ van der Waals compound which undergoes a phase-transition characterised by an increase in molecular-nitrogen rotational ordering at 14 GPa.

Interestingly, the molecular nitrogen in the $Xe(N_2)_2$ compound was observed up to the maximum pressure studied of 180 GPa, surpassing the non-molecular limit in pure nitrogen. Laser-heating to 3000 K was conducted at this maximum pressure, however no chemical reaction could be stimulated even at such extreme-conditions, and no changes were observed in the XRD patterns or Raman spectra.

In terms of future work it would be interesting to perform direct measurements of electrical transport properties of the $Xe(N_2)_2$ compound. Whilst the optical measurements made in the contributing work are not sufficient to make

any definitive claims about metallisation, visual observations of the xenon-rich sample containing $Xe(N_2)_2$-II becoming opaque and reflective by 120 GPa might suggest a reduced metallisation pressure compared to pure xenon. It is known that doping the high-pressure xenon system with small amounts of oxygen can drastically reduce the metallisation pressure at ambient-temperature from 130 GPa to 49 GPa [Dewaele 12] and it would be interesting to make a comparison by doping xenon with nitrogen, the diatomic next to oxygen in the periodic table.

Nitrogen–Hydrogen — The investigation detailed exploratory work into the behaviour of nitrogen-hydrogen mixtures as a function of both composition and pressure. Powder XRD experiments revealed mixed phases of known nitrogen-hydrogen solids consistent with those reported in the literature which was contemporary with the beginning of this project.

The first megabar study of the nitrogen-hydrogen system was performed in which the two species were not mutually soluble. The results are possibly the most intriguing of this particular investigation. At the maximum pressure studied of 242 GPa the sample of 75 mol% H_2 composition remained transparent yet Raman inactive, differentiating itself from either of its pure constituents under the same conditions. The Raman activity remained unchanged on decompression to low pressures, suggesting that the high-pressure structure may be recoverable to moderate pressures, however the megabar experiment was only attempted once and should be repeated.

The recovery of hydrazine on room-temperature decompression of nitrogen-hydrogen mixtures has been widely reported, however in order to better explore the extreme conditions within ice-giant planets it would be necessary to investigate the combined effect of elevated-temperatures. The recovery of ammonia rather than hydrazine on decompression after high-temperature conditions observed in the contributing work has not been reported in the current literature and may represent the highest pressure experimental demonstration of the Haber–Bosch process. Whether ammonia or hydrazine (or a different hydronitrogen

compound) is the preferred molecular state at extreme conditions is yet to be determined.

The new findings of the mega-bar and high-temperature Raman experiments show that there remain unanswered questions about the behaviour of the nitrogen-hydrogen system at extreme conditions. In terms of future work, there is a gap in the experimental literature regrading the exploration of the nitrogen-hydrogen system at megabar pressures and it would be interesting to repeat megabar Raman experiments to test the reproducibility of forming the transparent Raman inactive solid. It would also be interesting to explore the effect of simultaneous high-temperature megabar conditions, both of which were explored separately in the contributing work.

ι-Nitrogen — The investigation into ι-nitrogen has been a resounding success. As per the original aim of the investigation, the work constitutes the first structural study of ι-nitrogen to determine the crystal structure. The inclusion of 48 molecules in the unit cell makes ι-nitrogen the most complex elemental nitrogen structure determined to date and previously proposed structures can now be discarded.

The work emphasises the relevance of the high-temperature phases ι and θ-nitrogen which have previously been rather overlooked on the nitrogen phase-diagram which tends to focus on the ϵ-nitrogen family of phases. The layering observed in ι-nitrogen is similar to that observed in the proposed structure for λ-nitrogen. The two phases might be closely related in terms of structure which is intriguing considering their quite disparate synthesis conditions, λ-nitrogen only being accessible at cryogenic temperatures.

The experimental work illuminates the elusiveness of ι-nitrogen, which has reportedly been challenging to access. The discrepancies in the literature regarding the (ir)reproducibility of the P-T conditions necessary to access ι-nitrogen may be explained by the kinetic boundary to ι-nitrogen's formation, which requires well-

characterised steady-state elevated-temperatures which are not generally possible with laser-heating methods.

This work has spawned three clear directions for possible future studies:

1. In principle the exact methodology of the contributing work could be followed to produce sample of θ-nitrogen suitable for single-crystal XRD analysis. θ-nitrogen can be synthesised at slightly higher pressures but lower temperatures than ι-nitrogen and its structure remains undetermined.

2. The traditional melting-curve shown on the nitrogen phase-diagram is that of δ and ϵ-nitrogen. The DFT calculations found that the ι-nitrogen structure has a lower enthalpy than the ϵ-nitrogen above 30 GPa, so it would be interesting to explore how the thermodynamics of the new structure affect the melting characteristics.

3. Why such a complex molecular crystal might be more favourable than a simpler one remains unclear. Similar observations have been made in elemental systems which are metallic or semi-metallic under ambient conditions, but it is unusual to find such a complex molecular crystal consisting of simple diatomic units.

Appendix A

Supplementary Crystallographic Data for Chapter 5: Nitrogen-Xenon

	Phase I	Phase II
Crystal data		
Chemical formula	$Xe(N_2)_2$	$Xe(N_2)_2$
M_r	243.3	243.3
Crystal system, space group	Cubic, $Fd\bar{3}m$	Tetragonal, $I4_1/amd$
Pressure (GPa)	5.6	18.7
a (Å)	9.2361 (3)	5.7228 (3)
c (Å)	9.2361 (3)	9.2134 (10)
V (Å^3)	787.88 (5)	301.74 (4)
Radiation type	Synchrotron ($\lambda = 0.4872$ Å)	Synchrotron ($\lambda = 0.4872$ Å)
Data collection		
2θ values (°)	$2\theta_{min} = 3.416$, $2\theta_{max} = 33.451$, $2\theta_{step} = 0.011$	$2\theta_{min} = 3.724$, $2\theta_{max} = 24.979$, $2\theta_{step} = 0.011$
Refinement		
R factors and goodness of fit	$R_p = 0.009$, $R_{wp} = 0.019$, $R_{exp} = 0.018$, $R(F) = 0.082$, $\chi^2 = 1.103$	$R_p = 0.015$, $R_{wp} = 0.021$, $R_{exp} = 0.018$, $R(F) = 0.094$, $\chi^2 = 1.369$
No. of parameters	8	17

Table A.1: Crystal structure data, experiment and refinement details for $Xe(N_2)_2$ phases I and II. Taken from the Supplementary Material of ref [Howie 16a] which is included in the Publications section at the end of the end of this Thesis. The R factors and goodness of fit are discussed in ref. [Toby 06].

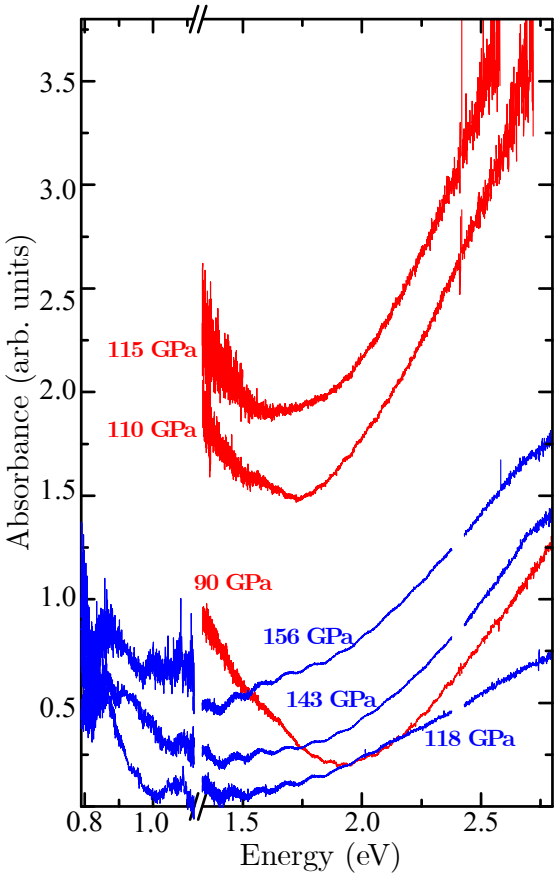

Figure A.1: Absorbance spectra for $Xe(N_2)_2$-II in an excess of xenon (red) and in an excess of nitrogen (blue). The higher absorbance of $Xe(N_2)_2$-II in an excess of xenon shows that the sample is less transparent over this energy region and may indicate the earlier onset of metallic behaviour. Electrical transport measurements would be required to confirm such a hypothesis.

Atom	x	y	z	Occupancy
Xe001	0.0000	0.0000	0.0000	1 Xe atom
Xe002	0.0000	0.0000	1.0000	1 Xe atom
Xe003	0.0000	1.0000	0.0000	1 Xe atom
Xe004	0.0000	1.0000	1.0000	1 Xe atom
Xe005	1.0000	0.0000	0.0000	1 Xe atom
Xe006	1.0000	0.0000	1.0000	1 Xe atom
Xe007	1.0000	1.0000	0.0000	1 Xe atom
Xe008	1.0000	1.0000	1.0000	1 Xe atom
Xe009	0.0000	0.5000	0.5000	1 Xe atom
Xe010	1.0000	0.5000	0.5000	1 Xe atom
Xe011	0.5000	0.5000	0.0000	1 Xe atom
Xe012	0.5000	0.5000	1.0000	1 Xe atom
Xe013	0.5000	0.0000	0.5000	1 Xe atom
Xe014	0.5000	1.0000	0.5000	1 Xe atom
Xe015	0.7500	0.2500	0.7500	1 Xe atom
Xe016	0.2500	0.2500	0.2500	1 Xe atom
Xe017	0.2500	0.7500	0.7500	1 Xe atom
Xe018	0.7500	0.7500	0.2500	1 Xe atom
N001	0.6250	0.1250	0.1250	2 N atom
N002	0.3750	0.3750	0.6250	2 N atom
N003	0.8750	0.6250	0.8750	2 N atom
N004	0.1250	0.8750	0.3750	2 N atom
N005	0.1250	0.6250	0.1250	2 N atom
N006	0.6250	0.3750	0.3750	2 N atom
N007	0.8750	0.8750	0.6250	2 N atom
N008	0.3750	0.1250	0.8750	2 N atom
N009	0.1250	0.1250	0.6250	2 N atom
N010	0.3750	0.6250	0.3750	2 N atom
N011	0.6250	0.8750	0.8750	2 N atom
N012	0.8750	0.3750	0.1250	2 N atom
N013	0.1250	0.3750	0.8750	2 N atom
N014	0.8750	0.1250	0.3750	2 N atom
N015	0.3750	0.8750	0.1250	2 N atom
N016	0.6250	0.6250	0.6250	2 N atom

Table A.2: Atomic coordinates for $Xe(N_2)_2$-I at 5.6 GPa which can be used as a starting model in future refinements.

Atom	x	y	z
Xe001	0.0000	0.0000	0.0000
Xe002	0.0000	0.0000	1.0000
Xe003	0.0000	1.0000	0.0000
Xe004	0.0000	1.0000	1.0000
Xe005	1.0000	0.0000	0.0000
Xe006	1.0000	0.0000	1.0000
Xe007	1.0000	1.0000	0.0000
Xe008	1.0000	1.0000	1.0000
Xe009	0.5000	0.5000	0.5000
Xe010	0.0000	0.5000	0.2500
Xe011	1.0000	0.5000	0.2500
Xe012	0.5000	0.0000	0.7500
Xe013	0.5000	1.0000	0.7500
N001	0.5000	0.2820	0.0461
N002	0.0000	0.2180	0.5461
N003	1.0000	0.2180	0.5461
N004	0.7180	0.0000	0.2961
N005	0.7180	1.0000	0.2961
N006	0.7820	0.5000	0.7961
N007	0.0000	0.2820	0.7039
N008	1.0000	0.2820	0.7039
N009	0.5000	0.2180	0.2039
N010	0.7820	0.0000	0.4539
N011	0.7820	1.0000	0.4539
N012	0.7180	0.5000	0.9539
N013	0.2820	0.5000	0.9539
N014	0.2180	0.0000	0.4539
N015	0.2180	1.0000	0.4539
N016	0.2180	0.5000	0.7961
N017	0.2820	0.0000	0.2961
N018	0.2820	1.0000	0.2961
N019	0.0000	0.7820	0.5461
N020	1.0000	0.7820	0.5461
N021	0.5000	0.7180	0.0461
N022	0.5000	0.7820	0.2039
N023	0.0000	0.7180	0.7039
N024	1.0000	0.7180	0.7039

Table A.3: Atomic coordinates for $Xe(N_2)_2$-II at 18.7 GPa which can be used as a starting model in future refinements.

Appendix B

Supplementary Raman spectra for all studied nitrogen–hydrogen composition:

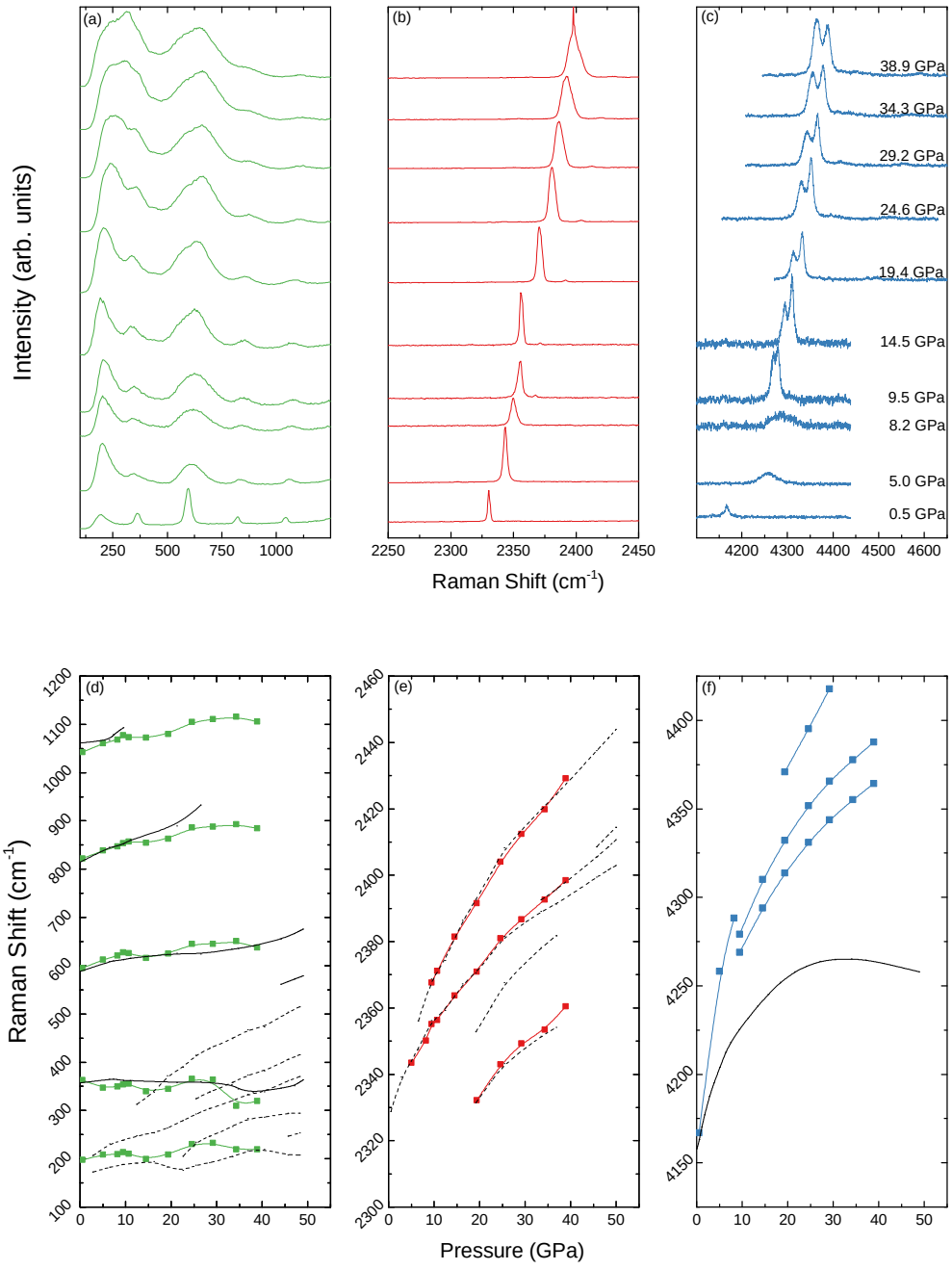

Figure B.1: Raman spectra (top) and corresponding frequency *vs.* pressure plots (bottom) for 16 mol% H_2 hydrogen-nitrogen. **(a)** and **(d)** in green show the low-frequency region of interest. **(b)** and **(e)** in red show the pure nitrogen vibrational mode region of interest. **(c)** and **(f)** in blue show the pure hydrogen vibrational mode region of interest. Pure hydrogen is shown with solid black lines. Pure nitrogen is shown with dashed black lines.

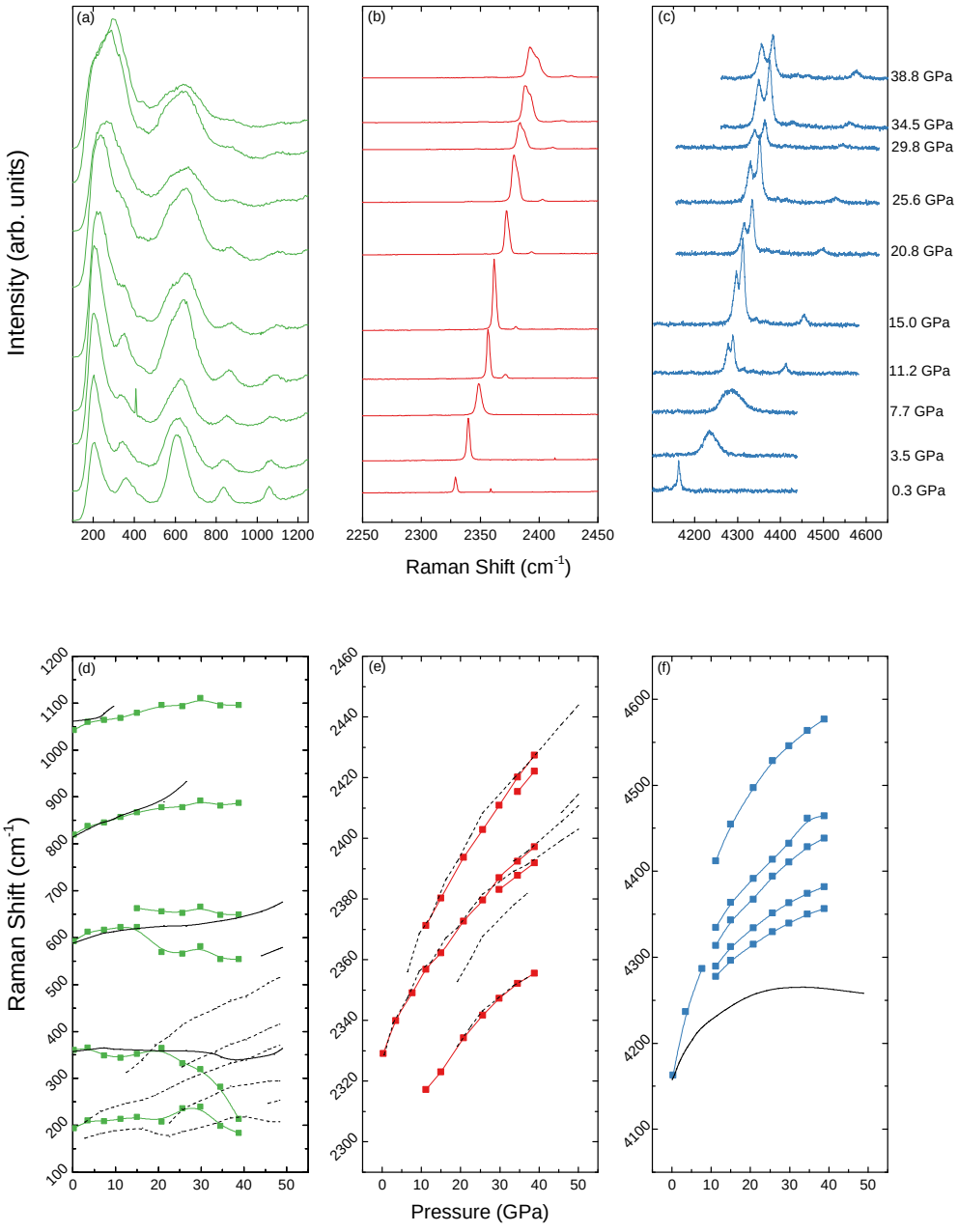

Figure B.2: Raman spectra (top) and corresponding frequency *vs.* pressure plots (bottom) for **28 mol**% $\mathbf{H_2}$ hydrogen-nitrogen.

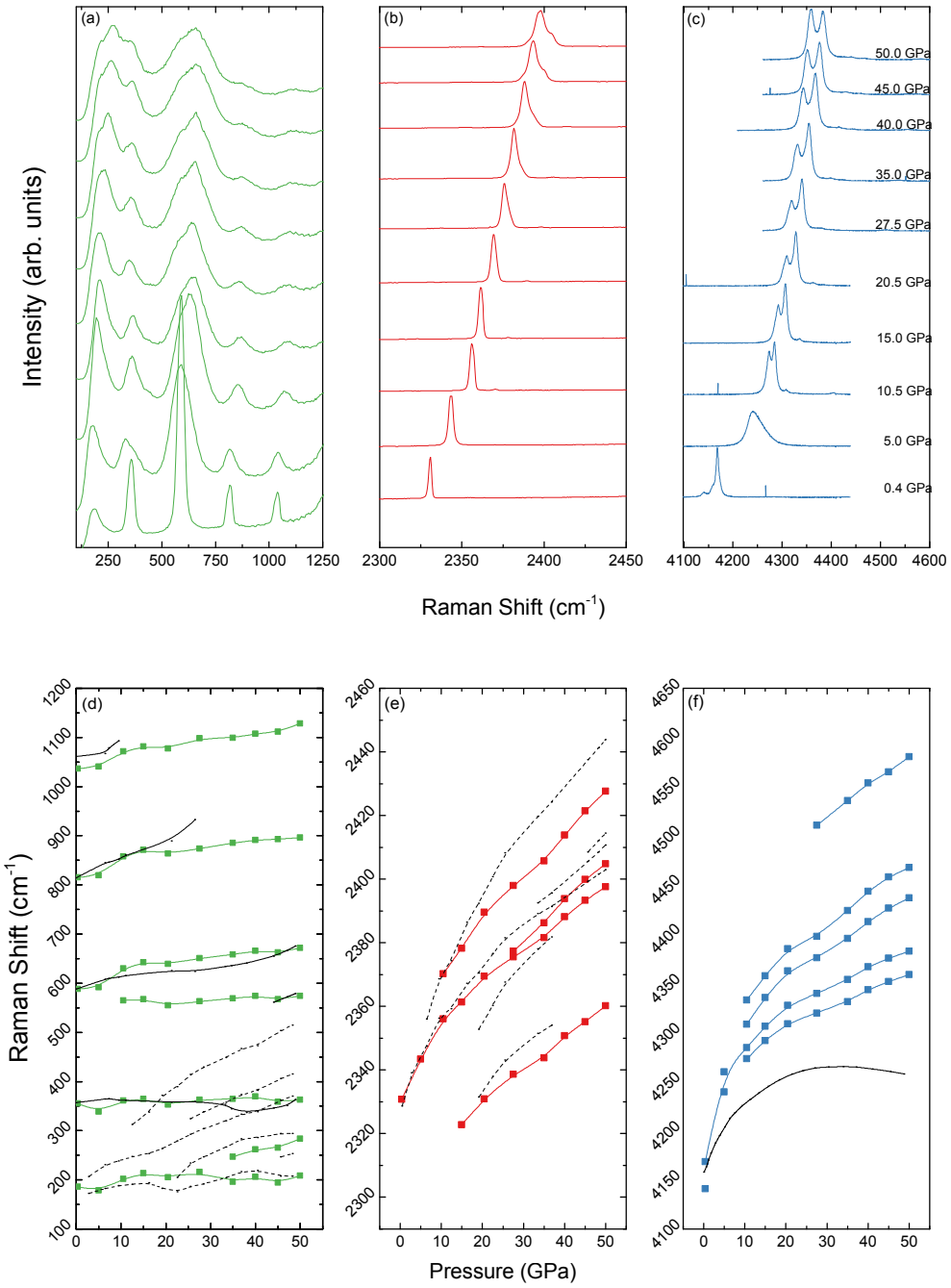

Figure B.3: Raman spectra (top) and corresponding frequency *vs.* pressure plots (bottom) for **43 mol**% $\mathbf{H_2}$ hydrogen-nitrogen.

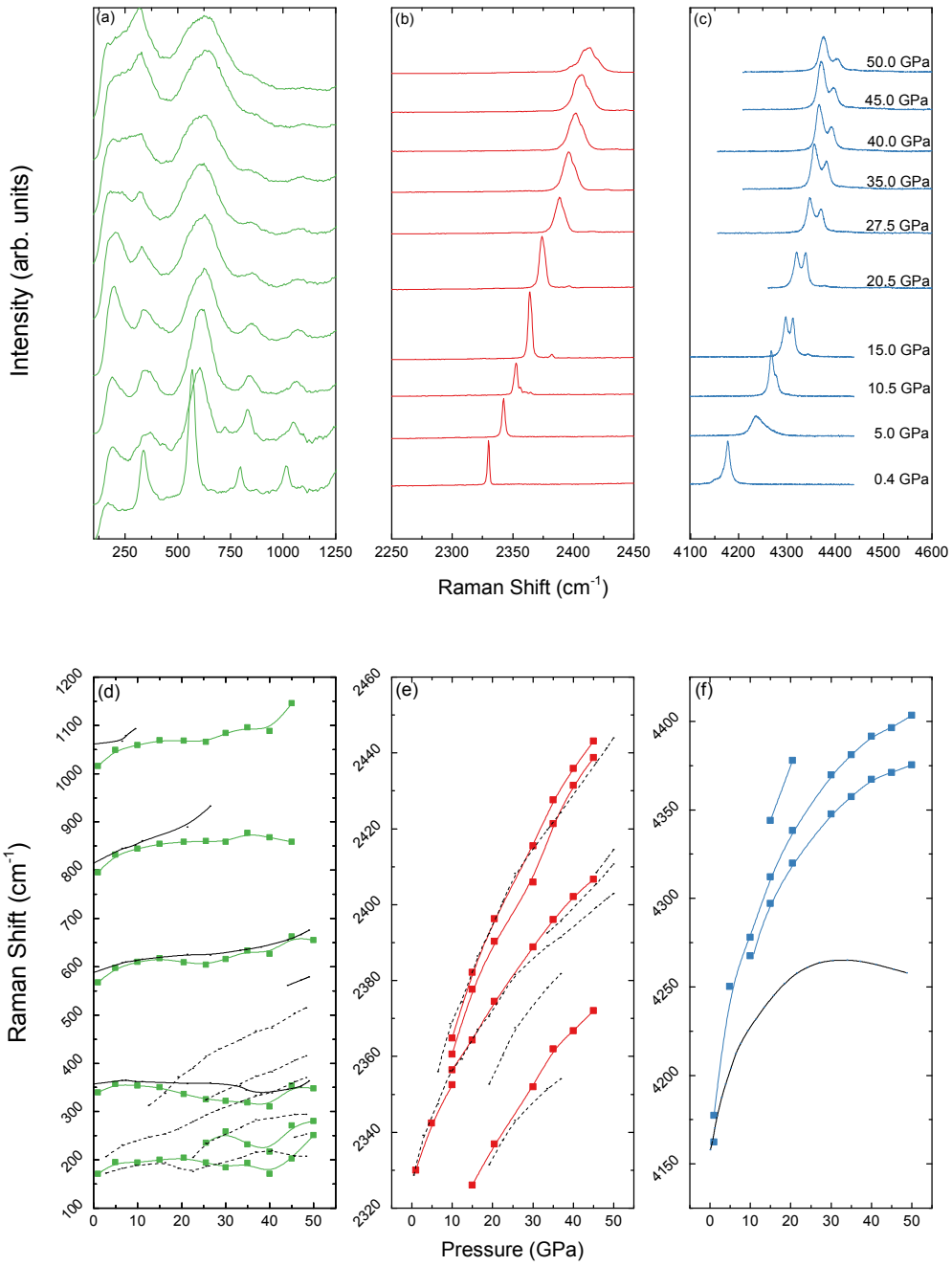

Figure B.4: Raman spectra (top) and corresponding frequency *vs.* pressure plots (bottom) for **50 mol%** $\mathbf{H_2}$ hydrogen-nitrogen.

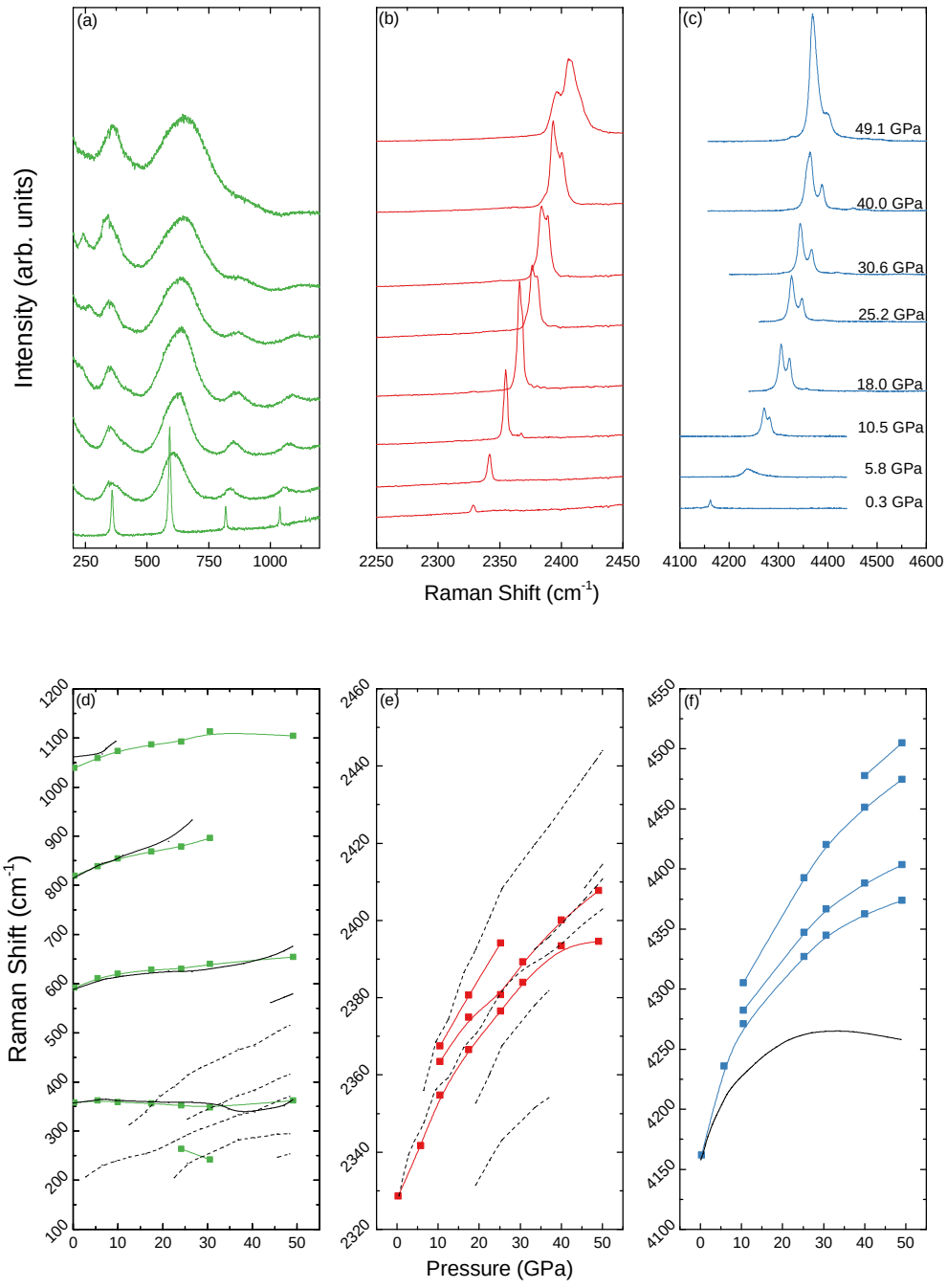

Figure B.5: Raman spectra (top) and corresponding frequency *vs.* pressure plots (bottom) for **59 mol**% $\mathbf{H_2}$ hydrogen-nitrogen.

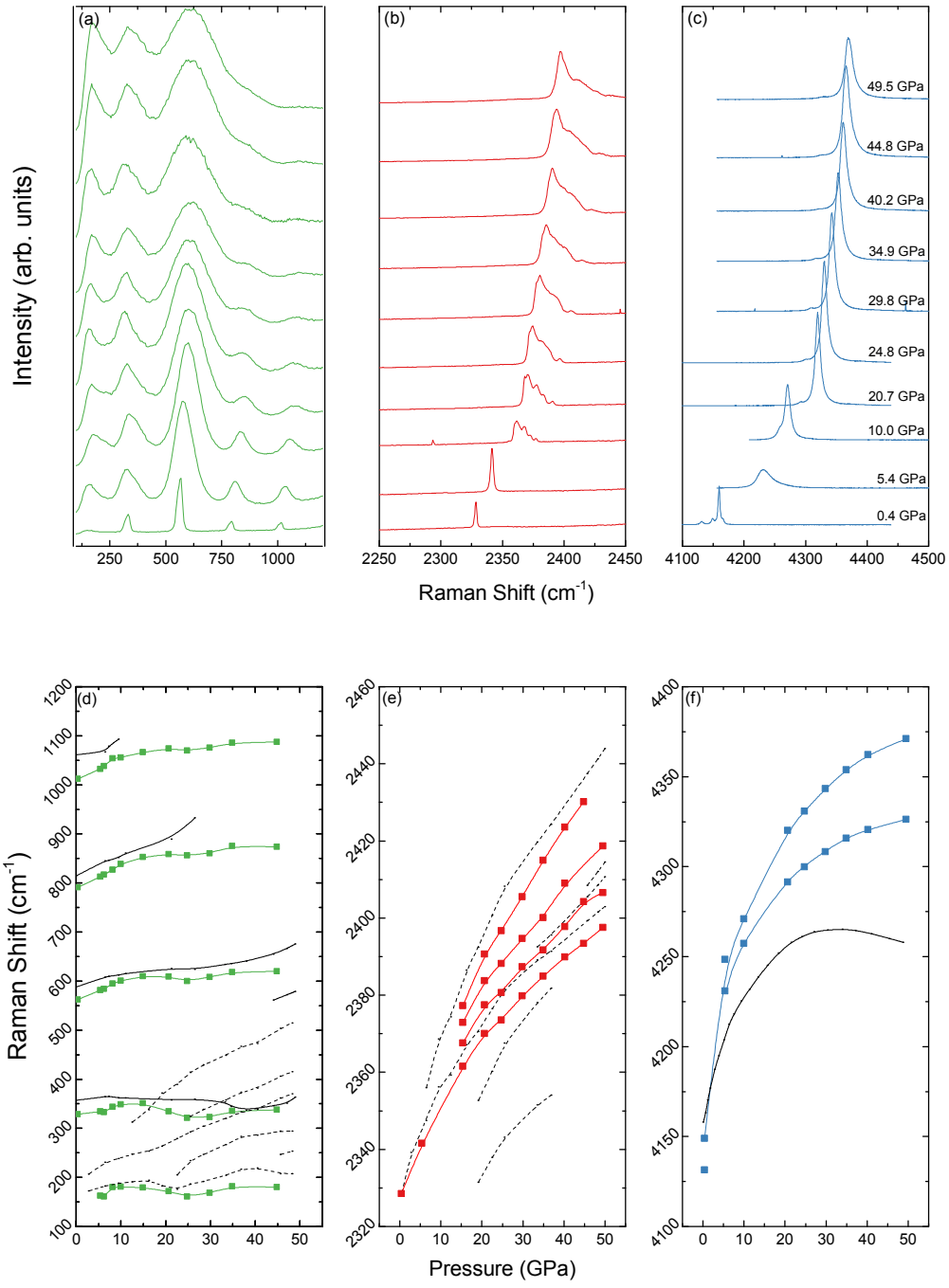

Figure B.6: Raman spectra (top) and corresponding frequency *vs.* pressure plots (bottom) for **66 mol**% $\mathbf{H_2}$ hydrogen-nitrogen.

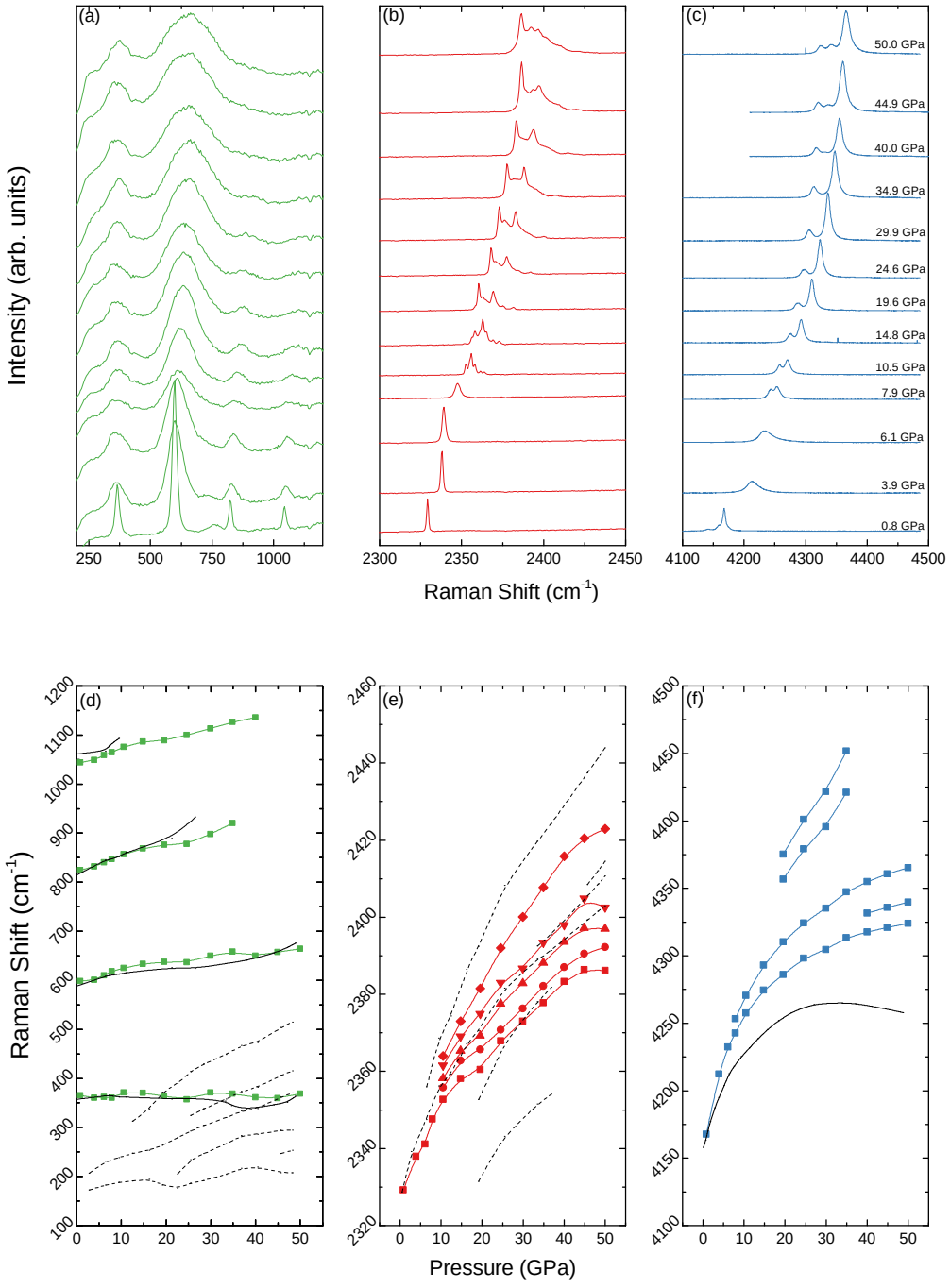

Figure B.7: Raman spectra (top) and corresponding frequency *vs.* pressure plots (bottom) for **75 mol**% $\mathbf{H_2}$ hydrogen-nitrogen.

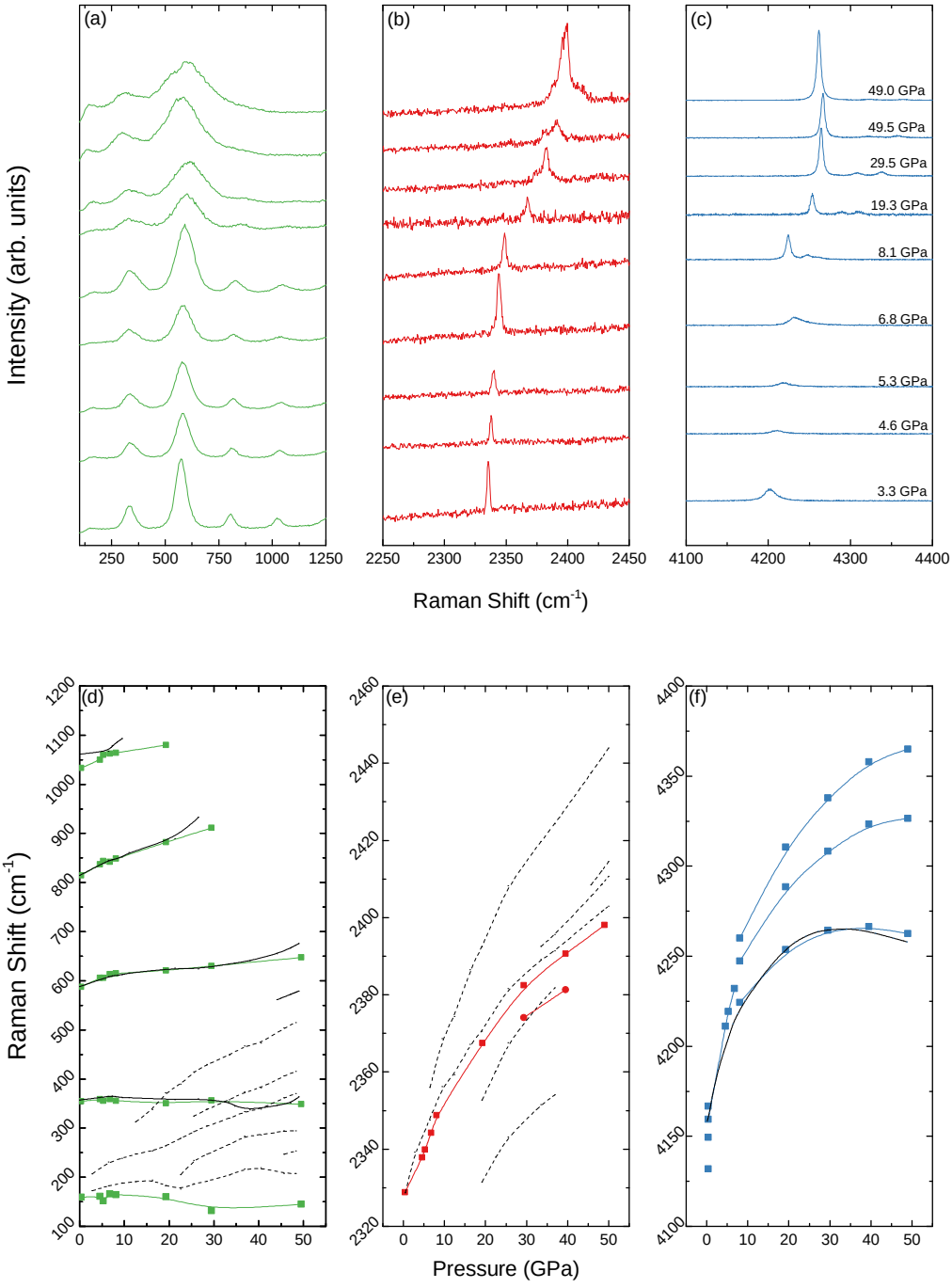

Figure B.8: Raman spectra (top) and corresponding frequency *vs.* pressure plots (bottom) for **83 mol**% $\mathbf{H_2}$ hydrogen-nitrogen.

Appendix C

Supplementary crystallographic data for Chapter 7:

ι-nitrogen:

Crystal data	
Space group	$P2_1/c$
a (Å)	9.899(2)
b (Å)	8.863(2)
c (Å)	8.726(2)
β (°)	91.64(3)
V (Å^3)	765.2(3)
Data collection	
Number of measured reflections	1276
Number of unique reflections	641
Number of observed reflections [$\lvert F_{obs}\rvert > 2\sigma$]	390
R_{int}	0.034
Refinement	
$R[F^2 > 2\sigma(F^2)]$	0.123
Number of parameters	97
Number of restraints	12
$\Delta\rho_{max}$, $\Delta\rho_{min}$ (e Å^{-3})	0.53, −0.40

Table C.1: Data collection and refinement details for ι-nitrogen at 56 GPa. Restraints were necessary because the data-to-parameter ratio was low. In the absence of these restrains the thermal displacement parameters for bonded atoms can be very different. The applied restraints used here were 'rigid bond restraints' which state that *the mean-square displacements of two atoms are equal in the direction of the bond joining them* [Thorn 12]. This is a reasonable restraint because ι-nitrogen contains only molecular nitrogen (as seen in the Raman spectra) which is characterised by a very stiff triple covalent bond. There are 12 restraints, corresponding the 12 nitrogen molecules in the asymmetric unit.

Atom	x	y	z	U_{eq} (Å^2)
N001	-0.0386(9)	0.4541(8)	0.348(3)	0.0353(19)
N002	0.0434(9)	0.3957(8)	0.411(2)	0.0342(19)
N003	0.0115(8)	0.2800(8)	0.637(3)	0.037(2)
N004	0.0083(10)	0.1605(8)	0.623(3)	0.039(2)
N005	0.1187(9)	0.4412(8)	0.929(3)	0.0357(19)
N006	0.1296(9)	0.3479(7)	0.855(3)	0.0318(17)
N007	0.2448(8)	0.3988(8)	0.626(2)	0.034(2)
N008	0.2571(8)	0.3182(8)	0.534(2)	0.0331(18)
N009	0.3740(9)	0.3475(8)	0.840(2)	0.0337(18)
N010	0.3792(9)	0.4375(9)	0.923(3)	0.039(2)
N011	0.4976(10)	0.1571(8)	0.629(3)	0.0343(19)
N012	0.4892(9)	0.2764(9)	0.637(3)	0.039(2)
N013	0.4619(9)	0.1020(8)	0.900(3)	0.0356(19)
N014	0.5459(9)	0.0412(8)	0.855(3)	0.0346(19)
N015	0.6097(10)	0.3990(8)	0.826(3)	0.0351(19)
N016	0.6322(9)	0.3117(8)	0.905(2)	0.0349(19)
N017	0.7468(8)	0.6022(8)	0.841(2)	0.031(2)
N018	0.7516(8)	0.6256(8)	0.717(2)	0.031(2)
N019	0.6972(9)	0.3998(7)	0.580(3)	0.0341(19)
N020	0.8035(9)	0.3975(8)	0.565(3)	0.038(2)
N021	0.8900(8)	0.3998(7)	0.819(2)	0.0266(17)
N022	0.8682(8)	0.3149(8)	0.900(2)	0.0321(18)
N023	0.7475(9)	0.1378(9)	0.767(2)	0.033(2)
N024	0.7539(8)	0.1402(8)	0.645(2)	0.0267(19)

Table C.2: Final Coordinates and Equivalent Isotropic Displacement Parameters for ι-N_2 at 56 GPa.

N001-N002	1.097(19)	N013-N014	1.075(18)
N003-N004	1.067(11)	N015-N016	1.06(2)
N005-N006	1.06(2)	N017-N018	1.10(2)
N007-N008	1.084(19)	N019-N020	1.064(13)
N009-N010	1.08(2)	N021-N022	1.059(18)
N011-N012	1.063(11)	N023-N024	1.07(2)

Table C.3: Bond Distances for ι-N_2 at 56 GPa.

Bibliography

Akahama 04. Akahama, Y. & Kawamura, H. High-pressure Raman spectroscopy of diamond anvils to 250 GPa: Method for pressure determination in the multimegabar pressure range. *J. Appl. Phys.* **96,** 3748–3751 (2004).

Akahama 06. Akahama, Y. & Kawamura, H. Pressure calibration of diamond anvil Raman gauge to 310 GPa. *J. Appl. Phys.* **100,** 043516 (2006).

Akahama 10. Akahama, Y. & Kawamura, H. Pressure calibration of diamond anvil Raman gauge to 410 GPa. *J. Phys. Conf. Ser.* **215,** 012195 (2010).

Anders 77. Anders, E. & Owen, T. Mars and Earth: Origin and abundance of volatiles. *Science* **198,** 453–465 (1977).

Ashcroft 04a. Ashcroft, N. W. Hydrogen dominant metallic alloys: High temperature superconductors? *Phys. Rev. Lett.* **92,** 187002–1 (2004).

Barbee 93. Barbee III, T. Metastability of atomic phases of nitrogen. *Phys. Rev. B* **48,** 9327 (1993).

Barrat 92. Barrat, J.-L. & Vos, W. L. Stability of van der Waals compounds and investigation of the intermolecular potential in helium–xenon mixtures. *J. Chem. Phys.* **97,** 5707–5712 (1992).

Bassett 01. Bassett, W. A. The birth and development of laser heating in diamond anvil cells. *Rev. Sci. Instrum.* **72,** 1270–1272 (2001).

Boehler 04. Boehler, R. & De Hantsetters, K. New anvil designs in diamond-cells. *High Press. Res.* **24,** 391–396 (2004).

Caldwell 97. Caldwell, W. A., Nguyen, J. H., Pfrommer, B. G., Mauri, F., Louie, S. G. & Jeanloz, R. Structure, bonding, and geochemistry of xenon at high pressures. *Science* **277,** 930–933 (1997).

Ciezak 09. Ciezak, J. A., Jenkins, T. A. & Hemley, R. J. Optical and Raman microspectroscopy of nitrogen and hydrogen mixtures at high pressures. *AIP Conf. Proc.* **1195,** 1291–1294 (2009).

Claassen 62. Claassen, H. H., Selig, H. & Malm, J. G. Xenon tetrafluoride. *J. Am. Chem. Soc.* **84,** 3593–3593 (1962).

Cromer 81. Cromer, D. T., Mills, R. L., Schiferi, D. & Schwalbe, L. A. The structure of N2 at 49 kbar and 299 K. *Acta Crystallogr. B* **37,** 8–11 (1981).

Darwent 70. Darwent, B. *Bond dissociation energies in simple molecules* Fifth edition (U.S. Government printing Office, 1970).

Datchi 07. Datchi, F., Dewaele, A., Loubeyre, P., Letoullec, R., Le Godec, Y. & Canny, B. Optical pressure sensors for high-pressure–high-temperature studies in a diamond anvil cell. *High Press. Res.* **27,** 447–463 (2007).

Dewaele 12. Dewaele, A., Loubeyre, P., Dumas, P. & Mezouar, M. Oxygen impurities reduce the metallization pressure of xenon. *Phys. Rev. B* **86,** 3–6 (2012).

Dewaele 16. Dewaele, A., Worth, N., Pickard, C. J., Needs, R. J., Pascarelli, S., Mathon, O., Mezouar, M. & Irifune, T. Synthesis and stability of xenon oxides Xe_2O_5 and Xe_3O_2 under pressure. *Nat. Chem.* **8,** 784–790 (2016).

Dubrovinskaia 03. Dubrovinskaia, N. & Dubrovinsky, L. Whole-cell heater for the diamond anvil cell. *Rev. Sci. Instrum.* **74,** 3433–3437 (2003).

Dubrovinskaia 16. Dubrovinskaia, N., Dubrovinsky, L., Solopova, N. A., Abakumov, A., Turner, S., Hanfland, M., Bykova, E., Bykov, M., Prescher, C., Prakapenka, V. B., *et al.* Terapascal static pressure generation with ultrahigh yield strength nanodiamond. *Sci. Adv.* **2,** e1600341 (2016).

Eremets 04b. Eremets, M. I., Gavriliuk, A. G., Trojan, I. A., Dzivenko, D. A. & Boehler, R. Single-bonded cubic form of nitrogen. *Nat. Mater.* **3,** 558–63 (2004).

Eremets 00. Eremets, M. I., Gregoryanz, E., Struzhkin, V., Mao, H. K., Hemley, R. J., Mulders, N. & Zimmerman, N. Electrical Conductivity of Xenon at Megabar Pressures. *Phys. Rev. Lett.* **85,** 2797–2800 (2000).

Eremets 01. Eremets, M. I., Hemley, R. J., Mao, H.-k. & Gregoryanz, E. Semiconducting non-molecular nitrogen up to 240 GPa and its low-pressure stability. *Nature* **411,** 170–174 (2001).

Eremets 11. Eremets, M. I. & Troyan, I. a. Conductive dense hydrogen. *Nat. Mater.* **10,** 927–931 (2011).

Errandonea 02. Errandonea, D., Boehler, R. & Ross, M. Melting of the alkaline-earth metals to 80 GPa. *Phys. Rev. B* **65,** 1–4 (2002).

Eucken 16. Eucken, A. *Verhandl. Deut. Physik. Ges.* **4** (1916).

Frost 16. Frost, M., Howie, R. T., Dalladay-Simpson, P., Goncharov, A. F. & Gregoryanz, E. Novel high-pressure nitrogen phase formed by compression at low temperature. *Phys. Rev. B* **93,** 024113 (2016).

Galtsov 07. Galtsov, N. N., Prokhvatilov, a. I. & Strzhemechny, M. a. Structure of quench condensed nH[sub 2]–N[sub 2] binary alloys: isotope effect. *Low Temp. Phys.* **33,** 499 (2007).

Goettel 89. Goettel, K. A., Eggert, J. H. & Silvera, I. F. Optical Evidence for the Metallization of Xenon at 132(5) GPa Kenneth. *Phys. Rev. Lett* **62,** 665–668 (1989).

Goncharov 12. Goncharov, A. F. Raman spectroscopy at high pressures. *Int. J. Spectrosc.* **2012** (2012).

Goncharov 08. Goncharov, A. F., Crowhurst, J. C., Struzhkin, V. V. & Hemley, R. J. Triple point on the melting curve and polymorphism of nitrogen at high pressure. *Phys. Rev. Lett* **101,** 1–4 (2008).

Goncharov 00. Goncharov, A. F., Gregoryanz, E., Mao, H.-k., Liu, Z. & Hemley, R. J. Optical evidence for a nonmolecular phase of nitrogen above 150 GPa. *Phys. Rev. Lett* **85,** 1262 (2000).

Goncharov 15. Goncharov, A. F., Holtgrewe, N., Qian, G., Hu, C., Oganov, A. R., Somayazulu, M., Stavrou, E., Pickard, C. J., Berlie, A., Yen, F., Mahmood, M., Lobanov, S. S., Konôpková, Z. & Prakapenka, V. B. Backbone NxH compounds at high pressures. *J. Chem. Phys.* **142,** 214308 (2015).

Goncharov 09. Goncharov, A. F., Montoya, J. A., Subramanian, N., Struzhkin, V. V., Kolesnikov, A., Somayazulu, M. & Hemley, R. J. Laser heating in diamond anvil cells: developments in pulsed and continuous techniques. *Journal of synchrotron radiation* **16,** 769–772 (2009).

Greenwood 12. Greenwood, N. N. & Earnshaw, A. *Chemistry of the Elements* (Elsevier, 2012).

Gregoryanz 01. Gregoryanz, E., Goncharov, A. F., Hemley, R. J. & Mao, H.-k. High-pressure amorphous nitrogen. *Phys. Rev. B* **64,** 052103 (2001).

Gregoryanz 02. Gregoryanz, E., Goncharov, A. F., Hemley, R. J., Mao, H.-k., Somayazulu, M. & Shen, G. Raman, infrared, and x-ray evidence for new phases of nitrogen at high pressures and temperatures. *Phys. Rev. B* **66,** 224108 (2002).

Gregoryanz 07. Gregoryanz, E., Goncharov, A. F., Sanloup, C., Somayazulu, M., Mao, H.-k. & Hemley, R. J. High P-T transformations of nitrogen to 170 GPa. *J. Chem. Phys.* **126,** 184505 (2007).

Gregoryanz 08. Gregoryanz, E., Lundegaard, L. F., McMahon, M. I., Guillaume, C., Nelmes, R. J. & Mezouar, M. Structural diversity of sodium. *Science* **320,** 1054–1057 (2008).

Haber 22. Haber, F. The production of ammonia from nitrogen and hydrogen. *Sci. Nat.* **10,** 1041–1049 (1922).

Hanfland 98. Hanfland, M., Lorenzen, M., Wassilew-Reul, C. & Zontone, F. Structures of Molecular Nitrogen at High Pressures. *Rev. High Press. Sci. Technol.* **7,** 787–789 (1998).

Hernandez 88. Hernández, G. *Fabry-perot interferometers* (Cambridge University Press, 1988).

Howie 14. Howie, R. T., Magdău, I. B., Goncharov, A. F., Ackland, G. J. & Gregoryanz, E. Phonon localization by mass disorder in dense hydrogen-deuterium binary alloy. *Phys. Rev. Lett* **113,** 175501 (2014).

Howie 16a. Howie, R. T., Turnbull, R., Binns, J., Frost, M., Dalladay-Simpson, P. & Gregoryanz, E. Formation of xenon-nitrogen compounds at high pressure. *Sci. Rep.* **6,** 34896 (2016).

Hu 11. Hu, A. & Zhang, F. A hydronitrogen solid: high pressure ab initio evolutionary structure searches. *J. Phys. Condens. Matter* **23,** 022203 (2011).

Jamieson 59. Jamieson, J. C., Lawson, A. & Nachtrieb, N. New Device for Obtaining X-Ray Diffraction Patterns from Substances Exposed to High Pressure. *Rev. Sci. Instrum.* **30,** 1016–1019 (1959).

Jayaraman 83. Jayaraman, A. Diamond anvil cell and high-pressure physical investigations. *Rev. Mod. Phys.* **55,** 65–108 (1 Jan. 1983).

Jephcoat 87. Jephcoat, A., Mao, H.-k., Finger, L., Cox, D., Hemley, R. & Zha, C.-s. Pressure-induced structural phase transitions in solid xenon. *Phys. Rev. Lett* **59,** 2670 (1987).

Jiang 14. Jiang, S., Huang, X., Duan, D., Zheng, S., Li, F., Yang, X., Zhou, Q., Liu, B. & Cui, T. Hydrogen Bond in Compressed Solid Hydrazine. *J. Phys. Chem. C* **118,** 3236–3243 (2014).

Katzke 08. Katzke, H. & Tolédano, P. Theoretical description of pressure- and temperature-induced structural phase transition mechanisms of nitrogen. *Phys. Rev. B* **78,** 1–13 (2008).

Kim 11. Kim, M. & Yoo, C.-S. Highly repulsive interaction in novel inclusion D2–N2 compound at high pressure: Raman and x-ray evidence. *J. Chem. Phys.* **134,** 044519 (2011).

Klee 91. Klee, H. & Knorr, K. Orientational-ordering transition fcc-Pa3 of Ar 1-x (N2) x. *Phys. Rev. B* **43,** 8658 (1991).

Kleppe 14. Kleppe, A. K., Amboage, M. & Jephcoat, A. P. New high-pressure van der Waals compound Kr (H2) 4 discovered in the krypton-hydrogen binary system. *Sci. Rep.* **4,** 4989 (2014).

Kooi 99b. Kooi, M. E. & Chouten, J. High-pressure Raman investigation of mutual solubility and compound formation in Xe-N2 and Ne-N2. *Phys. Rev. B* **60,** 12635–12643 (1999).

Kooi 99a. Kooi, M. E., Michels, J. P. J. & Schouten, J. A. Negative vibrational shift of nitrogen diluted in xenon at the fluid–solid transition. *J. Chem. Phys.* **110,** 3023 (1999).

Landsberg 28. Landsberg, G. & Mandelstam, L. Über die Lichtzerstreuung in Kristallen. *Z. Phys.* **50,** 769–780 (1928).

Laniel 18. Laniel, D., Svitlyk, V., Weck, G. & Loubeyre, P. Pressure-induced chemical reactions in the N2 (H2) 2 compound: from the N2 and H2 species to ammonia and back down into hydrazine. *Phys. Chem. Chem. Phys.* (2018).

Liu 00. Liu, M. S., Bursill, L. A., Prawer, S. & Beserman, R. Temperature dependence of the first-order Raman phonon line of diamond. *Phys. Rev. B* **61,** 3391 (2000).

Loa 12. Loa, I., Nelmes, R., Lundegaard, L. & McMahon, M. Extraordinarily complex crystal structure with mesoscopic patterning in barium at high pressure. *Nat. Mater.* **11,** 627 (2012).

Long 77. Long, D. A. & Long, D. *Raman spectroscopy* (McGraw-Hill New York, 1977).

Loubeyre 92. Loubeyre, P., LeToullec, R. & Pinceaux, J. P. Raman measurements of the vibrational properties of H_2 as a guest molecule in dense helium, neon, argon, and deuterium systems up to 40 GPa. *Phys. Rev. B* **45,** 12844–12853 (22 June 1992).

Loubeyre 93. Loubeyre, P., Jean-Louis, M., LeToullec, R. & Charon-Gérard, L. High pressure measurements of the He-Ne binary phase diagram at 296 K: Evidence for the stability of a stoichiometric Ne (He) 2 solid. *Phys. Rev. Lett.* **70,** 178 (1993).

Loubeyre 95. Loubeyre, P. & LeToullec, R. Stability of O2/H2 mixtures at high pressure. *Nature* **378,** 44 (1995).

Loubeyre 94. Loubeyre, P., Letoullec, R. & Pinceaux, J.-P. Compression of $Ar(H_2)_2$ up to 175 GPa: A new path for the dissociation of molecular hydrogen? *Phys. Rev. Lett* **72,** 1360–1363 (1994).

Loubeyre 96. Loubeyre, P., LeToullec, R., Hausermann, D., Hanfland, M., *et al.* X-ray diffraction and equation of state of hydrogen at megabar pressures. *Nature* **383,** 702 (1996).

Lundeen 75. Lundeen, J. W. & Koehler, W. H. Liquid ammonia. Comparative study of models via Raman spectroscopy. *J. Phys. Chem.* **79,** 2957–2963 (1975).

Mailhiot 92. Mailhiot, C., Yang, L. H. & McMahan, A. K. Polymeric nitrogen. *Phys. Rev. B* **46,** 14419–14435 (1992).

McMahan 85. McMahan, A. & LeSar, R. Pressure dissociation of solid nitrogen under 1 Mbar. *Phys. Rev. Lett* **54,** 1929 (1985).

Mcmillan 05. McMillan, P. F. Pressing on: the legacy of Percy W. Bridgman. *Nat. Mater.* **4,** 715 (2005).

Merrill 74. Merrill, L. & Bassett, W. A. Miniature diamond anvil pressure cell for single crystal x-ray diffraction studies. *Rev. Sci. Instrum.* **45,** 290–294 (1974).

Mills 80. Mills, R. L., Liebenberg, D. H., Bronson, J. C. & Schmidt, L. C. Procedure for loading diamond cells with high-pressure gas. *Rev. Sci. Instrum.* **51,** 891–895 (1980).

Mills 86. Mills, R. L., Olinger, B. & Cromer, D. T. Structures and phase diagrams of N2 and CO to 13 GPa by x-ray diffraction. *J. Chem. Phys.* **84,** 2837 (1986).

Nellis 12. Nellis, W. J. Seeing Deep Inside Icy Giant Planets. *Physics* **5,** 25 (2012).

Ninet 16. Ninet, S. & Datchi, F. High pressure – high temperature phase diagram of ammonia. **154508,** 154508 (2016).

Ojwang 12. Ojwang, J. G., Stewart Mcwilliams, R., Ke, X. & Goncharov, A. F. Melting and dissociation of ammonia at high pressure and high temperature. *J. Chem. Phys.* **137,** 064507 (2012).

Olijnyk 90. Olijnyk, H. High pressure x-ray diffraction studies on solid N2 up to 43.9 GPa. *J. Chem. Phys.* **93,** 8968 (1990).

Olijnyk 99. Olijnyk, H. & Jephcoat, A. P. Vibrational Dynamics of Isotopically Dilute Nitrogen to 104 GPa. *Phys. Rev. Lett* **83,** 332–335 (1999).

Olszewski 84. Olszewski, K. Nouveaux essais de liquefaction de l'hydrogene. Solidification et pression critique de l'ozote. *Compt. Rend. Acad. Sci. Paris* **98,** 913–915 (1884).

Pauling 33. Pauling, L. The Formulas of Antimonic Acid and the Antimonates. *J. Am. Chem. Soc.* **55,** 1895–1900 (1933).

Peng 15. Peng, F., Wang, Y., Wang, H., Zhang, Y. & Ma, Y. Stable xenon nitride at high pressures. *Phys. Rev. B* **92,** 1–5 (2015).

Petricek 14. Petricek, V., Dusek, M. & Palatinus, L. Crystallographic computing system JANA2006: general features. *Zeitschrift für Kristallographie-Crystalline Materials* **229,** 345–352 (2014).

Pickard 2009. Pickard, C. J. & Needs, R. High-pressure phases of nitrogen. *Phys. Rev. Lett* **102,** 125702 (2009).

Plisson 14. Plisson, T., Weck, G. & Loubeyre, P. (N2)6 Ne7: A High Pressure van der Waals Insertion Compound. *Phys. Rev. Lett.* **113,** 025702 (2014).

Prescher 15. Prescher, C. & Prakapenka, V. B. DIOPTAS: a program for reduction of two-dimensional X-ray diffraction data and data exploration. *High Press. Res.* **35,** 223–230 (2015).

Qian 16. Qian, G.-R., Niu, H., Hu, C.-H., Oganov, A. R., Zeng, Q. & Zhou, H.-Y. Diverse Chemistry of Stable Hydronitrogens, and Implications for Planetary and Materials Sciences. *Sci. Rep.* **6.** doi:10.1038/srep25947 (2016).

Raman 28b. Raman, C. V. A new radiation. *Indian J. Phys.* **2,** 387–398 (1928).

Raman 28a. Raman, C. V. & Krishnan, K. S. A new type of secondary radiation. *Nature* **121,** 501–502 (1928).

Reichlin 89. Reichlin, R., Brister, K. E., McMahan, A. K., Ross, M., Martin, S., Vohra, Y. K. & Ruoff, A. L. Evidence for the insulator-metal transition in xenon from optical, x-ray, and band-structure studies to 170 GPa. *Phys. Rev. Lett* **62,** 669–672 (1989).

Rice 07. Rice, B. M., Byrd, E. F. C. & Mattson, W. D. in *High Energy Density Materials* (ed Klapötke, T. M.) 153–194 (Springer Berlin Heidelberg, Berlin, Heidelberg, 2007). ISBN: 978-3-540-72202-1. doi:10.1007/430_2006_053.

Rutherford 72. Rutherford, D. *Dissertatio inauguralis de aere fixo dicto, aut mephitico...* PhD thesis (Balfour et Smellie, 1772).

Sanloup 05. Sanloup, C., Schmidt, B. C., Perez, E. M. C., Jambon, A., Gregoryanz, E. & Mezouar, M. Retention of xenon in quartz and Earth's missing xenon. *Science* **310,** 1174–1177 (2005).

Scandolo 03. Scandolo, S. & Jeanloz, R. The Centers of Plantes: In laboratories and computers, shocked and squeezed matter turns metallic, coughs up diamonds and reveals Earth's white-hot center. *Am. Sci.* **91,** 516–525 (2003).

Scheerboom 93. Scheerboom, M. I. M. & Schouten, J. A. Anomalous Behavior of the Vibrational Spectrum of the High-Pressure delta Phase of Nitrogen: A Second-Order Transition. **71,** 2252–2255 (1993).

Scheler 11. Scheler, T., Degtyareva, O. & Gregoryanz, E. On the effects of high temperature and high pressure on the hydrogen sol-

ubility in rhenium. *J. Chem. Phys.* **135.** doi:10.1063/1.3652863 (2011).

Schiferl 83. Schiferl, D., Cromer, D. T., Ryan, R. R., Larson, a. C., Lesar, R. & Mills, R. L. Structure o f N2 at 2.94 GPa and 300K. *Acta Crystallogr. C* **39,** 1151 (1983).

Schiferl 85. Schiferl, D., Buchsbaurn, S. & Mills, R. L. Phase Transitions in Nitrogen Observed by Raman Spectroscopy from 0.4 to 27.4 GPa at 15 K. *J. Phys. Chem.* **89,** 2324–2330 (1985).

Schuch 70. Schuch, a. F. Crystal Structures of the Three Modifications of Nitrogen 14 and Nitrogen 15 at High Pressure. *J. Chem. Phys.* **52,** 6000 (1970).

Sheldrick 15b. Sheldrick, G. M. Crystal structure refinement with SHELXL. *Acta Crystallogr. C* **71,** 3–8 (2015).

Sheldrick 15a. Sheldrick, G. M. SHELXT–Integrated space-group and crystal-structure determination. *Acta Crystallographica Section A: Foundations and Advances* **71,** 3–8 (2015).

Sihachakr 04. Sihachakr, D. & Loubeyre, P. O_2/N_2. *Phys. Rev. B* **70,** 134105 (13 Oct. 2004).

Skriver 85. Skriver, H. L. Crystal structure from one-electron theory. *Phys. Rev. B* **31,** 1909–1923 (1985).

Smekal 23. Smekal, A. Zur quantentheorie der dispersion. *Sci. Nat.* **11,** 873–875 (1923).

Somayazulu 10. Somayazulu, M., Dera, P., Goncharov, A. F., Gramsch, S. A., Liermann, P., Yang, W., Liu, Z., Mao, H.-k. & Hemley, R. J. Pressure-induced bonding and compound formation in xenon–hydrogen solids. *Nat. Chem.* **2,** 50–53 (2010).

Spaulding 14. Spaulding, D. K., Weck, G., Loubeyre, P., Datchi, F., Dumas, P. & Hanfland, M. Pressure-induced chemistry in a nitrogen-hydrogen host–guest structure. *Nat. Commun.* **5,** 5739 (2014).

Stewart 55. Stewart, J. W. Compressibilities of some solidified gases at low temperature. *Phys. Rev.* **97,** 578–582 (1955).

Stinton 09. Stinton, G. W., Loa, I., Lundegaard, L. F. & McMahon, M. I. The crystal structures of δ and δ* nitrogen. *J. Chem. Phys.* **131.** doi:10.1063/1.3204074 (2009).

Swenson 55. Swenson, C. A. New Modification of Solid Nitrogen. *J. Chem. Phys.* **23,** 1963 (1955).

Syassen 08. Syassen, K. Ruby under pressure. *High Press. Res.* **28,** 75–126 (2008).

Tateno 2010. Tateno, S., Hirose, K., Ohishi, Y. & Tatsumi, Y. The structure of iron in Earth's inner core. *Science* **330,** 359–361 (2010).

Thorn 12. Thorn, A., Dittrich, B. & Sheldrick, G. M. Enhanced rigid-bond restraints. *Acta Crystallographica Section A: Foundations of Crystallography* **68,** 448–451 (2012).

Toby 06. Toby, B. H. R factors in Rietveld analysis: how good is good enough? *Powder diffraction* **21,** 67–70 (2006).

Toby 13. Toby, B. H. & Von Dreele, R. B. GSAS-II: the genesis of a modern open-source all purpose crystallography software package. *Journal of Applied Crystallography* **46,** 544–549 (2013).

Tomasino 14a. Tomasino, D., Jenei, Z., Evans, W. & Yoo, C. S. Melting and phase transitions of nitrogen under high pressures and temperatures. *J. Chem. Phys.* **140.** doi:10.1063/1.4885724 (2014).

Tomasino 14b. Tomasino, D., Kim, M., Smith, J. & Yoo, C. S. Pressure-induced symmetry-lowering transition in dense nitrogen to layered polymeric nitrogen (LP-N) with colossal raman intensity. *Phys. Rev. Lett.* **113,** 1–5 (2014).

Vos 92. Vos, W., Finger, L., Hemley, R., Hu, J., Mao, H.-k. & Schouten, J. A high-pressure van der Waals compound in solid nitrogen-helium mixtures. *Nature* **358,** 46–48 (1992).

Wang 15. Wang, H., Eremets, M. I., Troyan, I., Liu, H., Ma, Y. & Vereecken, L. Nitrogen Backbone Oligomers. *Sci. Rep.* **5,** 13239 (2015).

Weck 2017. Weck, G., Datchi, F., Garbarino, G., Ninet, S., Queyroux, J.-A., Plisson, T., Mezouar, M. & Loubeyre, P. Melting Curve and Liquid Structure of Nitrogen Probed by X-ray Diffraction to 120 GPa. *Phys. Rev. Lett* **119,** 235701 (2017).

Weck 10. Weck, G., Dewaele, A. & Loubeyre, P. Oxygen/noble gas binary phase diagrams at 296 K and high pressures. *Phys. Rev. B* **82,** 014112 (2010).

Weir 59. Weir, C., Lippincott, E., Van Valkenburg, A. & Bunting, E. Infrared studies in the 1-to 15-micron region to 30,000 atmospheres. *J. Res. Natl. Bur. Stand. A* **63,** 55–62 (1959).

Wigner 35. Wigner, E. & Huntington, H. á. On the possibility of a metallic modification of hydrogen. *J. Chem. Phys.* **3,** 764–770 (1935).

Wojdyr 10. Wojdyr, M. *Fityk*: a general-purpose peak fitting program. *J. Appl. Crystallogr.* **43,** 1126–1128 (Oct. 2010).

Yin 15. Yin, K., Wang, Y., Liu, H., Peng, F. & Zhang, L. N 2 H: a novel polymeric hydronitrogen as a high energy density material. *J. Mater. Chem. A* **3,** 4188–4194 (2015).

Zha 03. Zha, C.-S. & Bassett, W. A. Internal resistive heating in diamond anvil cell for in situ X-ray diffraction and Raman scattering. *Rev. Sci. Instrum.* **74,** 1255–1262 (2003).

Publications

The published work of Chapter 5 is attached below. The author of this thesis is the second author of the article.

SCIENTIFIC REPORTS

OPEN

Formation of xenon-nitrogen compounds at high pressure

Ross T. Howie[1], Robin Turnbull[2], Jack Binns[1], Mungo Frost[2], Philip Dalladay-Simpson[1] & Eugene Gregoryanz[2]

Received: 06 September 2016
Accepted: 19 September 2016
Published: 17 October 2016

Molecular nitrogen exhibits one of the strongest known interatomic bonds, while xenon possesses a closed-shell electronic structure: a direct consequence of which renders both chemically unreactive. Through a series of optical spectroscopy and x-ray diffraction experiments, we demonstrate the formation of a novel van der Waals compound formed from binary Xe-N_2 mixtures at pressures as low as 5 GPa. At 300 K and 5 GPa $Xe(N_2)_2$-I is synthesised, and if further compressed, undergoes a transition to a tetragonal $Xe(N_2)_2$-II phase at 14 GPa; this phase appears to be unexpectedly stable at least up to 180 GPa even after heating to above 2000 K. Raman spectroscopy measurements indicate a distinct weakening of the intramolecular bond of the nitrogen molecule above 60 GPa, while transmission measurements in the visible and mid-infrared regime suggest the metallisation of the compound at ~100 GPa.

Nitrogen is the most abundant element in the terrestrial atmosphere, existing as a diatomic molecule with one of the strongest known triple bonds and as a result is unreactive at ambient conditions. Under high compression, molecular nitrogen exhibits a rich polymorphism[1–7] and significant overlap of thermodynamically competing phases, dependent on formation conditions[8]. The application of high pressure can also provide new synthesis routes, initiating chemical processes that would not happen otherwise, such as N_2 becoming reactive with the noble metals, as in the formation of platinum or iridium nitrides[9,10]. Xenon, an archetypical inert gas due to its closed shell system, has long been known to form stable halide and oxide compounds through chemical synthesis[11,12]. The reactivity can also be fundamentally altered with the application of high pressure, the process which has produced van der Waals compounds composed of Xe-H_2[13] and Xe-O_2[14], as well as a Xe-H_2O clathrate[15]. Direct reactions have also been observed such as that between xenon and ice[16] and the recently reported stable oxides, Xe_2O_5 and Xe_3O_2[17]. Xenon has also been shown to be inserted into both quartz[18], and a small-pore zeolite at high pressure and temperature[19]. Theoretical studies also suggest the increased reactivity of xenon at high pressures with the formation of binary solids Xe-O[20,21], Xe-Fe/Ni[22], and Xe-Mg[23] synthesised solely from their constituent elements. Such studies on the reactivity of xenon, especially with terrestrially abundant elements, could provide an explanation into the significant under-abundance of xenon detectable in the Earth's atmosphere.

The direct reaction of N_2 and Xe would seem unlikely due to the relative inertness of both materials. Nevertheless, a recent theoretical study predicts the formation of novel xenon nitride compounds above 146 GPa with stoichiometry - XeN_6[24]. Possible interactions between Xe and N_2 have been explored experimentally at low pressures investigating mutual solubility[25,26]. Through Raman spectroscopic measurements those studies inferred the formation of an orientationally disordered van der Waals compound but were limited up to pressures of 13 GPa at 408 K with no structural investigation.

It is known that at high pressures both xenon and nitrogen exhibit (semi-)conducting phases. Xenon has been shown to transform to metallic state at pressures between 130–150 GPa, giving it the lowest pressure of metallisation amongst the rare gas solids[27–29] and nitrogen becomes semiconducting with band gap of 0.4 eV at 240 GPa[2,3]. Previous studies have claimed that by doping Xe with O_2, the metallisation pressure is drastically reduced[30]. Therefore it is of significant interest to investigate pressure-induced electronic effects of any formed Xe-N_2 compound. Here, we report the synthesis and characterisation of a Xe-N_2 van der Waals compound through x-ray diffraction, Raman and transmission spectroscopies. We show that two inert condensed gases form a $Xe(N_2)_2$ compound at pressures as low as 5 GPa at room temperature. When the novel compound is formed in a xenon medium, it becomes metallic at around 100 GPa, whilst $Xe(N_2)_2$ with an abundance of nitrogen demonstrates metallic behaviour above ~140 GPa.

[1]Center for High Pressure Science & Technology Advanced Research, Shanghai, 201203, P.R. China. [2]Centre for Science at Extreme Conditions and School of Physics and Astronomy, University of Edinburgh, Edinburgh, UK. Correspondence and requests for materials should be addressed to R.T.H. (email: ross.howie@hpstar.ac.cn)

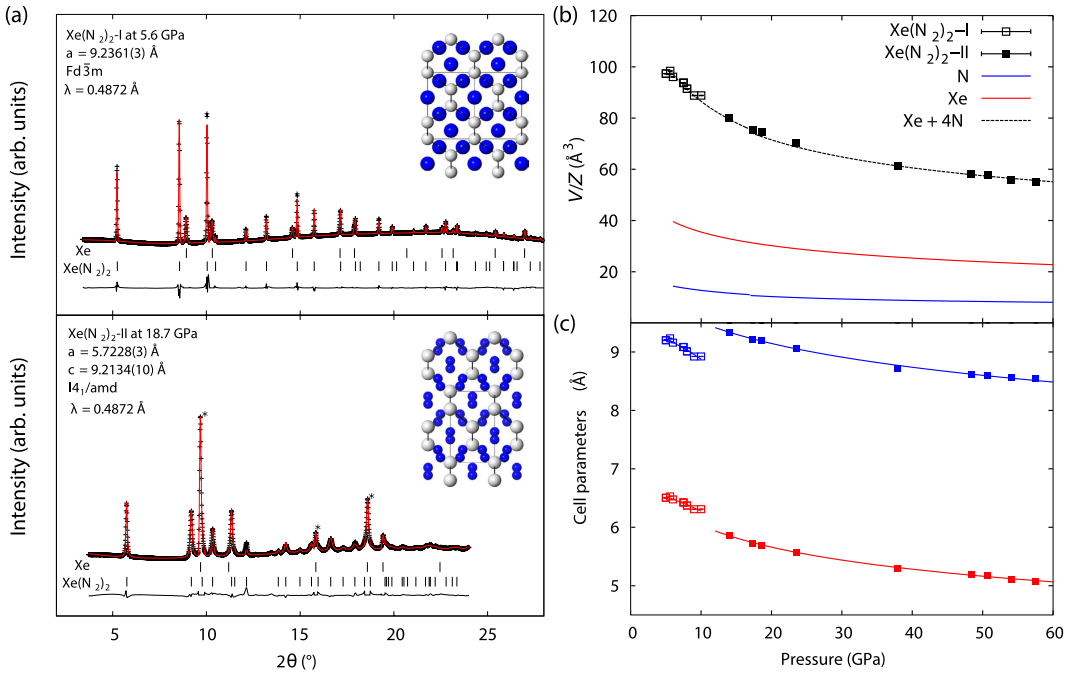

Figure 1. (**a**) Powder X-ray diffraction patterns at 5.6 and 18.7 GPa used for Rietveld refinement. Below 14 GPa, $Xe(N_2)_2$ adopts a face-centered cubic structure, space group $Fd\bar{3}m$, $a = 9.2361(3)$ Å denoted $Xe(N_2)_2$-I. At 14 GPa and above $Xe(N_2)_2$ undergoes a transition to a body-centered tetragonal structure, $I4_1/amd$, with unit-cell dimensions $a = 5.7228(3)$, $c = 9.2134(10)$ Å at 18.7 GPa. Peaks corresponding to Xe (marked with *) were excluded from the profile used in the refinement. Insets show crystal-structure projections for both phases, phase I is rotated to view down the face diagonal ⟨110⟩ highlighting structural similarity to phase II. Freely rotating N_2 molecules in phase I are represented by blue spheres, whilst in phase II blue spheres represent atoms in aligned N_2 molecules; (**b**) Equation-of-state data for $Xe(N_2)_2$ compounds. Pressure-volume per Z data for Xe phases is indicated by red lines[32], N_2 phases by blue lines[6]. Black squares indicate volume per Z data for $Xe(N_2)_2$ phases I and II, dashed black line indicates the calculated volume for stoichiometry Xe + 4N from atomic volume data; (**c**) Response of unit-cell dimensions to applied pressure for $Xe(N_2)_2$, phase I data are shown for unit-cell length a (blue open squares) and $d_{\langle 110\rangle}$ (red open squares), phase II data is plotted for unit-cell lengths a (red closed squares) and c (blue closed squares). Solid lines indicate fitted linear Birch-Murnaghan linear equations of state?

Mixtures of Xe-N_2 at various concentration were loaded into diamond-anvil cells (DAC) using a combination of cryogenic and high-pressure gas-loading techniques (see Methods section). Compressing the mixture above 2 GPa leads to the formation of a xenon single crystal surrounded by liquid N_2 as seen visually and in x-ray diffraction measurements (see Figs S1 and S2). At pressures above 5 GPa we observe the formation of a N_2-rich compound in the media surrounding the xenon single crystal (Fig. S2). Through x-ray powder diffraction analysis we have identified this phase as having a *fcc* structure, with $a = 9.2361(3)$ Å at 5.6 GPa (Fig. 1), indexing with space group $Fd\bar{3}m$ or $Fd\bar{3}$ accounts for all observed Bragg peaks. Several patterns were of sufficient quality to allow for Rietveld refinement, otherwise Le Bail fitting was used to extract unit-cell dimensions. Solution of the structure by charge-flipping suggests space group $Fd\bar{3}m$. Two atomic sites could be refined; Xe(0, 0, 0) and $N\left(\frac{5}{8}, \frac{1}{8}, \frac{1}{8}\right)$ resulting in a cubic Laves Cu_2Mg-type structure (Fig. 1(a)).

From both the structure type and unit-cell dimensions we determine the stoichiometry as $Xe(N_2)_2$, designated $Xe(N_2)_2$-I herein, which is in excellent agreement with the calculated equation-of-state data for Xe + 4N (Fig. 1(b), see also below). Both the structure type and the stoichiometry are identical to that proposed for oxygen-rich xenon mixtures[14]. The N-N site distances of 3.2655(1) Å are clearly too long to be bonded, these sites therefore represent scattering from disordered N_2 molecules. N_2 molecules have been found to adopt both spherical and disk-like rotational disordering in the solid state[31], and refinement of both disorder types was attempted, with a spherical disorder model (*i.e.* with the N-site occupancy equal to 2) resulting in the best fit to the data (see table in SM for more details on the structure refinement). The structure of this phase can be considered as a diamond-type host lattice of Xe atoms with four rotationally disordered N_2 molecules forming a tetrahedron within each vacancy. The N-N site distance of 3.2655(1) Å implies a N…N closest-contact distance of 2.1655(1) Å.

Raman spectroscopy measurements of the formed single crystal at 2 GPa reveals the appearance of a weak vibrational mode, which is lower in frequency than the fluid N_2 vibrational mode by 10 cm^{-1} (compare red and black spectra in Fig. 2). This mode has been observed in a previous high-temperature study and attributed to fluid N_2 dissolved in the Xe crystal lattice[26]. By contrast, in xenon-rich samples (*ca.* 4:1 concentration), we observe the complete transformation of the sample, evident through only the low-frequency vibrational mode and no evidence of excess N_2 (see SM).

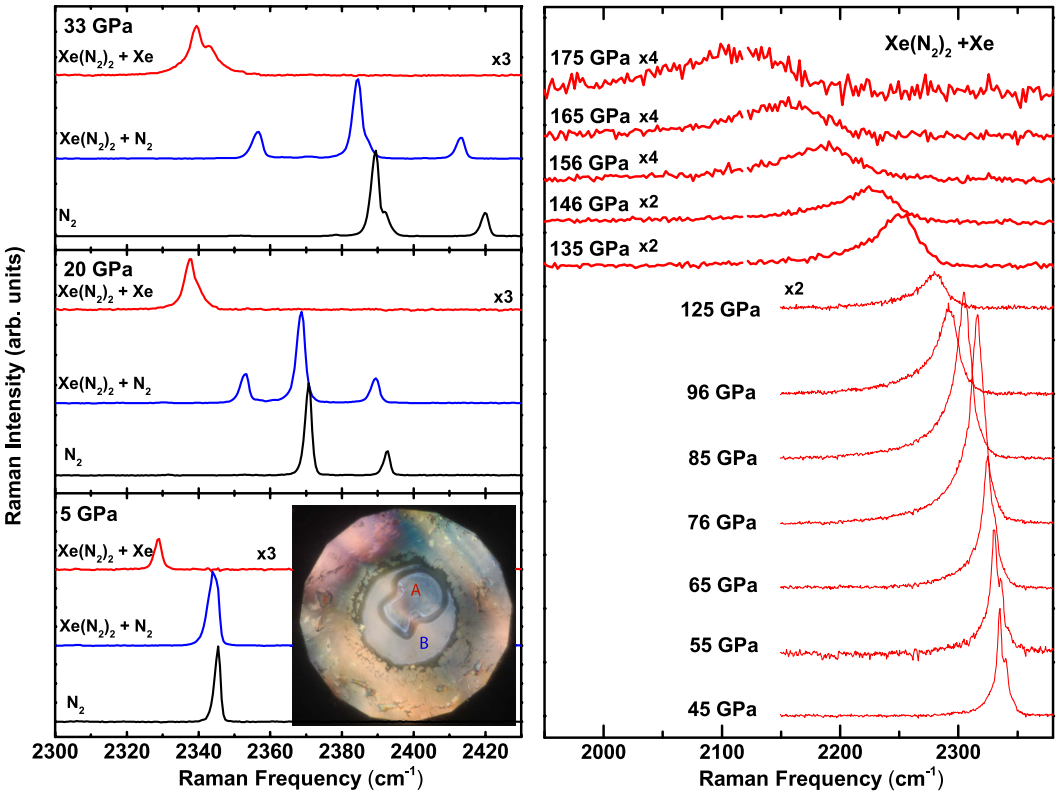

Figure 2. (**a**) Representative vibrational Raman spectra of the Xe-N_2 compound at 5, 20 and 33 GPa. Red spectra are from the formed compound in Xe media, whilst blue spectra show the compound formed in N_2 media. As a comparison, vibrational spectra of pure N_2 are shown in black. Inset: Photomicrograph of sample at 5 GPa. Red spectra were taken at position A in the single crystal and blue spectra were taken in the surrounding medium at position B. (**b**) Representative vibrational Raman spectra of $Xe(N_2)_2$ in a Xe matrix to pressures of 175 GPa.

In Raman measurements of the surrounding media (see blue spectra in Fig. 2), we observe a broad N_2 mode at 5 GPa, which consists of overlapping modes of $Xe(N_2)_2$-I, as determined by x-ray diffraction, and pure N_2 that increasingly separate in frequency space at higher pressure. The vibrational mode of $Xe(N_2)_2$-I (blue spectra in Fig. 2) and the vibrational mode attributed to N_2 in Xe (red spectra in Fig. 2), exhibit identical behaviour with pressure (see red and blue points in Fig. 3a), suggesting that the latter is most likely due to small crystallites of $Xe(N_2)_2$-I that form within a Xe matrix. It should be noted that the prescence of this N-containing dopant does not significantly affect the measured unit-cell volume which agrees with the literature to within experimental error[32].

Above pressures of 14 GPa, we observe a phase transition from the low-pressure $Xe(N_2)_2$-I to a high-pressure $Xe(N_2)_2$-II phase. This transition pressure corresponds approximately to the critical pressure of the δ to ϵ transition in pure molecular N_2. $Xe(N_2)_2$-II adopts a body-centered tetragonal cell with $a = 5.7228(3)$, $c = 9.2134(10)$ Å at 18.7 GPa (Fig. 1). Systematic-absence analysis unambiguously confirm space-group symmetry $I4_1/amd$. Again Xe is located at the origin, with one N position refined to (0.5, 0.721(2), 0.179(1)). This position lies displaced by 0.52(2) Å from an inversion centre resulting in four ordered N_2 molecules aligned along the c-axis. Final Rietveld agreement factors are $R_p = 0.015$ and $R = 0.094$.

The origin of this transition lies in the ordered orientation of N_2 molecules within the vacancy, corroborated by the poorer fit to the data ($R = 0.1672$) with a spherically-disordered N_2 molecule model. Shortest N…N interatomic distances are now 2.5238(1) Å and 2.610(12) Å at 18.7 GPa. Recalling that the shortest N…N interatomic distances at 5.6 GPa were 2.1655 (1) Å in phase I, the alignment of N_2 molecules relieves unfavourable close N…N contacts while maintaing the same coordination number for each N_2 molecule.

Over the I-II phase transition the unit cell undergoes a tetragonal distortion elongating by 0.323(3) Å (+3.6%) along **c** accompanied by a reduction of −0.519(1) Å (−8.1%) along tetragonal **a**, corresponding to ⟨110⟩ in phase I (see table in SM for more details on the structure refinement). We tracked unit-cell dimensions for $Xe(N_2)_2$-II up to 58 GPa (Fig. 1(c)), confirming again the stoichiometry of the compound (Fig. 1(a)) and allowing the determination of equation-of-state parameters for both $Xe(N_2)_2$ phases (see methods section). At pressures of 38 GPa and above there were clear signs of the incipient high-pressure *hcp* phase of Xe accompanied by strong diffuse scattering and increased background at d-spacings overlapping with a significant number of $Xe(N_2)_2$ reflections and above 58 GPa unit-cell dimensions could not be reliably extracted from the data. However the low-angle (101) reflection could be observed up to 103 GPa (see Fig. S4).

Above 40 GPa, the frequency dependence with pressure of the vibrational mode of $Xe(N_2)_2$ deviates greatly from that of pure N_2 (Fig. 3). The maximum in the vibrational frequency *vs.* pressure is shifted from 80 GPa in pure N_2 to 30 GPa. In the sample in Xe matrix, we observe splitting of the vibrational band (see Fig. 2) up to 70 GPa, after

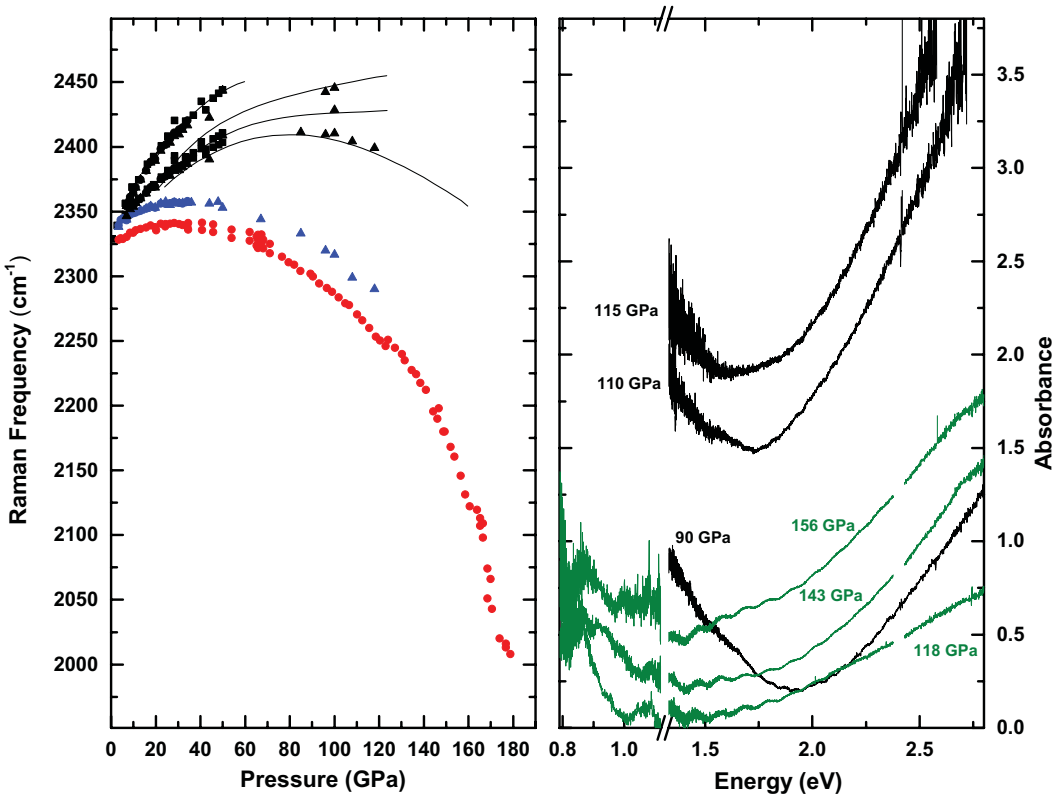

Figure 3. Left Panel: Frequencies of the vibrational modes as a function of pressure. $Xe(N_2)_2$ Raman frequencies in Xe medium are shown in red, $Xe(N_2)_2$ Raman frequencies in N_2 medium are shown in blue and black points are the Raman frequencies of the excess N_2. Black lines are taken from a study on pure N_2[1]. Right Panel: Optical absorption as a function of energy for Xe-rich (black) and N_2-rich (green) samples. The reference spectra were taken at 50 GPa in both experiments.

which the splitting is not distinguishable due to the enhanced broadening of the modes. At 140 GPa the N_2 vibrational frequencies of $Xe(N_2)_2$ are 2161 cm^{-1} and 2212 cm^{-1}, considerably lower frequencies than either those of κ-N_2 (2376 cm^{-1}) or λ-N_2 (2320 cm^{-1}, 2400 cm^{-1}). Interestingly, at 178 GPa, we observe the persistence of molecular nitrogen, which is above the pressure at which pure N_2 is claimed to become non-molecular (η-N_2)[1–3]. We note that although we observe a much softer N_2 molecular mode than that just before ζ transforms to the non-molecular amorphous η phase in pure N_2, there is no evidence that the N_2 molecules in $Xe(N_2)_2$ dissociate to form Xe-N bonding. However, there is a clear reduction in intensity (see Fig. 2) together with a marked increase in the FWHH (see Fig. S5) indicating that the molecular N-N bond is weakening. Up to highest pressure studied (180 GPa) we see no evidence of Xe-N bonded compounds predicted by theory[24]. In an attempt to promote synthesis of such compounds, we performed laser heating of the sample to temperatures of 3000 K at 120, 150, 160 and 180 GPa but no transition was observed in either Raman spectroscopy or x-ray diffraction. It is remarkable that a van der Waals solid, the components of which are inert materials, can remain stable to such extreme conditions.

Figure 3(b) shows the transmission spectra collected from two samples with different initial ratio of Xe and N_2. The spectra were collected with both visible and mid infrared light sources which allow the coverage of energy region between ~3 to 0.6 eV. The samples in a Xe matrix (black), appear to exhibit metallic behaviour evident by the sharp rise in the absorption in the near-IR, which shifts with pressure. By 120 GPa, no detectable transmission was observed in the visible, the sample appearance became shiny and reflected red laser light (see photomicrographs in Fig. S6). Samples of $Xe(N_2)_2$ with higher N_2 concentrations do exhibit absorption (Fig. 3 green) but not to the same extent as in the Xe matrix, which could be due to the excess of N_2. Pure xenon has been shown to be conductive at above 135 GPa through both absorption/reflectivity and electrical measurements[27–29]. The mechanism of conductivity is an indirect overlap of the 5*p* valence and 5*d* conduction bands. Although determining the mechanism was beyond the scope of this study, our results indicate that by doping Xe with N_2, or $Xe(N_2)_2$, we are able to tune the conductive properties of Xe and lower the pressure of metallisation.

Our results demonstrate that xenon can form compounds not only with chemically reactive gases such as hydrogen or oxygen, but also with unreactive nitrogen. That such a compound forms at low pressure, exhibits metallic properties, and stable to both high-pressure and high-temperature conditions will no doubt stimulate further research in the reactivity of xenon, an element which now appears to be substantially less inert than previously thought.

Methods

We have studied the formation conditions and stability of xenon and nitrogen compounds up to pressures of 180 GPa in a diamond anvil cell (DAC). In total 12 DAC loadings were performed. 200 μm culet flat diamonds were used for experiments under 50 GPa, while 60 μm and 150 μm culets were used for higher pressure experiments. In all experiments rhenium foil was used as the gasket material.

The loading of the Xe-N_2 consisted of two stages. Solid Xe (99.9% purity) was initially cryogenically loaded into a DAC under a N_2 atmosphere. Loading was confirmed initially through comparisons of white light transmission spectra due to the change in refractive index between the empty sample chamber and loaded sample. Thorough mapping of the sample with Raman spectroscopy was carried out to ensure no impurities were present in the sample and further confirmation was obtained through x-ray diffraction analysis.

N_2 gas (99.9% purity) was then loaded into the cell at a pressure of 20 MPa using a high-pressure gas loading system, displacing some of the pre-existing Xe gas. The volume ratio was estimated by the phase separation of Xe and N_2 in the fluid state. Using a combination of varying pressure and temperature, single crystals of the Xe rich mixture were grown.

We have used 514 and 647 nm as excitation wavelengths in the Raman spectroscopy measurements using a custom-built micro-focussed Raman system. Pressure was determined through both ruby fluorescence ($P < 100$ GPa) and the Raman edge of the stressed diamond[33].

Powder x-ray diffraction data were collected at several beamlines: BL10XU at SPring-8 (Japan), IDB PETRA-III (Germany), ID09 at the European Synchrotron Radiation Facility (France), and ID-BMD of HPCAT at APS (USA). Incident beam energies in the range 25–30 keV were used. Intensity *vs.* 2θ plots were obtained by integrating image plate data in various formats using DIOPTAS[34]. Indexing was carried out in GSAS-II[35], Le Bail and Rietveld refinements were carried out in Jana2006[36]. Equation of state data were determined using EosFIT 7[37]. Fitted equation of state parameters for $Xe(N_2)_2$-I: $V_0 = 873(90)$ Å^3, $K_0 = 47(56)$ GPa, $K' = 1(5)$. Equation-of-state parameters for $Xe(N_2)_2$-II: $V_0 = 526(158)$ Å^3, $K_0 = 9(14)$ GPa, $K' = 4.5(11)$, $K'' = -0.51131$ GPa^{-1}.

References

1. Goncharov, A., Gregoryanz, E., Mao, H., Liu, Z. & Hemley, R. Optical evidence for a non-molecular phase of nitrogen above 150 gpa. *Phys. Rev. Lett.* **85,** 1262–1265 (2000).
2. Eremets, M. I., Hemley, R. J., Mao, H.-k. & Gregoryanz, E. Semiconducting non-molecular nitrogen up to 240 gpa and its low-pressure stability. *Nature* **411,** 170–174 (2001).
3. Gregoryanz, E., Goncharov, A. F., Hemley, R. J. & Mao, H.-k. High-pressure amorphous nitrogen. *Phys. Rev. B* **64,** 052103 (2001).
4. Gregoryanz, E. *et al.* Raman, infrared, and x-ray evidence for new phases of nitrogen at high pressures and temperatures. *Phys. Rev. B* **66,** 224108 (2002).
5. Eremets, M. I., Gavriliuk, A. G., Trojan, I. A., Dzivenko, D. A. & Boehler, R. Single-bonded cubic form of nitrogen. *Nat. Mater.* **3,** 558–563 (2004).
6. Gregoryanz, E. *et al.* High p-t transformations of nitrogen to170 gpa. *J. Chem. Phys.* **126,** 184505 (2007).
7. Tomasino, D., Kim, M., Smith, J. & Yoo, C.-S. Pressure-induced symmetry-lowering transition in dense nitrogen to layered polymeric nitrogen (lp-n) with colossal raman intensity. *Phys. Rev. Lett.* **113,** 205502 (2014).
8. Frost, M., Howie, R. T., Dalladay-Simpson, P., Goncharov, A. F. & Gregoryanz, E. Novel high-pressure nitrogen phase formed by compression at low temperature. *Phys. Rev. B* **93,** 024113 (2016).
9. Gregoryanz, E. *et al.* Synthesis and characterization of a binary noble metal nitride. *Nat. Mater.* **3,** 294–297 (2004).
10. Young, A. *et al.* Synthesis of novel transition metal nitrides IrN_2 and OsN_2. *Phys. Rev. Lett.* **96,** 155501 (2006).
11. Bartlett, N. Xenon hexafluoroplatinate(v) xe + [ptf6]. *Proc. Chem. Soc.* **218** (1962).
12. Classen, H. H., Selig, H. & Malm, J. G. Xenon tetrafluoride. *J. Am. Phys. Soc.* **84,** 3593–3593 (1962).
13. Somayazulu, M. *et al.* Pressure-induced bonding and compound formation in xenon-hydrogen solids. *Nat. Chem.* **2,** 50–53 (2009).
14. Weck, G., Dewaele, A. & Loubeyre, P. Oxygen/noble gas binary phase diagrams at 296 K and high pressures. *Phys. Rev. B* **82,** 014112 (2010).
15. Sanloup, C., Mao, H.-k. & Hemley, R. J. High-pressure transformations in xenon hydrates. *P. Natl. Acad. Sci.* **99,** 25–28 (2001).
16. Sanloup, C., Bonev, S. A., Hochlaf, M. & Maynard-Casely, H. E. Reactivity of xenon with ice at planetary conditions. *Phys. Rev. Lett.* **110,** 1–5 (2013).
17. Dewaele, A. *et al.* Synthesis and stability of xenon oxides Xe_2O_5 and Xe_3O_2 under pressure. *Nat. Chem.* advance online publication (2016).
18. Sanloup, C. *et al.* Retention of xenon in quartz and earth's missing xenon. *Science* **310,** 1174–1177 (2005).
19. Seoung, S. *et al.* Irreversible xenon insertion into a small-pore zeolite at moderate pressures and temperatures. *Nat. Chem.* **6,** 835 (2014).
20. Brock, D. S. & Schrobilgen, G. J. Synthesis of the missing oxide of xenon, XeO_2, and its implications for earth's missing xenon. *J. Am. Chem. Soc.* **133,** 6265–6269 (2011).
21. Zhu, Q. *et al.* Stability of xenon oxides at high pressures. *Nat. Chem.* **5,** 61–65 (2012).
22. Zhu, L., Liu, H., Pickard, C. J., Zou, G. & Ma, Y. Reactions of xenon with iron and nickel are predicted in the earth's inner core. *Nat. Chem.* **6,** 644–648 (2014).
23. Miao, M.-s. *et al.* Anionic chemistry of noble gases: Formation of mg-ng (ng = xe, kr, ar) compounds under pressure. *J. Am. Chem. Soc.* **137,** 14122–14128 (2015).
24. Peng, F., Wang, Y., Wang, H., Zhang, Y. & Ma, Y. Stable xenon nitride at high pressures. *Phys. Rev. B* **92,** 094104 (2015).
25. Kooi, M. E. & Schouten, J. A. High-pressure raman investigation of mutual solubility and compound formation in Xe N_2 and Ne N_2. *Phys. Rev. B* **60,** 12635–12643 (1999).
26. Kooi, M. E., Michels, J. P. J. & Schouten, J. A. Negative vibrational shift of nitrogen diluted in xenon at the fluidsolid transition. *J. Chem. Phys.* **110,** 3023–3025 (1999).
27. Reichlin, R. *et al.* Evidence for the insulator-metal transition in xenon from optical, x-ray, and band-structure studies to 170 gpa. *Phys. Rev. Lett.* **62,** 669–672 (1989).
28. Goettel, K. A., Eggert, J. H., Silvera, I. F. & Moss, W. C. Optical evidence for the metallization of xenon at 132(5) gpa. *Phys. Rev. Lett.* **62,** 665–668 (1989).
29. Eremets, M. *et al.* Electrical conductivity of xenon at megabar pressures. *Phys. Rev. Lett.* **85,** 2797–2800 (2000).
30. Dewaele, A., Loubeyre, P., Dumas, P. & Mezouar, M. Oxygen impurities reduce the metallization pressure of xenon. *Phys. Rev. B* **86,** 014103 (2012).
31. Hanfland, M. *et al.* Structures of molecular nitrogen at high pressures. *The Review of High Pressure Science and Technology* **7,** 787–789 (1998).

32. Cynn, H. *et al.* Martensitic fcc-to-hcp transformation observed in xenon at high pressure. *Phys. Rev. Lett.* **86,** 4552–4555 (2001).
33. Akahama, Y. & Kawamura, H. Pressure calibration of diamond anvil raman gauge to 410 gpa. *J. Phys.: Conf. Ser.* **215,** 012195 (2010).
34. Prescher, C. & Prakapenka, V. B. Dioptas: a program for reduction of two-dimensional x-ray diffraction data and data exploration. *High Pressure Res*. **35,** 223–230 (2015).
35. Toby, B. H. & Von Dreele, R. B. GSAS-II: the genesis of a modern open-source all purpose crystallography software package. *J. Appl. Crystallogr*. **46,** 544–549 (2013).
36. Petříček, V., Dušek, M. & Palatinus, L. Crystallographic computing system jana2006: general features. *Z. Kristallogr.* **229,** 345–352 (2014).
37. Gonzalez-Platas, J., Alvaro, M., Nestola, F. & Angel, R. EosFit7-GUI: a new graphical user interface for equation of state calculations, analyses and teaching. *J. Appl. Crystallogr*. **49**, 1377–1382 (2016).

Acknowledgements

Synchrotron radiation experiments were performed at the BL10XU of SPring-8 with the approval of the Japan Synchrotron Radiation Research Institute (JASRI) (Proposal No. 2016A1041), the authors would like to acknowledge Saori Imada and Naohisa Hirao for assistance with experiments. We acknowledge the European Synchrotron Radiation Facility for provision of synchrotron radiation facilities and we would like to thank Micheal Hanfland for assistance in using beamline ID09. Parts of this research were carried out at the light source PETRA III at DESY, a member of the Helmholtz Association (HGF). We would like to thank Konstantin Glazyrin for assistance in using beamline IDB. This research used resources of the Advanced Photon Source, a U.S. Department of Energy (DOE) Office of Science User Facility operated for the DOE Office of Science by Argonne National Laboratory under Contract No. DE-AC02-06CH11357. Part of this work were performed at HPCAT (Sector 16), Advanced Photon Source (APS), Argonne National Laboratory (ANL), we would like to thank Changyong Park for assistance with experiments. This work was supported by a research grant from the U.K. EPSRC Leadership Fellowship grant EP/J003999/1.

Author Contributions

R.T.H. conceived and designed the project, carried out the experiments, analysed the data and wrote the paper. R.T. and J.B. carried out the experiments, analysed the data and wrote the paper. M.F. and P.D.-S. carried out the experiments. E.G. analysed the data and wrote the paper.

Additional Information

Supplementary information accompanies this paper at http://www.nature.com/srep

Competing financial interests: The authors declare no competing financial interests.

How to cite this article: Howie, R. T. *et al.* Formation of xenon-nitrogen compounds at high pressure. *Sci. Rep.* **6**, 34896; doi: 10.1038/srep34896 (2016).

Supplementary Information

Formation of xenon-nitrogen compounds at high pressure

Ross T. Howie[1*], Robin Turnbull[2], Jack Binns[1], Mungo Frost[2], Philip Dalladay-Simpson [1], Eugene Gregoryanz[2]

[1] Center for High Pressure Science & Technology Advanced Research, Pudong, Shanghai, P.R. China.
[2] Centre for Science at Extreme Conditions and School of Physics and Astronomy, University of Edinburgh, Edinburgh EH9 3JZ, UK.

*e-mail: ross.howie@hpstar.ac.cn

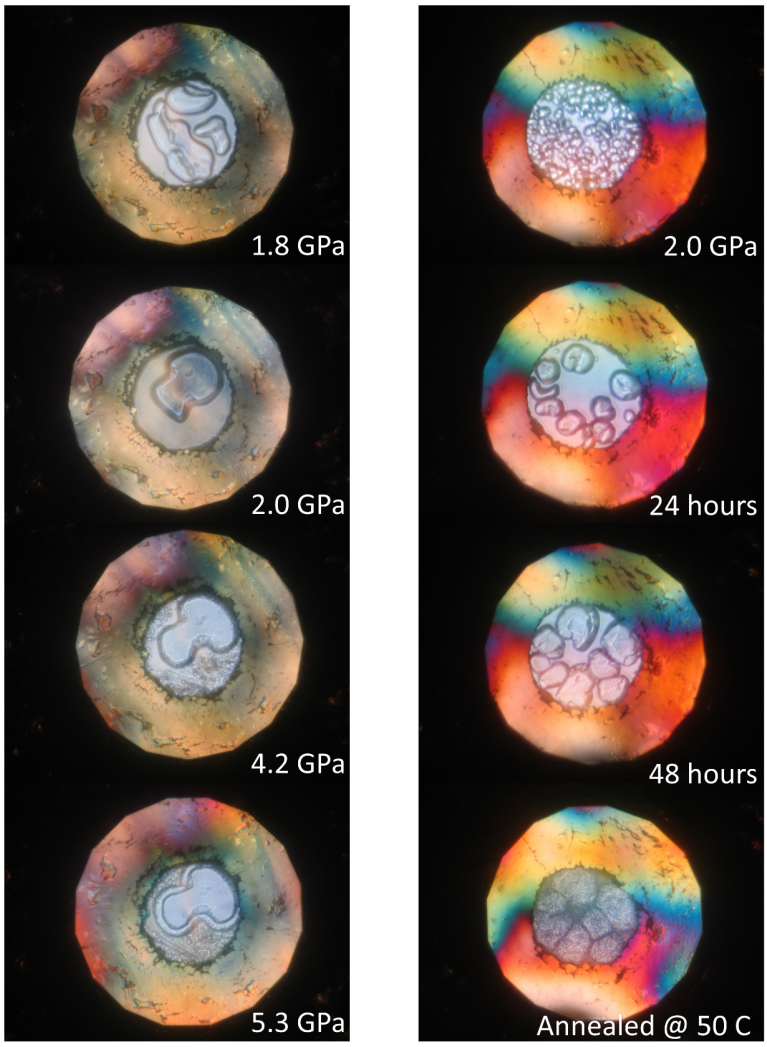

Figure S1. Micrographs of Xe-N_2 samples at low pressures. The left column shows the behaviour of a Xe-N_2 mixture of roughtly 50/50 on compression to 5.3 GPa. The "8" shape figure is Xe single crystal embedded in a $Xe(N_2)_2$. The right column shows the evolution of a Xe-rich N_2/Xe mixture over a 48 hour period after sample loading at constant pressure.

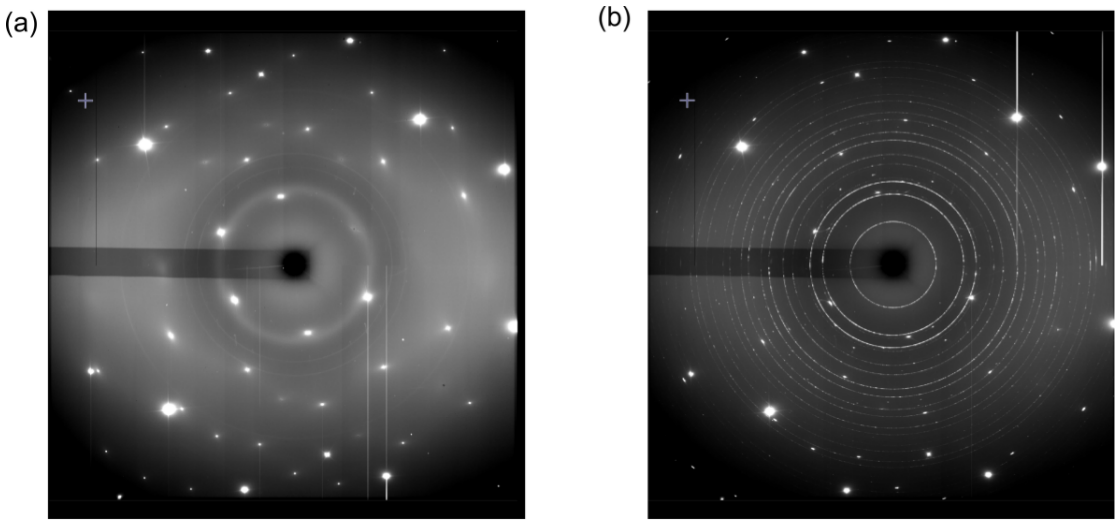

Figure S2. X-ray diffraction image plates (a) Data collected at 3 GPa shows the presence of the Xe fcc phase and the first diffraction peak from liquid nitrogen; (b) At 5.6 GPa the diffraction pattern of polycrystalline $Xe(N_2)_2$ phase dominates the image plate. Additional peaks are due to excess Xe and scattering from the diamond anvils.

	Phase I	Phase II
Crystal data		
Chemical formula	$Xe(N_2)_2$	$Xe(N_2)_2$
M_r	243.3	243.3
Crystal system, space group	Cubic, $Fd\bar{3}m$	Tetragonal, $I4_1/amd$
Pressure (GPa)	5.6	18.7
a (Å)	9.2361 (3)	5.7228 (3)
c (Å)	9.2361 (3)	9.2134 (10)
V (Å^3)	787.88 (5)	301.74 (4)
Z	8	4
Radiation type	Synchrotron ($\lambda = 0.4872$ Å)	Synchrotron ($\lambda = 0.4872$ Å)
Data collection		
2θ values (°)	$2\theta_{min} = 3.416$, $2\theta_{max} = 33.451$, $2\theta_{step} = 0.011$	$2\theta_{min} = 3.724$, $2\theta_{max} = 24.979$, $2\theta_{step} = 0.011$
Refinement		
R factors and goodness of fit	$R_p = 0.009$, $R_{wp} = 0.019$, $R_{exp} = 0.018$, $R(F) = 0.082$, $\chi^2 = 1.103$	$R_p = 0.015$, $R_{wp} = 0.021$, $R_{exp} = 0.018$, $R(F) = 0.094$, $\chi^2 = 1.369$
No. of parameters	8	17

TABLE I. Crystal structure data, experiment and refinement details for $Xe(N_2)_2$ phases I and II.

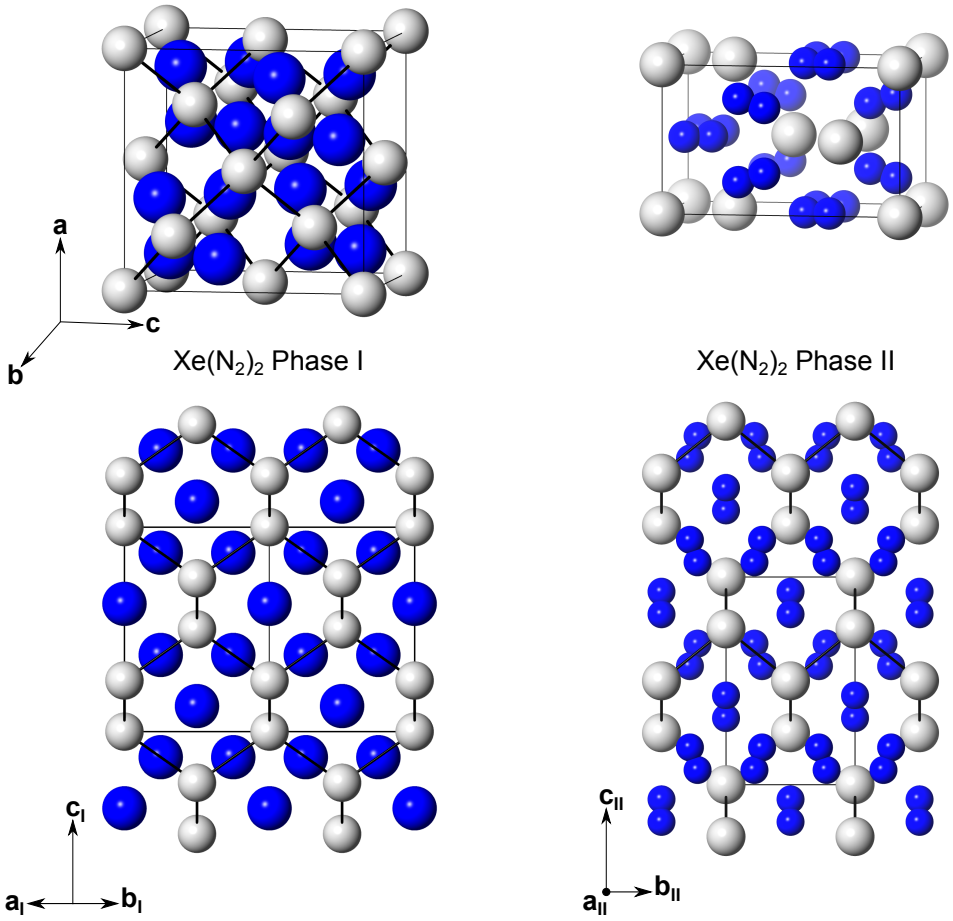

Figure S3. Crystal structures of $Xe(N_2)_2$ phases I and II. Ordering and alignment of N_2 molecules occurs over the transition leading to a tetragonal distortion along $\mathbf{c}_{II}$. Freely rotating N_2 molecules in phase I are represented by blue balls, whilst in phase II blue balls represent atoms in aligned molecules.

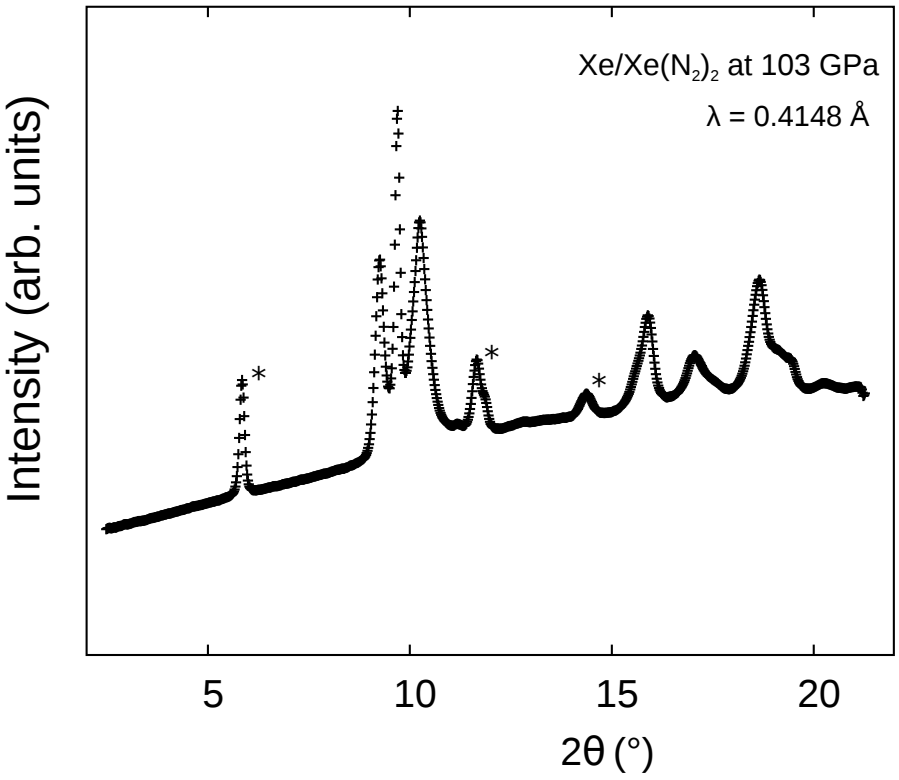

Figure S4. X-ray diffraction pattern of $Xe/Xe(N_2)_2$ at 103 GPa. Low-angle peak marked by * corresponds to the (101) peak of $Xe(N_2)_2$, additional diffracted intensity marked by * are also due to $Xe(N_2)_2$, although an unambiguous indexing is not possible due.

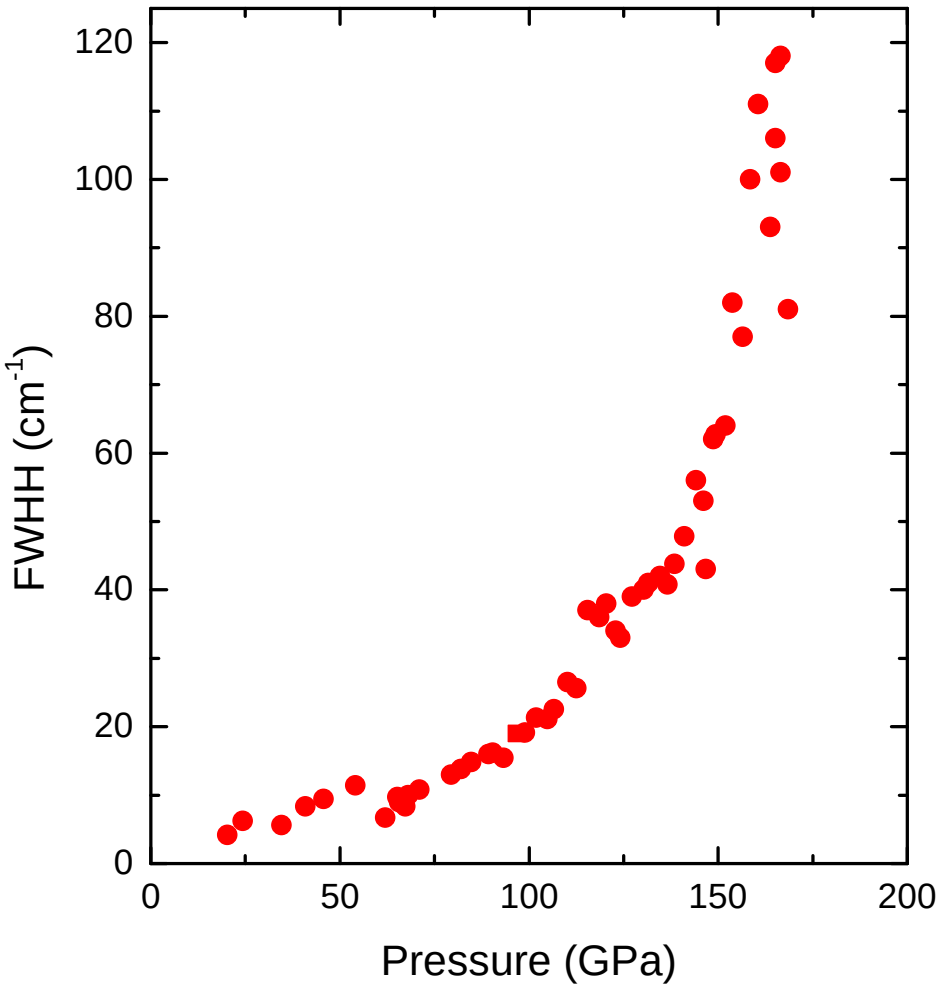

Figure S5. Full width at half height as a function of pressure for the Xe-rich sample.

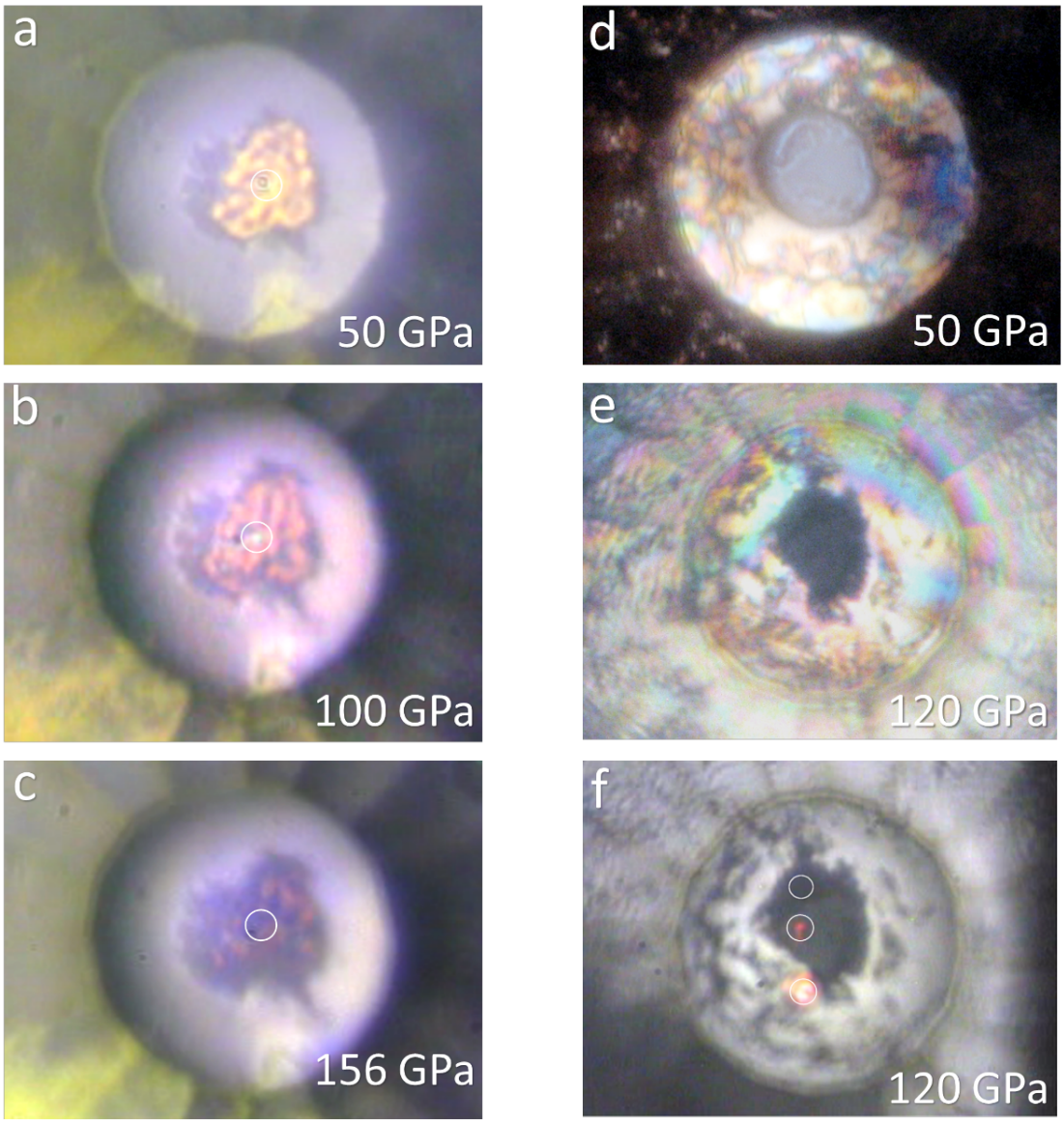

Figure S6. (a-c): The nitrogen-rich sample becomes less transparent to visible light on compression to 156 GPa. 514 nm laser light is incident in the centre of each sample indicated by white circles; (d-e); The Xe-rich sample was transparent at 50 GPa becoming opaque by 120 GPa; (e) Xe-rich sample at 120 GPa. 647 nm laser light of the same intensity is incident on the gasket and the sample as indicated by the white circles.

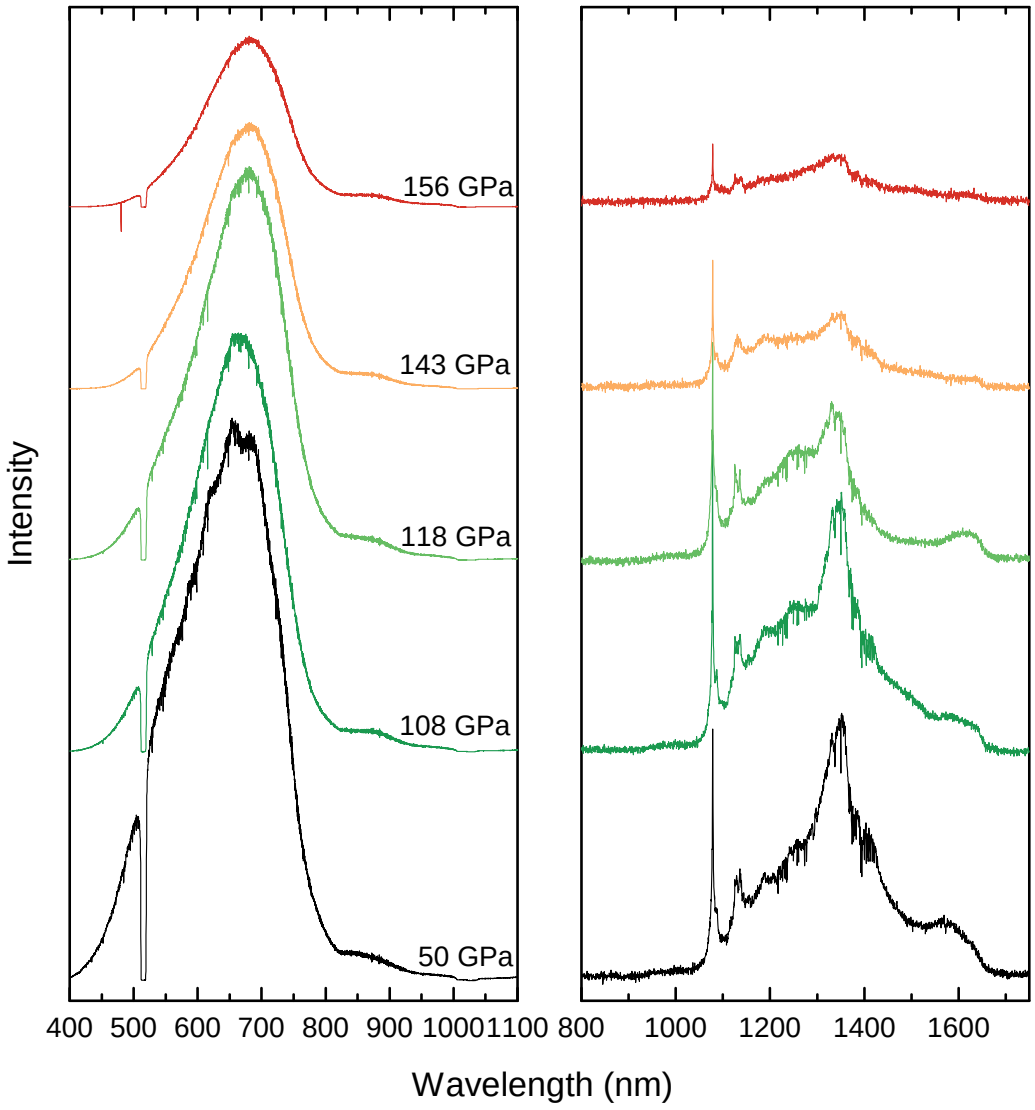

Figure S7. Raw transmission spectra for the N_2-rich sample in the visible (left) and mid infra-red regions (right) up to 156 GPa. The dip in intensity at 514 nm is due to the notch filters.